NUMERICAL SIMULATION OF PULSATILE FLOW IN A CONSTRICTED CHANNEL

Dissertation Report

SUBMITTED IN PARTIAL FULFILLMENT OF THE REQUIREMENTS FOR THE AWARD OF THE DEGREE OF

Master of Technology
in
Mechanical Engineering
(Thermal Sciences)

Submitted by
SUFIA KHATOON
14 METM 015

Under the Supervision of
Dr. Syed Fahad Anwer

DEPARTMENT OF MECHANICAL ENGINEERING
ZAKIR HUSAIN COLLEGE OF ENGINEERING & TECHNOLOGY
ALIGARH MUSLIM UNIVERSITY
ALIGARH (INDIA)
2015-2016

CERTIFICATE
CANDIDATE'S DECLARATION

I hereby declare that this dissertation, titled **"NUMERICAL SIMULATION OF PULSATILE FLOW IN A CONSTRICTED CHANNEL"** is being submitted in partial fulfilment of the requirement for the award of the degree of **Master of Technology** in **Mechanical Engineering** with specialization in **Thermal Sciences** in the **Department of Mechanical Engineering, Z.H.C.E.T, Aligarh Muslim University, Aligarh** is an authentic record of my work under the supervision of **Dr. Syed Fahad Anwer**.

This thesis, and the material in it, is my own work. It has not been submitted in any previous application for any degree**.**

Dated:

<div align="right">

SUFIA KHATOON

14-METM-015

GC1527

</div>

SUPERVISOR'S DECLARATION

This is to certify that the above statement made by the candidate is correct to the best of my knowledge.

Dated:

<div align="right">

Dr. Syed Fahad Anwer

Department of Mechanical Engineering

Z.H. College of Engineering & Technology

Aligarh Muslim University, Aligarh

</div>

ACKNOWLEDGEMENT

Table of Contents

List of Figures

List of Tables

Nomenclature

dt	$\equiv$	non dimensional time step
i,j	$\equiv$	local grid indices
x,y	$\equiv$	coordinates in physical plane
ξ, η	$\equiv$	coordinates in computational plane
p'	$\equiv$	pressure correction term
p^n	$\equiv$	current pressure
p^{n+1}	$\equiv$	corrected pressure
τ	$\equiv$	non-dimensional time
$\overline{U}$	$\equiv$	guessed velocity
U^n	$\equiv$	velocity at current time level
U'	$\equiv$	velocity correction term
U^{n+1}	$\equiv$	corrected velocity
Re	$\equiv$	Reynolds number
St	$\equiv$	Strouhal number
Pe	$\equiv$	Peclet number
Wo	$\equiv$	Womersley number
ω	$\equiv$	angular frequency
ν	$\equiv$	kinematic viscosity
μ	$\equiv$	dynamic viscosity
T	$\equiv$	stress tensor
μ_o, μ_∞	$\equiv$	asymptotic apparent viscosity
Λ	$\equiv$	material constant

Abstract

Numerical simulations are performed for pulsatile flow of blood through a constricted channel with single stenosis in two-dimensions. The stenosis is modelled using a semi-circular constriction on the upper wall of the channel. This configuration is assumed as a simple model for studying blood flow in a constricted artery. The governing flow equations are solved using a finite difference scheme in a body fitted coordinate system. Three different inflow velocity profiles (uniform, sinusoidal and non-sinusoidal) are taken to study the flow. The observations have revealed that the presence of stenosis leads to a recirculation zone downstream of the stenosis. Simulations are done on Reynolds number of 750 and 500 and Strouhal number of 0.024 and 0.048 to study the pulsatile flows. These range of values are taken as they fall in the physiological range of blood flow. The effects of varying the Reynolds number (Re) and Strouhal number (St) on the flow of blood through a two-dimensional channel with stenosis are investigated and the results are compared.

First, all the flows are studied assuming blood to be a Newtonian fluid and then blood is modelled as a non-Newtonian fluid using the shear-thinning relation proposed by Yeleswarapu[13]. The observations show that strong vortex waves are generated for pulsatile flows in comparison to uniform flows with complex wall shear rate and pressure distribution. Also on increasing the Reynolds number, the strength of vortex waves increases. A significant difference in different fluid dynamic properties is observed based on the inflow velocity pattern. The simulations show that the shear-thinning fluid predicts higher peak wall shear rate than the Newtonian fluid for uniform inflow velocity. However the non-Newtonian model shows less complexities in the fluid dynamics as compared to Newtonian model. Lesser vortex waves are formed in the non-Newtonian model which decay faster in a cycle.

A POD analysis of the computational data is also done to analyse the statistical patterns in the ensemble of spatially distributed data and find out the most dominant structures in the flow fields. The number of POD modes which are required to reconstruct the flow fields are calculated and the structures are compared with the DNS snaps. These results are of importance when developing a model for plaque growth based on mechanical factors. They also help in studying spatially developing and time periodic flows.

Chapter 1 Introduction

In this chapter a brief introduction to the research work is given. § 1.1 covers the aspects of importance of research work in this field and why further extensive research is needed in current area. In § 1.2, literature survey is done over the work done so far in this field and then how we have taken the approach towards this problem is covered in § 1.3. The various goals which we have set forth in this work are discussed in § 1.4.

1.1 Motivation

According to a recent survey of World Health Organization held in January 2015, cardiovascular diseases (CVDs) are the leading cause of death globally [1]. It is said that more people die annually due to CVDs than due to any other cause. Therefore blood flow under diseased condition is an important field of study. The desire to understand the flow of blood through the cardiovascular system and prosthetic devices has led to a lot of research activity in the field of hemodynamics. Such studies hold importance because there is indirect evidence that the developments and cause of many cardiovascular diseases are, to a great extent, related to the characteristics of blood flow, such as due to the high values of the shear stress at the wall or its variation. Hence it is important to understand the connection between blood flow characteristics and development of cardiovascular diseases. Although the exact mechanisms responsible for the initiation of this phenomena are not yet clearly known, it has been established that once a mild stenosis is developed, the resulting flow disorder further enhances the development of the disease and arterial deformity, and change the regional blood rheology [2, 5].

Atherosclerosis is a chronic disease which leads to excessive deposition of lipids (cholesterol) in the artery wall. In some cases, they form a solid structure (plaque) and become calcified immediately beneath the wall surface. Figure 1.1 shows a normal artery and an artery with plaque deposition. This plaque projects into the artery lumen (inside space of the tubular structure) and significantly alters the blood flow in the artery. The rheological properties of blood hold importance in the development of plaque in the circulatory system. The occluded section consisting of the plaque which projects into the artery lumen is called a stenoses. Plaque is made up of fat, cholesterol, calcium, and other substances which are found in blood. Over time, the plaque hardens and narrows the arteries. This limits the flow of oxygen-rich blood to

the organs and other body parts. Localized atherosclerotic constrictions in arteries, known as arterial stenoses, are found predominantly in the internal carotid artery which supplies blood to the brain, the coronary artery which supplies blood to the cardiac muscles, and the femoral artery which supplies blood to the lower limbs. Blockage of more than about 70% (by area) of the artery is considered clinically significant since it presents significant health risks for the patient [15]. If a blood-clot becomes lodged in the stenosis, complete closure of the artery can occur and this can lead to a stroke or a heart attack. Moreover, even moderate and severe stenoses can have long-term health consequences. The presence of a constriction results in head losses which can reduce the blood supply to the artery and as a result increase the work load on the heart. The fluctuations in the blood flow downstream of the stenosis can damage and weaken the internal wall (intima) of the artery. It is accepted that both the wall pressure and shear stress play a role in this [3]. Atherosclerosis can lead to serious problems, including heart attack, stroke, or even death. It can affect any artery in the body, including arteries in the heart, brain, arms, legs, pelvis, and kidneys. As a result, different diseases may develop based on which arteries are affected.
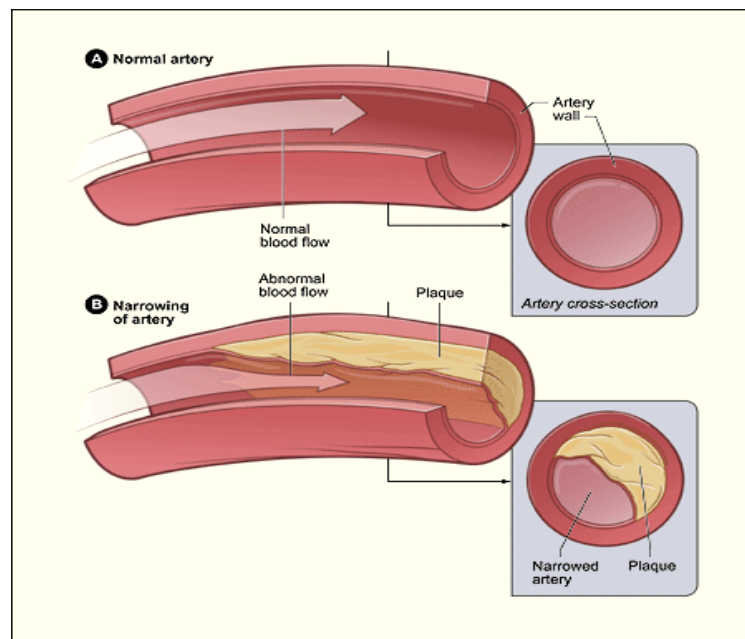
Figure 1.1 (A) shows normal artery with normal blood flow. The inset image shows a cross-section of a normal artery. Figure (B) shows an artery with plaque buildup. The inset image shows a cross-section of an artery with plaque buildup.[1]

Fluid dynamics of flow downstream of the stenosis also plays a key role in the diagnosis of arterial disease. In this work an attempt has been made to study the effects of pulsatility and non-Newtonian nature of blood on physiologically important flow quantities such as velocity, pressure and wall shear rate for blood flow in an artery. The effects of pulsatility, Reynolds number and Strouhal number of the fluid on velocity profiles, pressure, wall shear rate and vorticity are analyzed.

1.2 Literature review

Understanding the phenomena of stenotic flow has proceeded from quite a good number of theoretical, computational and experimental efforts. Assuming blood flow to be steady flow, flow through an axisymmetric stenosis has been investigated extensively by Smith [3] using an analytical approach concluding that the flow patterns strongly depend on the geometry of the stenosis and the upstream Reynolds number. However, blood flow is unsteady. The cyclic nature of the heart pump creates pulsatile conditions in all arteries. The heart ejects and fills with blood in alternating cycles called systole and diastole. Blood is pumped out of the heart during systole while the heart rests during diastole, and no blood is ejected. Pressure and flow have characteristic pulsatile shapes that vary in different parts of the arterial system. Therefore considering the fact that blood flow is pulsatile in nature and this nature of the blood flow through arteries cannot be neglected many theoretical analysis and experimental measurements on the flow through stenosis have been performed. Womersley [4] considered the flow of blood through a straight pipe driven by an oscillatory pressure gradient. A dimensional analysis of the unsteady Navier-Stokes equations leads to a non-dimensional number commonly referred to as the Womersley parameter (Wo):

$$Wo = R\sqrt{\frac{\omega}{\nu}}$$

where R is the tube radius, ω is the angular frequency, and ν is the kinematic viscosity of blood. In this study it was observed that the degree of departure from the normal parabolic form increases with Wo, i.e. with the Womersley frequency parameter. The Womersley parameter (Wo) can be interpreted as the ratio of the unsteady forces to the viscous forces. When the Womersley parameter is low, viscous forces dominate and velocity profiles are parabolic in shape. For Womersley parameters above 10, the unsteady inertial forces dominate, and the flow is essentially one of piston-like motion with a flat velocity profile.

Liepsch [5] did experiments on hemodynamic effects in elastic silicon rubber models of the cardiovascular system with flow wire, stents, or patches for vessel surgery. He concluded that once a mild stenosis is developed, resulting flow disorder further influences the development of disease. Tutty [16] has performed numerical simulation in a constricted channel for pulsatile flows and studied the various flow patterns for a range of Reynolds number and Strouhal number. He has concluded from his study that there is much difference in the flow patterns obtained from a physiological pulse and sinusoidal pulse. Mittal et al [4] used Direct Numerical Simulation (DNS) and Large-Eddy Simulation (LES) to study pulsatile flow in a channel with a one-sided semicircular constriction over a range of Reynolds numbers from 750 to 2000. They showed that flow downstream of the constriction in the current simulations, exhibits a number of features observed before in experiments carried out in more realistic configurations. But they have modelled blood as a Newtonian fluid which is only valid for larger arteries.

In most of the studies discussed so far, blood is assumed to be a Newtonian fluid. The composition of blood is a complex mixture of cells, proteins, lipoproteins, and ions by which nutrients and wastes are transported. At a macroscopic level, blood appears to be a liquid material, but at a microscopic level blood appears to be a material with microscopic solid particles of varying size which are the various blood cells. Red blood cells comprise approximately 40% of blood by volume. Since red blood cells are small semisolid particles, they increase the viscosity of blood and affect the behavior of the fluid. Blood is approximately four times more viscous than water [23]. Moreover, blood does not exhibit a constant viscosity at all flow rates and is especially non-Newtonian in the microcirculatory system [23]. The non-Newtonian behavior is most evident at very low shear rates when the red blood cells clump together into larger particles. Blood also exhibits non-Newtonian behavior in small branches and capillaries, where the cells squeeze through and a cell-free skimming layer reduces the effective viscosity through the tube. The assumption of Newtonian behaviour of blood is acceptable for high shear rate flow, i.e. the case of flow through larger arteries [8]. However, it is not valid when the shear rate is low as is the flow in smaller arteries and in post-stenotic region. It has been pointed out that in some diseased conditions, blood exhibits remarkable non-Newtonian properties. Hemorheological studies have documented three types of non-Newtonian blood properties: Thixotropy, Viscoelasticity and Shear thinning [17]. Thurston [15, 16] has shown conclusively that blood, being a suspension of enumerable number of cells, possesses significant viscoelastic properties in the frequency range of physiological importance. Studies pertaining to the viscoelasticity of blood are of great interest because of

three main reasons. To medical scientists, an accurate knowledge of the mechanical properties of whole blood and the erythrocytes can suggest a new diagnostic tool. For specialists in fluid mechanics, detailed information of the complex rheological behaviour of the system is of utmost importance in any attempt towards establishing the equations that govern the flow of blood in various parts of the circulatory system in different states. To rheologists, blood (whose biochemical and cellular compositions are well-known in other respects) is an excellent model for correlating its rheological behaviour with the underlying molecular or cellular structures. However, the viscoelasticity of blood diminishes very rapidly as shear rate rises and at physiological hematocrit values ($\sim$ 45%) [17]. This suggests that viscoelasticity has a secondary impact on normal pulsatile blood flow at physiological hematocrit values. The shear thinning properties of blood, however, are not transient and are exhibited in normal blood at all shear rates upto about $100 \ s^{-1}$. The purely viscous shear thinning nature of blood is, therefore, the dominant non-Newtonian effect. The flow of non-Newtonian fluid models through stenosed pipes have been widely studied using various models such as Casson, Herschel–Bulkley, Power-law, Oldroyd-B, and various generalized Oldroyd-B models [11, 12, 17, 18]. Many of these models are known to predict blood flow behavior better than the Newtonian model. Prakash [9] used Power-law model and blood vessel was heated externally. They showed that increase in radiation parameter leads to an increase in axial velocity and shear stress . Yeleswarapu [13] performed the evaluation of continuum models for characterizing the constitutive behaviour of blood. He introduced a shear rate-dependent viscosity term in the classical Oldroyd-B model for a viscoelastic fluid, and used it to model blood. Nandakumar et. al. [7] simulated blood flow in a 2D stenosed channel using the model proposed by Yeleswarapu. They concluded the key differences between the shear-thinning model and the Newtonian model in both uniform and pulsatile flows. However, they considered Reynolds number for larger aorta and percentage stenosis only up to 25%. They showed that there is little difference in aorta size blood vessel and the difference increase with increase in percentage stenosis. This is expected, as for large size vessels blood can be considered Newtonian.

Based on the various studies done so far our goal is to study in general terms the behavior of the flow in constricted channel with particular emphasis on features of physiological interest such as the pressure and shear rate distribution on the channel walls. We will first consider the Newtonian behavior of blood and then study the generalized Newtonian model with Re in the regime of human arteries. As a simple model a channel with a symmetric constriction has been

used. The various physiological properties will be studied for uniform and pulsatile flow in this channel. Also the effects of changing the Reynolds number and the Strouhal number are studied.

1.3 Problem Formulation

This work focusses on developing a computational methodology which studies blood flow through a blood vessel segment having a stenosis in its lumen which is modelled as a semi-circular constriction as shown in Figure 1.2. The shape of the stenosis is taken to be a semicircle with radius equal to half the width of the channel. In the computational domain a finite difference type of discretisation has been used. Three different velocity profiles have been separately taken at the inlet. The unsteady equations, transformed in the computational domain, are marched forward in time by using a semi-explicit pressure correction scheme. The validity and performance of the entire procedure is demonstrated through some flow problems involving flows in channels.

The numerical procedure developed is then applied to a constricted channel to model blood flow in an artery. The various fluid dynamic properties are studied in the channel and their variation with Re and St is observed.
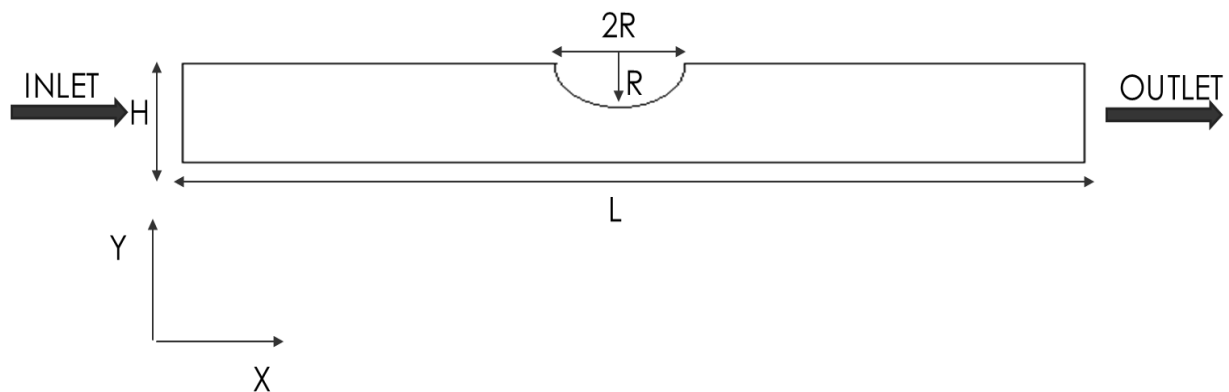
Figure 1.2 Schematic diagram of the stenosed channel

1.4 Objective of the present study

The objective of the present study is to develop a Computational Fluid Dynamics (CFD) model which is efficient and accurate in predicting fluid dynamics generated in constricted channels. Explicitly, the objectives are:

- To develop a CFD code for simulating blood flow in channels.
- To study uniform flow of blood under the influence of a constant velocity at inlet and recorded the variation of velocity profile and wall shear rate along the axial length with Reynolds(Re) and Strouhal(St) number .
- To consider the effect of pulsatile velocity profile (sinusoidal and non-sinusoidal) on the flow dynamics and record the variation of flow properties with time by varying the Re and St.
- To find the most dominant structure in the flow field by doing a POD analysis of our work.

Chapter 2 Mathematical model and Numerical Method

In this chapter the computational methodology used in the flow solver is discussed. The method has been applied to a structured body-fitted curvilinear non-orthogonal mesh flow solver employing a finite difference type of discretization. The unsteady equations transformed in the computational domain are marched forward in time by using a semi-explicit pressure correction scheme. This chapter is organized in seven sections. § 2.1 describes the governing equations for viscous incompressible flow and their transformation to non-orthogonal curvilinear coordinates. Non-Newtonian behavior of blood and the Generalized Newtonian model which is used in the current problem is discussed in § 2.2. The governing equations are transformed from physical plane to computational in § 2.3. A predictor corrector pressure correction scheme used to solve Navier Stokes equation is presented in § 2.4. The boundary and initial conditions are discussed in § 2.5. In § 2.6 validation of the methodology discussed above is done through flow in channels. The gird independence studies for this problem is given in § 2.7.

2.1 Governing Equations

The flow is governed by the continuity and momentum equations for an incompressible fluid as given below:

• Continuity equation

$$\nabla.\vec{U} = 0 \tag{2.1}$$

• Momentum equation

$$\rho\left(\frac{\partial\vec{U}}{\partial t} + \vec{U}\frac{\partial\vec{U}}{\partial x} + \vec{V}\frac{\partial\vec{U}}{\partial y}\right) = -\left(\frac{\partial\vec{P}}{\partial x}\right) + \mu\left(\frac{\partial^2\vec{U}}{\partial x^2} + \frac{\partial^2\vec{U}}{\partial y^2}\right) \tag{2.2}$$

2.1.1 Non-dimensional form of the governing equations

In order to convert the basic equations to non-dimensional form the length, velocity and time scales selected are as follows,

- Length scale = width of the channel 'D'
- Velocity scale = the centreline velocity at the inlet 'U'
- Time scale =D/U

The variables have been non-dimensionalized as follows:

U^{*}= u/U, V^{*}= v/U , τ = (t*U/D), $p = \frac{p}{\rho U^2}$ and $Re = \frac{\rho UD}{\mu}$,

The dimensionless form of continuity and momentum equations are obtained as,

$$\nabla \cdot \vec{U} = 0 \tag{2.3}$$

$$\frac{D^* U}{D\tau} = -\nabla^* p + \frac{1}{Re}(\nabla^* T) \tag{2.4}$$

where T is the stress tensor.

2.2 Generalized Newtonian model

Blood is a suspension of different cells in a liquid, the plasma, the red cells and platelets. It is generally assumed that the influence of red cells in blood rheology is predominant. Although plasma is constituted by 90% water, it is commonly accepted that blood is a non-Newtonian fluid because the elastic and deformable structure of red cells gives to it a shear dependent viscosity and a viscoelastic nature.

It is usually accepted that the Newtonian assumption for the constitutive nature of blood is adequate only for flow in larger vessels. However, at low shear rates ($<100 s^{-1}$) as well as in flows in smaller vessels, blood flow is not well described by the Navier-Stokes model [14]. The average shear rate at the wall of arteries is greater than this, and blood is assumed to be Newtonian in that region. Nevertheless, near the center of the vessel, or in separated regions of recirculating flow, the average value of shear rate will be small. Furthermore, in pulsatile flows, the wall shear stress vanishes twice per cycle, and there are instants where it is considerably small. In the last decades, many mathematical models have been studied to set a reliable constitutive equation for blood, in the attempt to model either the nonlinear dependence of the viscosity on the strain rate or the viscoelastic effects such as stress relaxation. Due to the variable behaviour and the complex chemical structure of this liquid, none of the constitutive equations studied so far seems to be completely satisfactory for all kinds of flow regimes.

A new model is being developed for blood [13], in which separate study has been done of the two components it has been built up, each of them being able to predict some particular properties. This is done in order to understand the role of the different concurrent forces on the flow.

In the Generalized Newtonian model blood is described using an incompressible shear-thinning model wherein the viscosity depends on the shear rate. The model is given by:

$$\bar{\bar{T}} = \mu(\boldsymbol{A_1})\boldsymbol{A_1}$$

Where $\bar{\bar{T}}$ is the stress tensor ,μ is the dynamic viscosity of blood and

$$A_1 = L + L^T$$
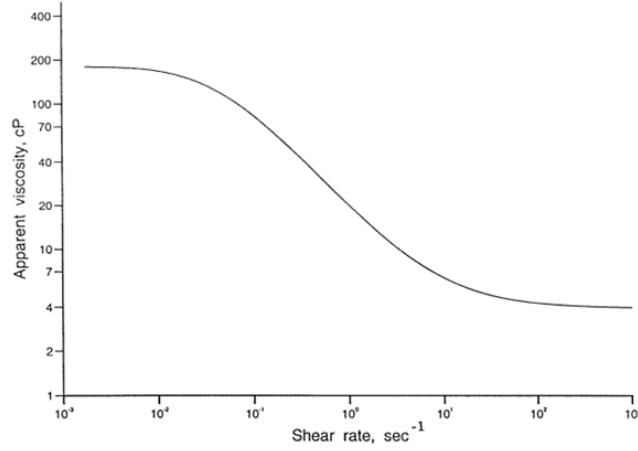
Figure 3. 1: Shear rate dependent viscosity function [8]

$$A_1 = \begin{bmatrix} 2\dfrac{\partial u}{\partial x} & \dfrac{\partial u}{\partial y} + \dfrac{\partial v}{\partial x} & \dfrac{\partial u}{\partial z} + \dfrac{\partial w}{\partial x} \\[2mm] \dfrac{\partial u}{\partial y} + \dfrac{\partial v}{\partial x} & 2\dfrac{\partial v}{\partial y} & \dfrac{\partial v}{\partial z} + \dfrac{\partial w}{\partial y} \\[2mm] \dfrac{\partial u}{\partial z} + \dfrac{\partial w}{\partial x} & \dfrac{\partial v}{\partial z} + \dfrac{\partial w}{\partial y} & 2\dfrac{\partial w}{\partial z} \end{bmatrix}$$

$$L = grad(v)$$

Where v is the velocity vector. Furthur the viscosity is a function of shear rate $(\dot{\gamma})$.

$$\mu(A_1) = \eta_\infty + \left(\eta_\circ - \eta_\infty\right)\left[\frac{1 + log(1 + \Lambda\dot{\gamma})}{1 + \Lambda\dot{\gamma}}\right] \tag{2.5}$$

The shear rate is given by

$$\dot{\gamma} = \left[\frac{1}{2}tr(A_1^2)\right]^{\frac{1}{2}}$$

$$\dot{\gamma} = \left[2\left(\frac{\partial^2 u}{\partial x^2} + \frac{\partial^2 v}{\partial y^2} + \frac{\partial^2 w}{\partial z^2}\right) + \left(\frac{\partial u}{\partial y} + \frac{\partial v}{\partial x}\right)^2 + \left(\frac{\partial u}{\partial z} + \frac{\partial w}{\partial x}\right)^2 + \left(\frac{\partial v}{\partial z} + \frac{\partial w}{\partial y}\right)^2\right]^{\frac{1}{2}}$$

Non-dimensionalizing equation (2.5) by dividing with η_∞ to obtain the non-dimensional form of the non-Newtonian model,

$$\mu^* = 1 + (\lambda - 1)\frac{[1 + ln(1 + \Lambda\dot{\gamma})]}{[1 + \Lambda\dot{\gamma}]} \tag{2.6}$$

Where

$$\lambda = \frac{\eta_o}{\eta_\infty}$$

Non dimensionalizing other variables as given below we get the non-dimensional form of momentum equation for the non-Newtonian model as shown in equation (2.7)

$U^* =$ u/U, $V^* =$ v /U , $\tau =$ (t*U/D), $p = \frac{p}{\rho U^2}$ and $Re = \frac{\rho UD}{\mu_\infty}$

$$\frac{D^*U}{D\tau} = -\nabla^* p + \mu^* \frac{1}{Re}(\nabla^* T) \tag{2.7}$$

η_o, η_∞ are the asymptotic apparent viscosity as $\dot{\gamma} \to 0$ and ∞ respectively, $\left(\eta_o > \eta_\infty\right)$, and $\Lambda \geq 0$, a material constant with the dimension of time representing the degree of shear-thinning. The complex nature of blood is approximated here with a three-parameter shear-thinning model, where the apparent viscosity is expressed as a decreasing function of the shear rate as shown in Figure 3.1. At low shear rates, the apparent viscosity increases considerably. The asymptotic values η_o and η_∞ are common in many other inelastic shear-thinning models and their values have been set up through experiments. These parameters have been fixed to some likelihood to the physiological measurements of blood flow and are as follows: $\Lambda=14.81s$ denotes the shear-thinning index, $\eta_o= 0.0736$ Pa s and $\eta_\infty= 0.005$ Pa s. For Newtonian fluids $\mu^*=1$ in equation (2.7).

2.3 Transformation of Governing Equations

Finite difference computations were hindered by the problem of fitting curved boundaries into computational grids. The use of interpolation between grid points for the application of boundary conditions on a curved boundary passing through a rectangular grid may lead to poor implementation of the boundary conditions. This is because finite difference equations depend on the continuity of derivatives and distribution of points. The problem can be overcome by the use of numerically generated body fitted coordinate system. This procedure allows the flow about arbitrary boundaries to be treated as computationally simple boundaries. All computations are done on rectangular mesh regardless of the shape or configurations of boundaries in the physical field. The technique of body fitted coordinate system is based on a process of algorithmic method of automatic numerical generation of general curvilinear coordinate system having a coordinate line coincident with each boundary of a general multiply connected region.

The curvilinear coordinates are generated as a solution of two elliptic partial differential equations (PDE). These elliptic PDEs are transformed to produce two elliptic PDEs for the

Cartesian coordinates as the function of curvilinear coordinates. Figure 2.1 shows a physical plane represented by Γ_1-Γ_4 mapped to computational plane represented by Γ^*_1-Γ^*_4. The grid system generated by this methodology is termed o-grids. As ξ and η are completely specified on the boundaries, the governing elliptic PDEs are,

$$\nabla^2 \xi = P(\xi, \eta) \tag{2.8a}$$

$$\nabla^2 \eta = Q(\xi, \eta) \tag{2.5b}$$

Where P and Q are control functions used to concentrate grid lines. The equation (2.8a) and (2.12) are then transformed into the computational plane. The resulting equations are given below:

$$\alpha \frac{\partial^2 x}{\partial \xi^2} - 2\beta \frac{\partial^2 x}{\partial \xi \partial \eta} + \gamma \frac{\partial^2 x}{\partial \eta^2} + J^2 (P \frac{\partial x}{\partial \xi} + Q \frac{\partial x}{\partial \eta}) = 0 \tag{2.9a}$$

$$\alpha \frac{\partial^2 y}{\partial \xi^2} - 2\beta \frac{\partial^2 y}{\partial \xi \partial \eta} + \gamma \frac{\partial^2 y}{\partial \eta^2} + J^2 (P \frac{\partial y}{\partial \xi} + Q \frac{\partial y}{\partial \eta}) = 0 \tag{2.6b}$$

Where

$$\alpha = ((x_\eta)^2 + (y_\eta)^2)/J^2$$

$$\gamma = ((x_\xi)^2 + (y_\xi)^2)/J^2$$

$$\beta = ((x_\eta x_\xi) + (y_\xi y_\eta))/J^2$$

$$J = (x_\xi y_\eta - x_\eta y_\xi)$$

The subscripts refer to partial derivatives with that variable.

The dimensional form of the governing equations (continuity and momentum) transformed in the body fitted coordinates are as follows:

Continuity:
$$(\xi_x \frac{\partial}{\partial \xi} + \eta_x \frac{\partial}{\partial \eta})U + (\xi_y \frac{\partial}{\partial \xi} + \eta_y \frac{\partial}{\partial \eta})V = 0 \tag{2.10}$$

x-Momentum:

22

$$\rho \left(\frac{\partial U}{\partial \tau} + U^{\xi} \frac{\partial U}{\partial \xi} + U^{\eta} \frac{\partial U}{\partial \eta} \right)$$

$$= -\left(\xi_x \frac{\partial p}{\partial \xi} + \eta_x \frac{\partial p}{\partial \eta} \right) + \mu (\alpha \frac{\partial^2 U}{\partial \xi^2} - 2\beta \frac{\partial^2 U}{\partial \xi \partial \eta} + \gamma \frac{\partial^2 U}{\partial \eta^2} \qquad (2.11)$$

$$+ \nabla^2 \xi \frac{\partial U}{\partial \xi} + \nabla^2 \eta \frac{\partial U}{\partial \eta})$$

y-Momentum:

$$\rho \left(\frac{\partial V}{\partial \tau} + U^{\xi} \frac{\partial V}{\partial \xi} + U^{\eta} \frac{\partial V}{\partial \eta} \right)$$

$$= -\left(\xi_y \frac{\partial p}{\partial \xi} + \eta_y \frac{\partial p}{\partial \eta} \right) + \mu (\alpha \frac{\partial^2 V}{\partial \xi^2} - 2\beta \frac{\partial^2 V}{\partial \xi \partial \eta} + \gamma \frac{\partial^2 V}{\partial \eta^2} \qquad (2.12)$$

$$+ \nabla^2 \xi \frac{\partial V}{\partial \xi} + \nabla^2 \eta \frac{\partial V}{\partial \eta})$$

The various coefficients that appear in the equations are given as,

$$\xi_x = \left(\frac{Y_{\eta}}{J} \right), \xi_y = -\left(\frac{X_{\eta}}{J} \right), \eta_x = -\left(\frac{Y_{\xi}}{J} \right), \eta_y = \left(\frac{X_{\xi}}{J} \right)$$

U^{ξ} and U^{η} are the fluid velocities in ξ and η direction given by

$$U^{\xi} = \xi_x U + \xi_y V$$
$$U^{\eta} = \eta_x U + \eta_y V \qquad (2.13)$$
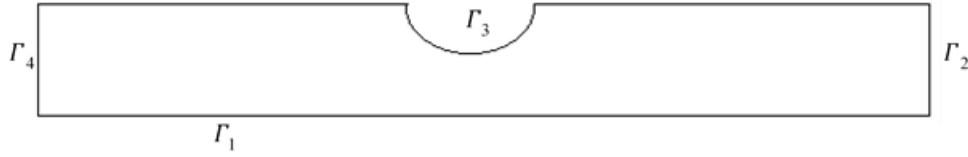
(a)
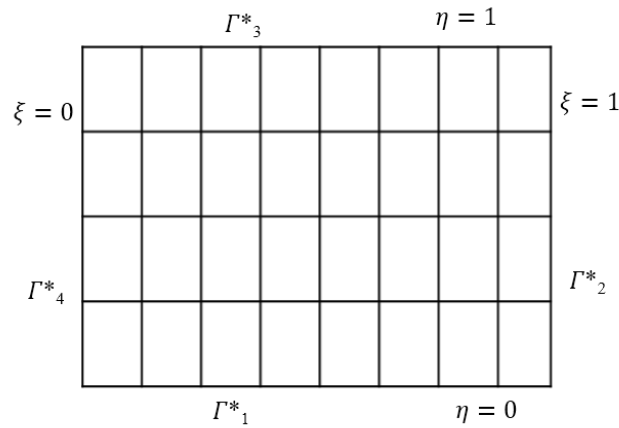
(b)

Figure 2.1 Illustrations of generation of body fitted grid systems. (a) Physical plane (b)Computational plane

2.4 Numerical scheme

For the purpose of capturing the unsteady physics of the flow we employ a semi-implicit, pressure correction type scheme, on a non- staggered structure body fitted grid mesh using a finite difference type of spatial discretisation. The concept of momentum interpolation of Rhie and Chow [29] is utilized in order to avoid grid scale pressure oscillation that can arise owing to decoupling between the velocity and pressure at grid points. The scheme was described by Hirsch [30] and is conceptually similar to SMAC algorithm described by Amsden and Harlow [31]. Guided by the works of Kim and Benson [32] and Cheng and Armfield [27] who have demonstrated the efficiency of SMAC scheme over SIMPLE, SIMPLEC and PISO methods for computing unsteady, incompressible flows, the present work uses a scheme that is similar to SMAC. The scheme has been implemented by Hasan and his co-workers [26]. The details of the scheme are spread over two sections. Time integration is presented in § 2.4.1 and spatial discretisation is discussed in § 2.4.2.

2.4.1 Time Integration

The flow field is marched forward in time using a two-step predictor-corrector approach. In the predictor step, the time integration of momentum equation is performed using a first order Euler method to obtain the guessed velocity field at the next time step. In the corrector the guessed velocity field obtained is corrected in to preserve using a pressure correction field to bring the divergence of the velocity field close to zero. The scheme is given as follows:

I. Predictor Step

At each grid point (i,j) the first order Euler integration in time of the momentum equation yields

$$\bar{U}_{i,j}^{n+1} = U_{i,j}^n + \delta\tau \left\{ H_{i,j}^n - \left(\left(\xi_x \frac{\partial p}{\partial \xi} \right)_{i,j}^n + \left(\eta_x \frac{\partial p}{\partial \eta} \right)_{i,j}^n \right) \right\} \qquad (2.14a)$$

$$\bar{V}_{i,j}^{n+1} = V_{i,j}^n + \delta\tau \left\{ G_{i,j}^n - \left(\left(\xi_y \frac{\partial p}{\partial \xi} \right)_{i,j}^n + \left(\eta_y \frac{\partial p}{\partial \eta} \right)_{i,j}^n \right) \right\} \qquad (2.11b)$$

Where superscript 'n' denotes the flow field at time level 'n', while the superscript 'n+1' denotes the flow field at time level 'n+1'.

The over bar is used to represent the guesses velocity components at time level 'n+1' which do not necessarily satisfy continuity. The terms $H_{i,j}^n$ and $G_{i,j}^n$ are the aggregates of the diffusive and convective terms at a grid point evaluated on the basis of the flow field at time level 'n'. Specifically the convective and diffusive terms are given in equation (2.15a) and (2.15a). Here the subscript u and v indicates the convective or diffusive flux in 'x' and 'y' directions.

$$C_u = U^\xi \frac{\partial U}{\partial \xi} + U^\eta \frac{\partial U}{\partial \eta}$$

$$C_v = U^\xi \frac{\partial V}{\partial \xi} + U^\eta \frac{\partial V}{\partial \eta}$$

(2.15a)

$$D_u = \mu(\alpha \frac{\partial^2 U}{\partial \xi^2} - 2\beta \frac{\partial^2 U}{\partial \xi \partial \eta} + \gamma \frac{\partial^2 U}{\partial \eta^2} + \nabla^2 \xi \frac{\partial U}{\partial \xi} + \nabla^2 \eta \frac{\partial U}{\partial \eta})$$

$$D_v = \mu(\alpha \frac{\partial^2 V}{\partial \xi^2} - 2\beta \frac{\partial^2 V}{\partial \xi \partial \eta} + \gamma \frac{\partial^2 V}{\partial \eta^2} + \nabla^2 \xi \frac{\partial V}{\partial \xi} + \nabla^2 \eta \frac{\partial V}{\partial \eta})$$

(2.12b)

II.   Corrector Step

In this step the guessed velocity field obtained in the predictor step is corrected in a vorticity preserving manner through a pressure correction field. The velocity and pressure corrections are:

$$U_{i,j}' = U_{i,j}^{n+1} - \bar{U}_{i,j}^{n+1}$$
$$V_{i,j}' = V_{i,j}^{n+1} - \bar{V}_{i,j}^{n+1}$$
$$p_{i,j}' = p_{i,j}^{n+1} - p_{i,j}^n$$

(2.16)

The velocity field at time level n+1 that satisfies continuity is coupled to the pressure field at a new time level n+1 through a semi-explicit discretisation in time of the momentum equations. This is given by,

$$U_{i,j}^{n+1} = U_{i,j}^n + \delta\tau \left\{ H_{i,j}^n - \left(\left(\xi_x \frac{\partial p}{\partial \xi}\right)_{i,j}^{n+1} + \left(\eta_x \frac{\partial p}{\partial \eta}\right)_{i,j}^{n+1} \right) \right\}$$

(2.17a)

$$V_{i,j}^{n+1} = V_{i,j}^n + \delta\tau \left\{ G_{i,j}^n - \left(\left(\xi_y \frac{\partial p}{\partial \xi}\right)_{i,j}^{n+1} + \left(\eta_y \frac{\partial p}{\partial \eta}\right)_{i,j}^{n+1} \right) \right\}$$

(2.14b)

The relationship between velocity and pressure can be obtained by subtracting equation (2.14a) from (2.17a) and (2.14a) from (2.17a). This yields the following relationships.

$$U'_{i,j} = -\delta\tau \left\{ \left(\xi_x \frac{\partial p'}{\partial \xi} + \eta_x \frac{\partial p'}{\partial \eta} \right)_{i,j} \right\}$$

$$V'_{i,j} = -\delta\tau \left\{ \left(\xi_y \frac{\partial p'}{\partial \xi} + \eta_y \frac{\partial p'}{\partial \eta} \right)_{i,j} \right\}$$

(2.18)

The pressure correction field must be such that it should enforce continuity at the new time level. The pressure Poisson equation is obtained by taking divergence of momentum equation with discrete divergence operator $\frac{\delta}{\delta x}$ and $\frac{\delta}{\delta y}$ below:

$$\frac{\delta}{\delta x} = \xi_x \frac{\partial}{\partial \xi} + \eta_x \frac{\partial}{\partial \eta}$$

$$\frac{\delta}{\delta y} = \xi_y \frac{\partial}{\partial \xi} + \eta_y \frac{\partial}{\partial \eta}$$

(2.19)

The continuity equation yield to :

$$\frac{\delta \bar{U}^{n+1}}{\delta x}_{i,j} + \frac{\delta \bar{V}^{n+1}}{\delta y}_{i,j} + \frac{\delta U'}{\delta x}_{i,j} + \frac{\delta V}{\delta y}_{i,j} = 0$$

(2.20)

The Poisson equation for Pressure correction is given by:

$$\frac{\delta}{\delta x}\left(\xi_x \frac{\partial p'}{\partial \xi} + \eta_x \frac{\partial p'}{\partial \eta} \right)_{i,j} + \frac{\delta}{\delta y}\left(\xi_y \frac{\partial p'}{\partial \xi} + \eta_y \frac{\partial p'}{\partial \eta} \right)_{i,j} = \left(\frac{1.0}{\delta \tau} \right)\left[\frac{\delta \bar{U}^{n+1}}{\delta x_{i,j}} + \frac{\delta \bar{V}^{n+1}}{\delta y_{i,j}} \right]$$

(2.21)

As the fluid cannot penetrate through the wall, the derivative of pressure correction (p') with the normal, $\frac{\partial p\prime}{\partial n}$, set to zero. At the inflow, velocity component is specified while $\frac{\partial p\prime}{\partial n}$ is set to zero and at the outflow boundary p' is set to zero.

It is observed that the velocity correction field as defined in equation ((2.18)) is irrotational in character. Thus the velocity associated with the guessed velocity field is preserved in the corrector step. The current method is similar to the SMAC method where the guessed velocity obtained from the momentum equations is corrected by adding irrotational velocity corrections to enforce continuity at the new time level. Equations (2.18) and (2.21) are used only in the interior to obtain the corrections and hence the flow field at the new time step. At the walls the no slip condition is explicitly specified for the velocities while the pressure at the wall and at inflow and outflow is obtained by applying momentum equation in the normal direction

2.4.2 Spatial Discretisation

The spatial discretisation of the equations (2.14a), (2.18), (2.21) is carried out using a finite difference methodology on a body fitted collocated mesh. For the interior nodes the convection terms are discretised using a hybrid scheme of a forth order, symmetric four point central differencing and a third order Taylor series based up-winding scheme. The up-winding scheme employs two point on the upstream side and one point on the downstream side of the grid point under consideration. The choice between the up-winding and central differencing is made on the basis of the local cell Peclet number. Here, Peclet number is defined on the basis of the difference between velocity in the directions of ξ,η (U^ξ and U^η). If $|Pe| < 2$ the central differencing is preferred otherwise up-winding is utilized. But for near boundary, central differencing scheme is used for discretising convective terms. The viscous terms are discretised using a forth order five-point, symmetric, central differencing in the interior while a second order three point, symmetric, central differencing scheme is utilized for the near boundary mesh points.

The discretisation of Pressure correction Poisson equation (PCPE, equation (2.21)) needs to be handled more carefully on a collocated grid. It is known that central discretisation of terms on both sides of equation (2.21) leads to an effective discrete equation on a mesh twice as coarse as the actual grid. Furthur, central discretisation of the divergence term on the right hand side of equation (2.21) results in pressure-velocity decoupling. These defects generally lead to spurious grid scale pressure oscillation [27]. In order to limit such non-physical solutions, discretisation of equation (2.21) is carried out as follows:

In equation (2.21) the divergence operator $\frac{\delta}{\delta x}$ is discretised as,

$$
\begin{aligned}
\frac{\delta}{\delta x}\left(\frac{\partial p'}{\partial x}\right) &= \left(\xi_x \frac{\partial}{\partial \xi} + \eta_x \frac{\partial}{\partial \eta}\right)\left(\frac{\partial p'}{\partial x}\right) = \left(\xi_x \frac{\partial}{\partial \xi} + \eta_x \frac{\partial}{\partial \eta}\right)\left(\xi_x \frac{\partial p'}{\partial \xi} + \eta_x \frac{\partial p'}{\partial \eta}\right) \\
&= \xi_x \frac{\partial}{\partial \xi}\left(\xi_x \frac{\partial p'}{\partial \xi} + \eta_x \frac{\partial p'}{\partial \eta}\right) + \eta_x \frac{\partial}{\partial \eta}\left(\xi_x \frac{\partial p'}{\partial \xi} + \eta_x \frac{\partial p'}{\partial \eta}\right)
\end{aligned}
\tag{2.22}
$$

The discretization of the first and second term of the right hand side of the equation (2.22) is given by (2.23) and (2.24)

$$
\xi_x \frac{\partial}{\partial \xi}\left(\xi_x \frac{\partial p'}{\partial \xi} + \eta_x \frac{\partial p'}{\partial \eta}\right)
\tag{2.23}
$$

$$= \frac{\xi_{xi,j}}{\Delta \xi} \left[\left(\xi_x \frac{\partial p'}{\partial \xi} + \eta_x \frac{\partial p'}{\partial \eta} \right)_{i+\frac{1}{2},j} - \left(\xi_x \frac{\partial p'}{\partial \xi} + \eta_x \frac{\partial p'}{\partial \eta} \right)_{i-\frac{1}{2},j} \right]$$

$$= \frac{\xi_{xi,j}}{\Delta \xi} \left[\begin{array}{c} \left(\left(\xi_x \frac{\partial p'}{\partial \xi} \right)_{i+\frac{1}{2},j} + \left(\eta_x \frac{\partial p'}{\partial \eta} \right)_{i+\frac{1}{2},j} \right) - \\ \left(\left(\xi_x \frac{\partial p'}{\partial \xi} \right)_{i-\frac{1}{2},j} + \left(\eta_x \frac{\partial p'}{\partial \eta} \right)_{i-\frac{1}{2},j} \right) \end{array} \right]$$

$$= \frac{\xi_{xi,j}}{\Delta \xi} \left[\begin{array}{c} \left(\xi_{x i+\frac{1}{2},j} \left(\frac{\partial p'}{\partial \xi} \right)_{i+\frac{1}{2},j} + \eta_{x i+\frac{1}{2},j} \left(\frac{\partial p'}{\partial \eta} \right)_{i+\frac{1}{2},j} \right) \\ - \left(\xi_{x i-\frac{1}{2},j} \left(\frac{\partial p'}{\partial \xi} \right)_{i-\frac{1}{2},j} + \eta_{x i-\frac{1}{2},j} \left(\frac{\partial p'}{\partial \eta} \right)_{i-\frac{1}{2},j} \right) \end{array} \right]$$

$$\eta_x \frac{\partial}{\partial \eta} \left(\xi_x \frac{\partial p'}{\partial \xi} + \eta_x \frac{\partial p'}{\partial \eta} \right)$$

$$= \frac{\eta_{xi,j}}{\Delta \eta} \left[\left(\xi_x \frac{\partial p'}{\partial \xi} + \eta_x \frac{\partial p'}{\partial \eta} \right)_{i,j+\frac{1}{2}} - \left(\xi_x \frac{\partial p'}{\partial \xi} + \eta_x \frac{\partial p'}{\partial \eta} \right)_{i,j-\frac{1}{2}} \right]$$

$$= \frac{\eta_{xi,j}}{\Delta \eta} \left[\begin{array}{c} \left(\left(\xi_x \frac{\partial p'}{\partial \xi} \right)_{i,j+\frac{1}{2}} + \left(\eta_x \frac{\partial p'}{\partial \eta} \right)_{i,j+\frac{1}{2}} \right) - \\ \left(\left(\xi_x \frac{\partial p'}{\partial \xi} \right)_{i,j-\frac{1}{2}} + \left(\eta_x \frac{\partial p'}{\partial \eta} \right)_{i,j-\frac{1}{2}} \right) \end{array} \right] \tag{2.24}$$

$$= \frac{\eta_{xi,j}}{\Delta \eta} \left[\begin{array}{c} \left(\xi_{x i,j+\frac{1}{2}} \left(\frac{\partial p'}{\partial \xi} \right)_{i,j+\frac{1}{2}} + \eta_{x i,j+\frac{1}{2}} \left(\frac{\partial p'}{\partial \eta} \right)_{i,j+\frac{1}{2}} \right) \\ - \left(\xi_{x i,j-\frac{1}{2}} \left(\frac{\partial p'}{\partial \xi} \right)_{i,j-\frac{1}{2}} + \eta_{x i,j-\frac{1}{2}} \left(\frac{\partial p'}{\partial \eta} \right)_{i,j-\frac{1}{2}} \right) \end{array} \right]$$

Mid way metrices and pressure correction gradients used in equations (2.23) and (2.24) are given by equation (2.25). In the equations below, $\overline{(a,b)}$ denotes the average of any two quantities a and b.

$$\left(\frac{\partial p'}{\partial \xi}\right)_{i+\frac{1}{2},j} = \left(\frac{p'_{i+1,j} - p'_{i,j}}{\Delta \xi}\right)$$

(2.25)

$$\left(\frac{\partial p'}{\partial \eta}\right)_{i+\frac{1}{2},j} = \overline{\left(\frac{\partial p'}{\partial \eta}\right)_{i+1,J}, \left(\frac{\partial p'}{\partial \eta}\right)_{i,J}} = \frac{p'_{i+1,j+1} - p'_{i+1,j-1} + p'_{i,j+1} - p'_{i,j-1}}{4\Delta \eta}$$

$$\xi_{x_{i+\frac{1}{2},j}} = \overline{\xi_{x_{i+1,J}}, \xi_{x_{i,J}}}$$

$$\left(\frac{\delta \overline{U}}{\delta x}\right)_{i,j}^{n+1} = \left(\xi_x \frac{\partial \overline{U}}{\partial \xi} + \eta_x \frac{\partial \overline{U}}{\partial \eta}\right)_{i,j}^{n+1} = \xi_{x_{i,j}} \left(\frac{\partial \overline{U}}{\partial \xi}\right)_{i,j}^{n+1} + \eta_{x_{i,j}} \left(\frac{\partial \overline{U}}{\partial \eta}\right)_{i,j}^{n+1}$$

(2.26)

$$\left(\frac{\delta \overline{U}}{\delta x}\right)_{i,j}^{n+1} = \frac{\xi_{x_{i,j}}}{\Delta x}\left(\overline{U}_{i+\frac{1}{2},j}^{n+1} - \overline{U}_{i-\frac{1}{2},j}^{n+1}\right) + \frac{\eta_{xi,j}}{\Delta \eta}\left(\overline{U}_{i,j+\frac{1}{2}}^{n+1} - \overline{U}_{i,j-\frac{1}{2}}^{n+1}\right)$$

The velocities $\overline{U}_{i+\frac{1}{2},j}^{n+1}$, $\overline{U}_{i-\frac{1}{2},j}^{n+1}$, $\overline{U}_{i,j+\frac{1}{2}}^{n+1}$ and $\overline{U}_{i,j-\frac{1}{2}}^{n+1}$ are obtained using a interpolation procedure known as momentum interpolation [28]. This is given as,

$$\overline{U}_{i+\frac{1}{2},j}^{n+1} = \left(\overline{Up_{i+1,j}^{n+1}, Up_{i,j}^{n+1}}\right) - \Delta \tau \left(\xi_x \frac{\partial p}{\partial \xi} + \eta_x \frac{\partial p}{\partial \eta}\right)_{i+\frac{1}{2},j}^{n}$$

$$\overline{U}_{i+\frac{1}{2},j}^{n+1} = \left(\overline{Up_{i+1,j}^{n+1}, Up_{i,j}^{n+1}}\right) - \Delta \tau \left\{\xi_{x_{i+\frac{1}{2},j}}^{n} \left(\frac{\partial p}{\partial \xi}\right)_{i+\frac{1}{2},j}^{n} + \eta_{x_{i+\frac{1}{2},j}}^{n} \left(\frac{\partial p}{\partial \eta}\right)_{i+\frac{1}{2},j}^{n}\right\}$$

(2.27a)

$$\overline{U}_{i-\frac{1}{2},j}^{n+1} = \left(\overline{Up_{i-1,j}^{n+1}, Up_{i,j}^{n+1}}\right) - \Delta \tau \left\{\xi_{x_{i-\frac{1}{2},j}}^{n} \left(\frac{\partial p}{\partial \xi}\right)_{i-\frac{1}{2},j}^{n} + \eta_{x_{i-\frac{1}{2},j}}^{n} \left(\frac{\partial p}{\partial \eta}\right)_{i-\frac{1}{2},j}^{n}\right\}$$

(2.24b)

$$\left(\frac{\partial p}{\partial \xi}\right)_{i+\frac{1}{2},j}^{n} = \left(\frac{p_{i+1,j}^{n} - p_{i,j}^{n}}{\Delta \xi}\right)$$

(2.28)

$$\left(\frac{\partial p}{\partial \eta}\right)_{i+\frac{1}{2},j}^{n} = \overline{\left(\frac{\partial p}{\partial \eta}\right)_{i+1,J}^{n}, \left(\frac{\partial p}{\partial \eta}\right)_{i,J}^{n}} = \frac{p_{i+1,j+1}^{n} - p_{i+1,j-1}^{n} + p_{i,j+1}^{n} - p_{i,j-1}^{n}}{4\Delta \eta}$$

The velocity $Up_{i,j}^{n+1}$ is obtained from equation (2.14a) without the pressure gradient term. In the discretisation schemes in equation (2.22) and (2.25), the momentum interpolation procedure given in equation (2.27a) maintains the coupling between the pressure and velocity field.

A procedure similar to the discretisation of $\frac{\delta}{\delta x}$ (equation (2.28)) is adopted for $\frac{\delta}{\delta y}$ discretisation which will lead to discrete pressure correction Poisson equation (PCPE),

$$[A]\{p'\} = [Q] \tag{2.29}$$

This discretisation procedure discretises PCPE to a nine point molecule structure. The different components of $[A]$ in equation (2.29) are given in equation (2.30a) and of $[Q]$ are given in equation (2.31)

$$
\begin{aligned}
a_{i+1,j} = &\left(\frac{\xi_{xi,j}}{2(\Delta\xi)^2} \left(\xi_{x\,i,j} + \xi_{x\,i+1,j} \right) \right) + \left(\frac{\xi_{yi,j}}{2(\Delta\xi)^2} \left(\xi_{y\,i,j} + \xi_{y\,i+1,j} \right) \right) \\
&+ \left(\frac{\eta_{xi,j}}{8\Delta\xi\Delta\eta} \left(\xi_{x\,i,j+1} - \xi_{x\,i,j-1} \right) \right) + \left(\frac{\eta_{y\,i,j}}{8\Delta\xi\Delta\eta} \left(\xi_{y\,i,j+1} - \xi_{y\,i,j-1} \right) \right)
\end{aligned} \tag{2.30a}
$$

$$
\begin{aligned}
a_{i-1,j} = &\left(\frac{\xi_{xi,j}}{2(\Delta\xi)^2} \left(\xi_{x\,i,j} + \xi_{x\,i-1,j} \right) \right) + \left(\frac{\xi_{yi,j}}{2(\Delta\xi)^2} \left(\xi_{y\,i,j} + \xi_{y\,i-1,j} \right) \right) \\
&+ \left(\frac{\eta_{xi,j}}{8\Delta\xi\Delta\eta} \left(\xi_{x\,i,j-1} - \xi_{x\,i,j+1} \right) \right) + \left(\frac{\eta_{y\,i,j}}{8\Delta\xi\Delta\eta} \left(\xi_{y\,i,j-1} - \xi_{y\,i,j+1} \right) \right)
\end{aligned} \tag{2.27b}
$$

$$
\begin{aligned}
a_{i,j+1} = &\left(\frac{\eta_{xi,j}}{2(\Delta\eta)^2} \left(\eta_{x\,i,j} + \eta_{x\,i,j+1} \right) \right) + \left(\frac{\eta_{yi,j}}{2(\Delta\eta)^2} \left(\eta_{y\,i,j} + \eta_{y\,i,j+1} \right) \right) \\
&+ \left(\frac{\xi_{xi,j}}{8\Delta\xi\Delta\eta} \left(\xi_{x\,i+1,j} - \xi_{x\,i-1,j} \right) \right) + \left(\frac{\xi_{y\,i,j}}{8\Delta\xi\Delta\eta} \left(\xi_{y\,i+1,j} - \xi_{y\,i-1,j} \right) \right)
\end{aligned} \tag{2.27c}
$$

$$
\begin{aligned}
a_{i,j-1} = &\left(\frac{\eta_{xi,j}}{2(\Delta\eta)^2} \left(\eta_{x\,i,j} + \eta_{x\,i,j-1} \right) \right) + \left(\frac{\eta_{yi,j}}{2(\Delta\eta)^2} \left(\eta_{y\,i,j} + \eta_{y\,i,j-1} \right) \right) \\
&+ \left(\frac{\xi_{xi,j}}{8\Delta\xi\Delta\eta} \left(\xi_{x\,i-1,j} - \xi_{x\,i+1,j} \right) \right) + \left(\frac{\xi_{yi,j}}{8\Delta\xi\Delta\eta} \left(\xi_{y\,i-1,j} - \xi_{y\,i+1,j} \right) \right)
\end{aligned} \tag{2.27d}
$$

$$
\begin{aligned}
a_{i+1,j+1} = &\left(\frac{\xi_{xi,j}}{8\Delta\xi\Delta\eta} \left(\eta_{x\,i,j} + \eta_{x\,i+1,j} \right) \right) + \left(\frac{\xi_{yi,j}}{8\Delta\xi\Delta\eta} \left(\xi_{y\,i,j} + \xi_{y\,i+1,j} \right) \right) \\
&+ \left(\frac{\eta_{xi,j}}{8\Delta\xi\Delta\eta} \left(\xi_{x\,i,j} + \xi_{x\,i,j+1} \right) \right) + \left(\frac{\eta_{y\,i,j}}{8\Delta\xi\Delta\eta} \left(\eta_{y\,i,j} + \eta_{y\,i,j+1} \right) \right)
\end{aligned} \tag{2.27e}
$$

$$a_{i-1,j-1} = \left(\frac{\xi_{xi,j}}{8\Delta\xi\Delta\eta}\left(\eta_{x\,i,j} + \eta_{x\,i-1,j}\right)\right) + \left(\frac{\xi_{yi,j}}{8\Delta\xi\Delta\eta}\left(\xi_{y\,i,j} + \xi_{y\,i-1,j}\right)\right)$$
$$+ \left(\frac{\eta_{xi,j}}{8\Delta\xi\Delta\eta}\left(\xi_{x\,i,j} + \xi_{x\,i,j-1}\right)\right) + \left(\frac{\eta_{y\,i,j}}{8\Delta\xi\Delta\eta}\left(\eta_{y\,i,j} + \eta_{y\,i,j-1}\right)\right)$$

(2.27f)

$$a_{i-1,j+1} = \left(\frac{\xi_{xi,j}}{8\Delta\xi\Delta\eta}\left(\eta_{x\,i,j} + \eta_{x\,i-1,j}\right)\right) + \left(\frac{\xi_{yi,j}}{8\Delta\xi\Delta\eta}\left(\xi_{y\,i,j} + \xi_{y\,i-1,j}\right)\right)$$
$$+ \left(\frac{\eta_{xi,j}}{8\Delta\xi\Delta\eta}\left(\xi_{x\,i,j} + \xi_{x\,i,j+1}\right)\right) + \left(\frac{\eta_{y\,i,j}}{8\Delta\xi\Delta\eta}\left(\eta_{y\,i,j} + \eta_{y\,i,j+1}\right)\right)$$

(2.27g)

$$a_{i+1,j-1} = \left(\frac{\xi_{xi,j}}{8\Delta\xi\Delta\eta}\left(\eta_{x\,i,j} + \eta_{x\,i+1,j}\right)\right) + \left(\frac{\xi_{yi,j}}{8\Delta\xi\Delta\eta}\left(\xi_{y\,i,j} + \xi_{y\,i+1,j}\right)\right)$$
$$+ \left(\frac{\eta_{xi,j}}{8\Delta\xi\Delta\eta}\left(\xi_{x\,i,j} + \xi_{x\,i,j-1}\right)\right) + \left(\frac{\eta_{y\,i,j}}{8\Delta\xi\Delta\eta}\left(\eta_{y\,i,j} + \eta_{y\,i,j-1}\right)\right)$$

(2.27h)

$$a_{i,j} = \left(-\frac{\xi_{xi,j}}{2(\Delta\xi)^2}\left(\xi_{x\,i+1,j} + 2\xi_{x\,i,j} + \xi_{x\,i-1,j}\right)\right)$$
$$+ \left(-\frac{\xi_{yi,j}}{2(\Delta\xi)^2}\left(\xi_{y\,i+1,j} + 2\xi_{y\,i,j} + \xi_{y\,i-1,j}\right)\right)$$
$$+ \left(-\frac{\eta_{xi,j}}{2(\Delta\eta)^2}\left(\eta_{x\,i,j+1} + 2\eta_{x\,i,j} + \eta_{x\,i,j-1}\right)\right)$$
$$+ \left(-\frac{\eta_{yi,j}}{2(\Delta\eta)^2}\left(\eta_{y\,i,j-1} + 2\eta_{y\,i,j} + \eta_{y\,i,j+1}\right)\right)$$

(2.27i)

$$Q_{i,j} = \frac{1}{\Delta\tau}\left[\xi_{xi,j}\left[\frac{\overline{U}_{i+\frac{1}{2},j} - \overline{U}_{i-\frac{1}{2},j}}{\Delta\xi}\right] + \eta_{xi,j}\left[\frac{\overline{U}_{i,j+\frac{1}{2}} - \overline{U}_{i,j-\frac{1}{2}}}{\Delta\eta}\right]\right.$$
$$\left. + \xi_{yi,j}\left[\frac{\overline{V}_{i+\frac{1}{2},j} - \overline{V}_{i-\frac{1}{2},j}}{\Delta\xi}\right] + \eta_{y\,i,j}\left[\frac{\overline{V}_{i,j+\frac{1}{2}} - \overline{V}_{i,j-\frac{1}{2}}}{\Delta\eta}\right]\right]$$

(2.31)

The discrete PCPE is then solved numerically with the help of nine point SIP procedures as in by Peric.

The first order explicit Euler time integration in the predictor step has been preferred as the problem is well posed. The nature of the scheme (explicit, first order in time) does imposes restrictions on the allowable time step owing to stability and accuracy considerations. An implicit scheme would have allowed a larger time step but this advantage would be offset by two factors. Firstly an additional Poisson equation in addition to the PCPE, has to be solved which would increase the computational effort required. Secondly because of the highly unsteady nature of the problem, the time step has to be kept sufficiently small.

2.5 Boundary and Initial Conditions

In the numerical scheme employed, boundary conditions have to be specified for velocities, pressure correction field and pressure field. Three different velocity field conditions are given at the inflow portion. A uniform velocity profile, a pulsatile sinusoidal velocity profile and a non-sinusoidal velocity profile is given at the inlet. The no-slip and the no-penetration, boundary conditions for the velocity components are specified at the rigid wall. At the outflow boundary the axial diffusion in both of the momentum equation is neglected for every y. At the solid walls and at the inflow boundary, the gradient of pressure correction field in the normal direction is taken to be zero. At the outflow the pressure correction is taken to be zero. The conditions on pressure correction are essentially the same as employed in [27]. The pressure on the solid walls and on the inflow and outflow boundary is updated by obtaining the value of pressure gradient in the normal direction from the full momentum equations as follows:

$$\frac{\partial p}{\partial \eta} = \left(\frac{\partial p}{\partial x}\right)\left(\frac{\partial x}{\partial \eta}\right) + \left(\frac{\partial p}{\partial y}\right)\left(\frac{\partial y}{\partial \eta}\right) \tag{2.32}$$

The pressure gradients in the x and y directions at the boundaries are obtained through the x and y momentum equations respectively.

2.6 Validation of Computational Methodology

Two of the classical flows treated in introductory fluid mechanics lectures are laminar, fully developed pipe flow, in other words, the so-called Hagen-Poiseuille flow, and the corresponding plane channel flow. The development of these flows from pre-assigned velocity profiles require certain axial distances from the pipe or the channel inlet. Irrespective of a particular inlet velocity profile or what happens in detail at the entrance of a pipe or a channel, the physical mechanisms behind such axial development of a flow are well established and understood. Owing to the no-slip velocity condition at walls, the fluid next to the wall is

immediately slowed as soon as the flow enters a pipe or a channel. This retardation near the wall spreads inwards owing to viscous effects and the slowed-down fluid close to the wall causes the fluid in the centre to move faster, since the cross-sectional mass flow rate at any axial location remains constant. Ultimately, moving in the flow direction, the fully developed state of the flow is reached, i.e., the parabolic velocity distribution of the Hagen-Poiseuille flow develops. The closest location from the entrance where this phenomenon occurs defines the hydrodynamic entrance length as the distance from the inlet of the pipe to the location of the fully developed pipe flow or the corresponding position of the fully developed channel flow.

There have been numerous investigations of the development length for laminar pipe and channel flows, carried out not only using various approximate analytical methods, but also by performed numerical and experimental investigations. Good summaries of the work in the past are provided in Schlichting[22]. Using the above mentioned principles the code has been validated by using the velocity profiles and entrance lengths for different physical parameters and compared with given experimental and theoretical results. We have seen the flow development in the channel and plotted the centreline velocities. Figure 2. 1 shows the development of the centreline velocity along the axial length of the channel for Re values of 100, 300, 500 and 750. The centreline velocity increases in the developing region and reaches a maximum value of 1.5 times the inlet velocity which has been validated from literature. Also the entrance length can also be seen from the same graphs upto the region where the velocity has attained a constant value. A number of researchers have agreed upon L/D in a channel to be approximately 0.05*Re which has been approximately achieved in our results as shown in Table 2.1. Figure 2.2 shows the development of the velocities at different axial locations along the length of the channel for various Re and their analytical values at the fully developed condition are also plotted in the same graph. It clearly shows that the fully developed velocity profile is attained at a later point for higher Re. A good approximation closer to the analytical values are also achieved.

Table 2.1 Entrance lengths in a channel for different Re

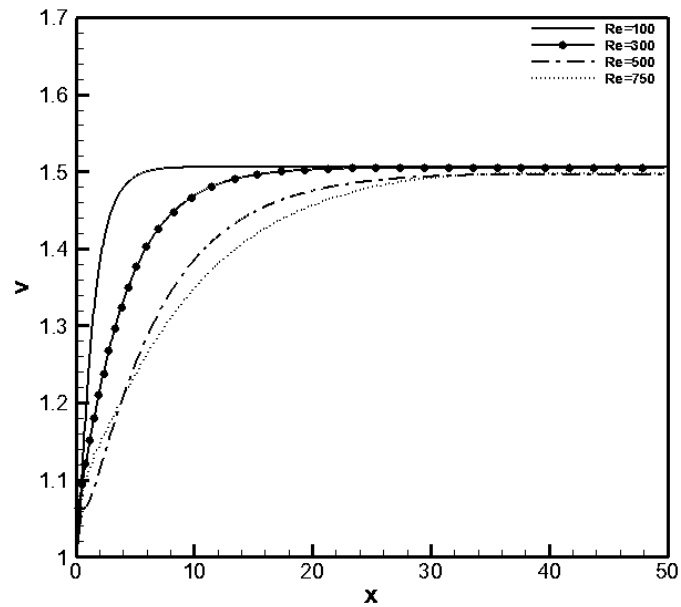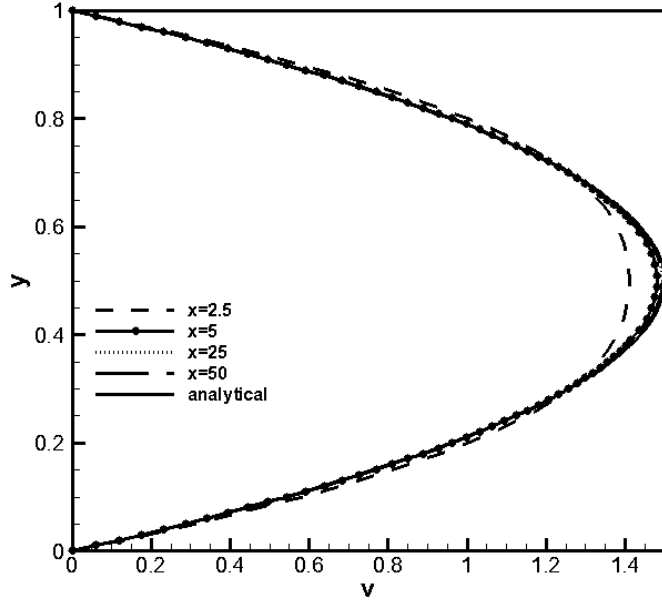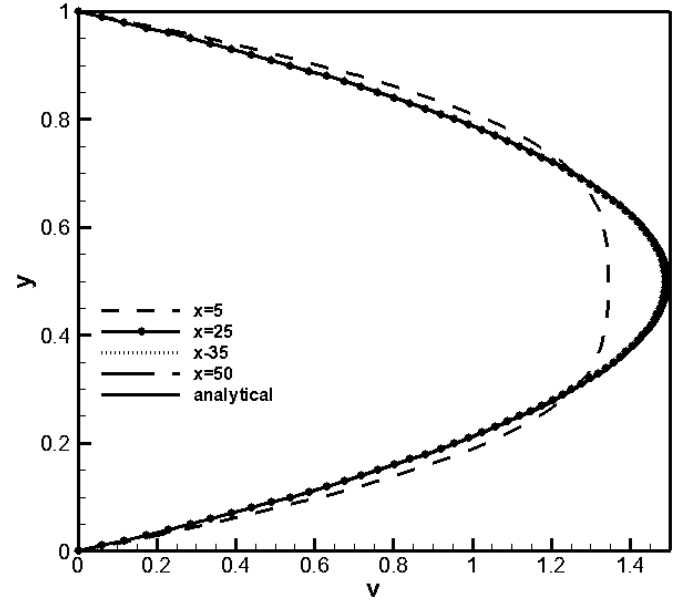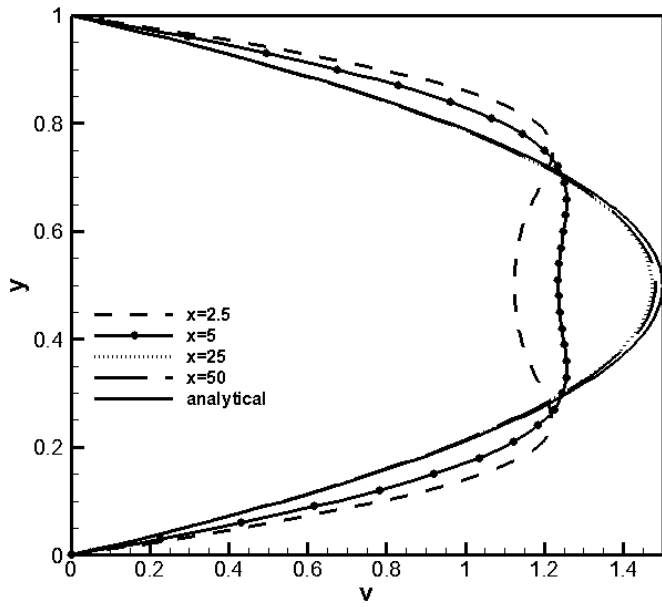| Re	Present	Analytical [35]	% difference
100	5	5	0
300	14.99	15	0.06
500	25.2	25	0.2
750	38.1	37.5	1.6

Figure 2. 1 Axial development of the centreline velocities along the length of the channel for Re=100, 300, 500, 750
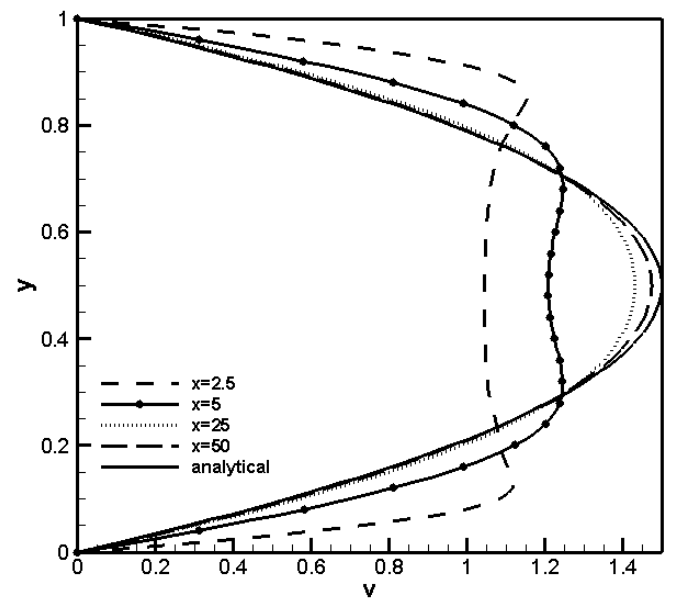
Figure 2.2 Development of velocities at different axial positions for (a) Re=100, (b) Re=300,
(c) Re=500 and (d) Re=750

2.7 Grid Independence

The grid independence studies were performed by varying the number of grid points in the x and y direction. Five different grids having 991×101, 1021×101, 1221×101, 91×1021, 121×1021 points with the dimensionless time step fixed at 1×10^{-4} as shown in Figure 2.3 and Figure 2.4 separately for grid variations along x and y directions. The velocity profile is recorded at different locations along the length of the channel(x) at a given instant. This velocity profile is used for grid independence and time independence studies. Grid convergence is achieved at 1021×101 and hence subsequent simulations were performed at this grid.
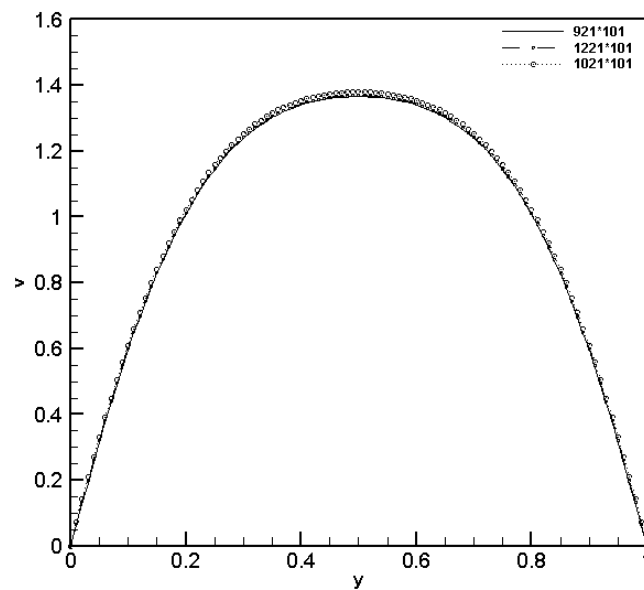
Figure 2.3 U velocity variation along y-axis at $\tau = 1.46$ for different grids 991×101, 1021×101 and 1221×101
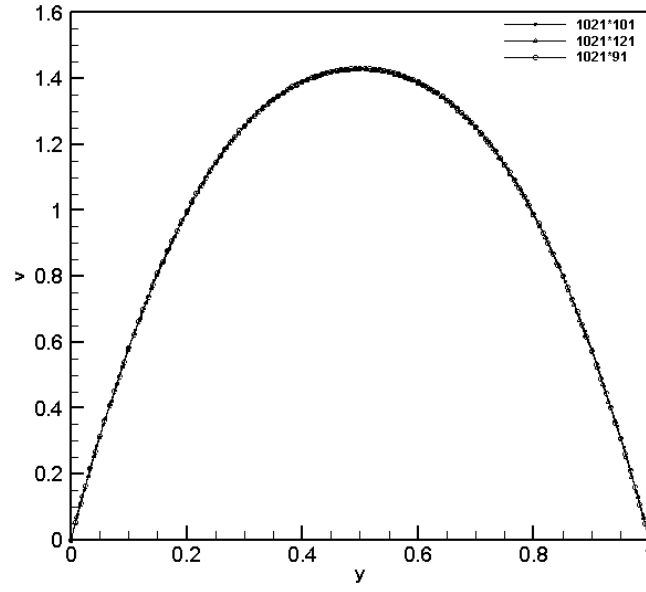
Figure 2.4 U velocity variation along y-axis at $\tau = 1.48$ for different grids 1021×101, 1021×121 and 1021×91

To establish the time step for simulations, time independence study was carried out for two different time steps of 1×10^{-4} and 2×10^{-4} . The velocity profile recorded looked almost identical at these time steps, hence the time step of 1×10^{-4} is fixed.
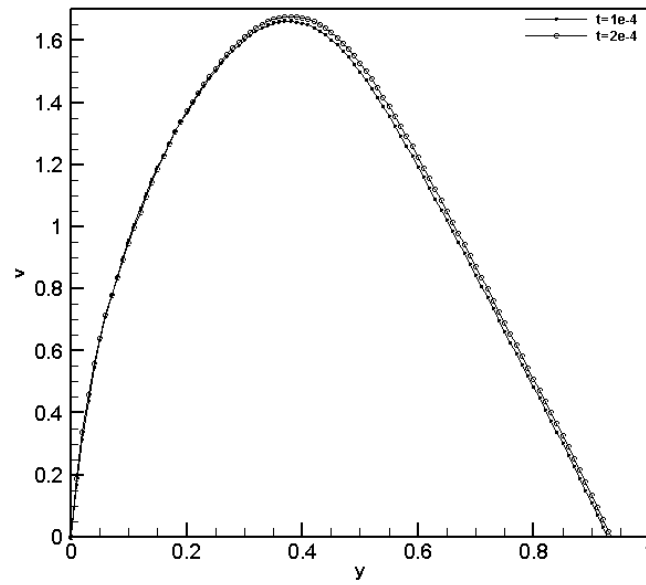
Figure 2. 2 Velocity variation along y-axis(x=50) at $\tau = 0.5$ for different time steps (dt) 0.0001 and 0.0002.

Chapter 3 Results and Discussions

Table 3.1 gives a summary of the various simulations that are performed for the current study. Reynolds number of 750 and 500 and Strouhal number of 0.024 and 0.048 are taken. Thus we get Womersely number in the range of 5.32 to 7.52 which is in the physiological range. All the computations are performed on 1021×101 mesh.

Table 3.1 Various simulations in the current study

Type of flow	Inflow velocity	Re	St	Wo
Newtonian	Uniform	750	-	-
		500	-	-
	Sinusoidal	750	0.024	5.32
		500	0.024	4.34
		750	0.048	7.52
		500	0.048	6.14
	Non-sinusoidal	750	0.024	5.32
		500	0.024	4.34
		750	0.048	7.52
		500	0.048	6.14
Non-Newtonian	Uniform	750	-	-
		500	-	-
	Sinusoidal	750	0.024	5.32
		500	0.024	4.34
		750	0.048	7.52
		500	0.048	6.14
	Non-sinusoidal	750	0.024	5.32
		500	0.024	4.34
		750	0.048	7.52
		500	0.048	6.14

We have first considered the uniform flow of blood under the influence of a constant velocity at inlet and recorded the variation of velocity profile and wall shear rate along the axial length with Re and St. This has been discussed in § 3.1. We have then considered the effect of pulsatile velocity profile (sinusoidal) on the flow dynamics and recorded the variation of flow properties with time by varying the Re and St in § 3.2 A sinusoidal incoming flow is commonly used in theoretical and experimental studies of flow in non-uniform vessels [15]. However, this is not realistic for the physiological case of flow in large blood vessels where there is a double pulse with the velocity during systole much greater than during diastole. Hence we have studied the effects of a non- sinusoidal incoming flow which is discussed in § 3.3. In § 3.4 we have done a comparative analysis between Newtonian and non-Newtonian flow.

3.1 Uniform Inflow

In Figure 3.1, the axial velocity profiles upstream of, at the peak of and downstream of the stenosis during uniform inflow at Re 500 are given. This shows the velocity profile pattern changes with the stenosis and regains the pattern away from the stenosis downstream of the channel. Also the velocity profile of the shear thinning model shows maximum difference from the Newtonian downstream of the stenosis, the difference of centreline velocities is 13%.
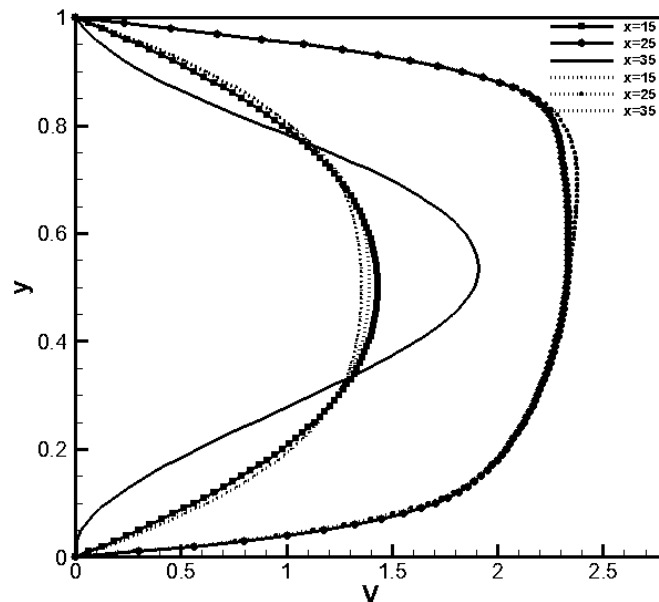

Figure 3.1 Centerline X-Velocity upstream of, at the peak of and downstream of the stenosis (Re=500). Solid lines are for Newtonian fluid and dashed lines are for shear-thinning fluid.

Figure 3.2 and Figure 3.3 show the streamlines for Newtonian fluid and shear thinning fluid at Reynolds no. 500. The figures show a zoomed section between x=24 and x=30. The zoomed section shows the recirculation zone that appears just downstream of the stenosis. The recirculation zone is larger in case of Newtonian fluid (upto x=29.84 for Re=500) than shear-thinning fluid (upto x=28.14) for the same Re as shown in Table 3.2. There is a point of separation at the point of peak constriction and later reattachment occurs downstream of stenosis. As expected it could be observed from Figure 3.4 and Figure 3.5 that the length of recirculation zone increases on increasing the Reynolds number. It stretches upto x=32.58 for the Newtonian fluid and x=29.26 for Non-Newtonian model of fluid for Re=750.
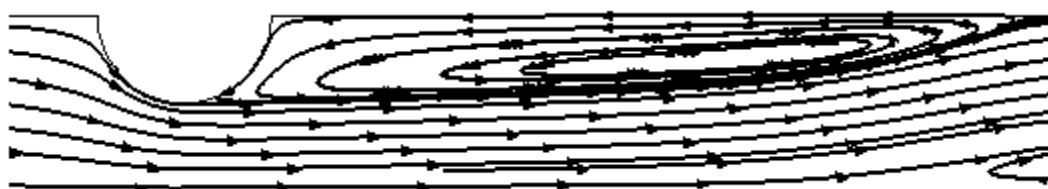

Figure 3.2 Streamlines for Newtonian fluid at Re=500, Zoomed between x=24 and 30.

Figure 3.3 Streamlines for Non-Newtonian fluid at Re=500, zommed between x=24 and 30.

Figure 3.4 Streamlines for Newtonian fluid at Re=750, Zoomed between x=24 and 30.

Figure 3.5 Streamlines for Non-Newtonian fluid at Re=750, zommed between x=24 and 30.

Table 3.2 Separation point and Re-attachment length for Newtonian and Non-Newtonian flows (uniform inflow)

Type of flow	Re	Separation point at y=1	Reattachment length at y=1
Newtonian	750	24.96	32.58
	500	25.03	29.84
Non-Newtonian	750	25.18	29.26
	500	25.15	28.14
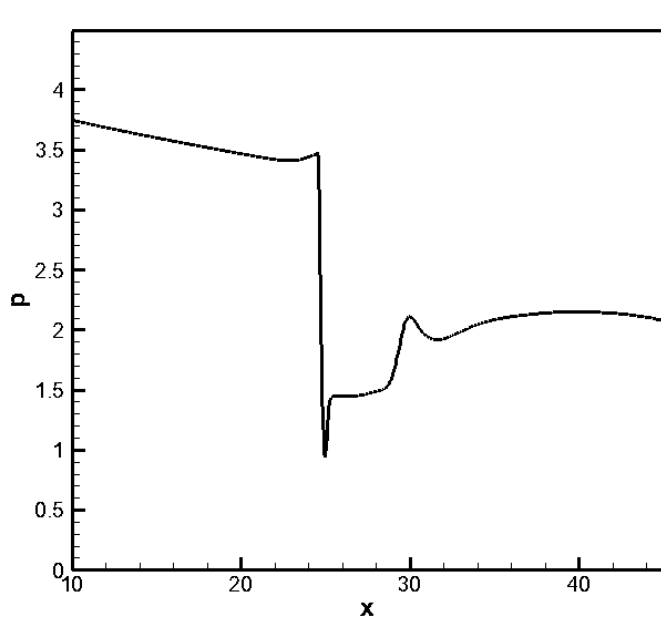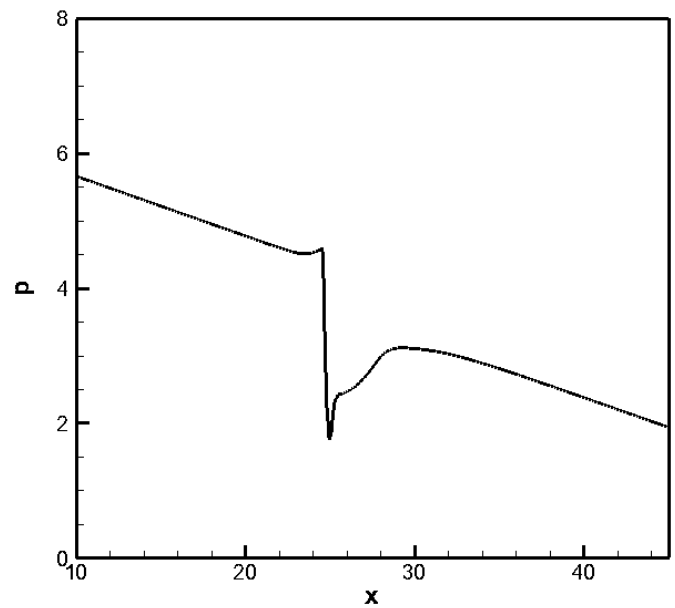
(a)   (b)

Figure 3.6 Pressure variation along the length of channel at top wall (a) Newtonian fluid (b) Non-Newtonian fluid for Re=750

Figure 3.6(a) and Figure 3.6(b) show the pressure variation along the top wall of the channel for the two different flows. It can be seen that there is fluctuation in pressure just after the peak stenosed region. In the region before the stenosis, pressure gradient is identical in both the cases. However since large separated zone is observed in Newtonian case , a steep linear pressure gradient is observed in non-Newtonian case. Also a pressure drop cause by the stenosis is observed. Similar is the case with wall vorticity profile as shown in Figure 3.7(a) and Figure 3.7(b) for Newtonian and non-Newtonian fluid respectively. The peak vorticity is higher for the non-Newtonian flow than the Newtonian flow and attains a steady value downstream.
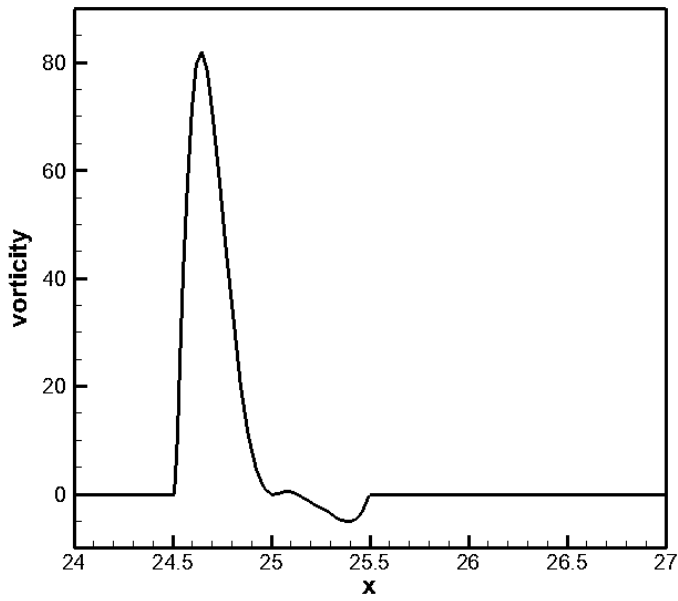
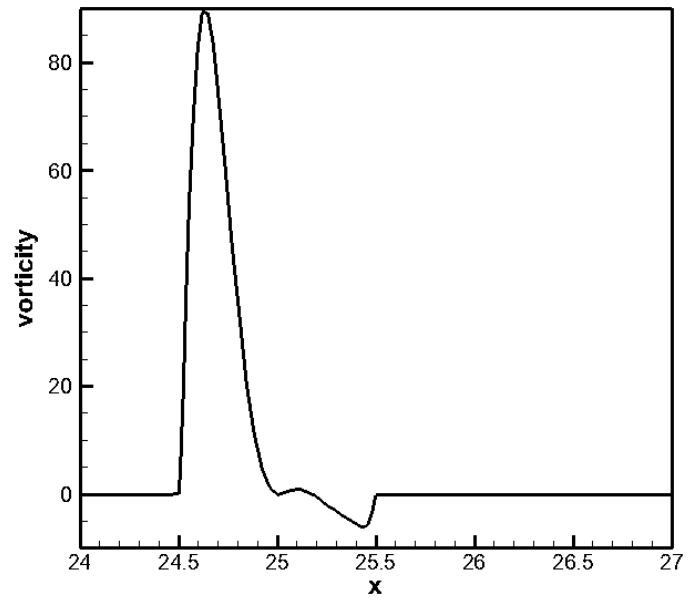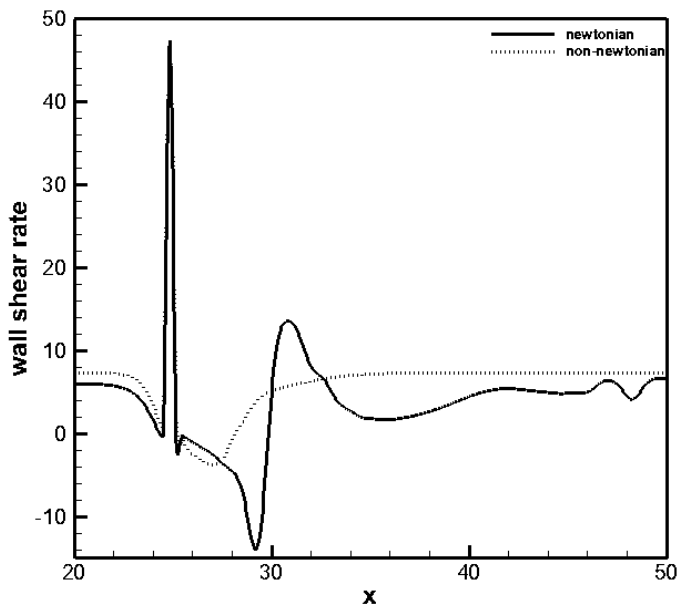(a)   (b)

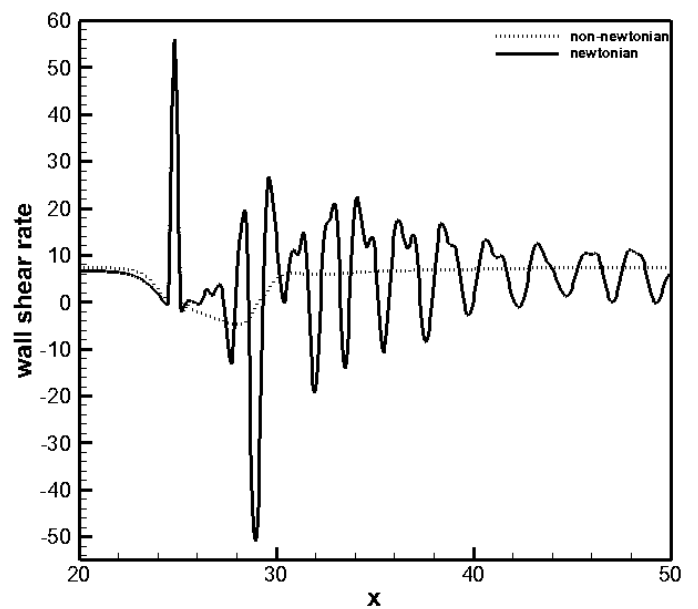Figure 3.7 Vorticity variation along the length of channel at top wall (a) Newtonian fluid (b) Non-Newtonian fluid for Re=750

(a)   (b)

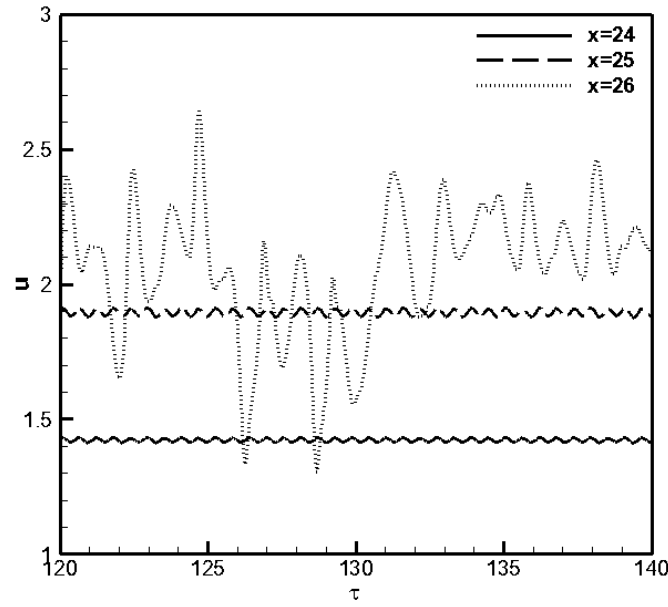Figure 3.8 Wall shear rate variation along channel length (a) Re=500 (b) Re=750

Figure 3.9 Time histories of centreline X-velocities along the length of channel (Newtonian flow)at three different x-locations for Re=750

The variation of wall shear rate for Newtonian and shear thinning fluid along the channel length is given in Figure 3.8(a) and Figure 3.8(b). This shows that the peak wall shear rate increases with increasing Re. The peak wall shear rate is slightly higher for the shear thinning model of fluid than for the newtonian fluid which shows the same trend as given by Nandakumar et al [7] for a lesser constriction The difference in the peak wall shear rate for the channel for Newtonian flow with uniform inflow is calculated to be 0.35% for Re=500 and 1.49% for Re=750. It can also be seen that initially both the fluids have almost the same wall shear rate till the stenotic region is reached. Also, the recirculation zone present downstream of the stenosis leads to a reduction in wall shear stresses below its upstream value. Again furthur downstream and away from the stenosis, the shear stress recovers its initial pre-stenosis value as can be seen in case of Re 500.

Figure 3.9 shows the time of evolution of the centerline velocities at three different locations along the channel length. x=24 refers to a region just before the stenosis. x=25 at the peak stenosis point and x=26 is a region after the stenosis. We can see that the velocity attains a uniform pattern in the region before stenosis and at peak stenosis while there are fluctuations in the velocity pattern downstream of the stenosis. This could be due to the recirculation zone created downstream.
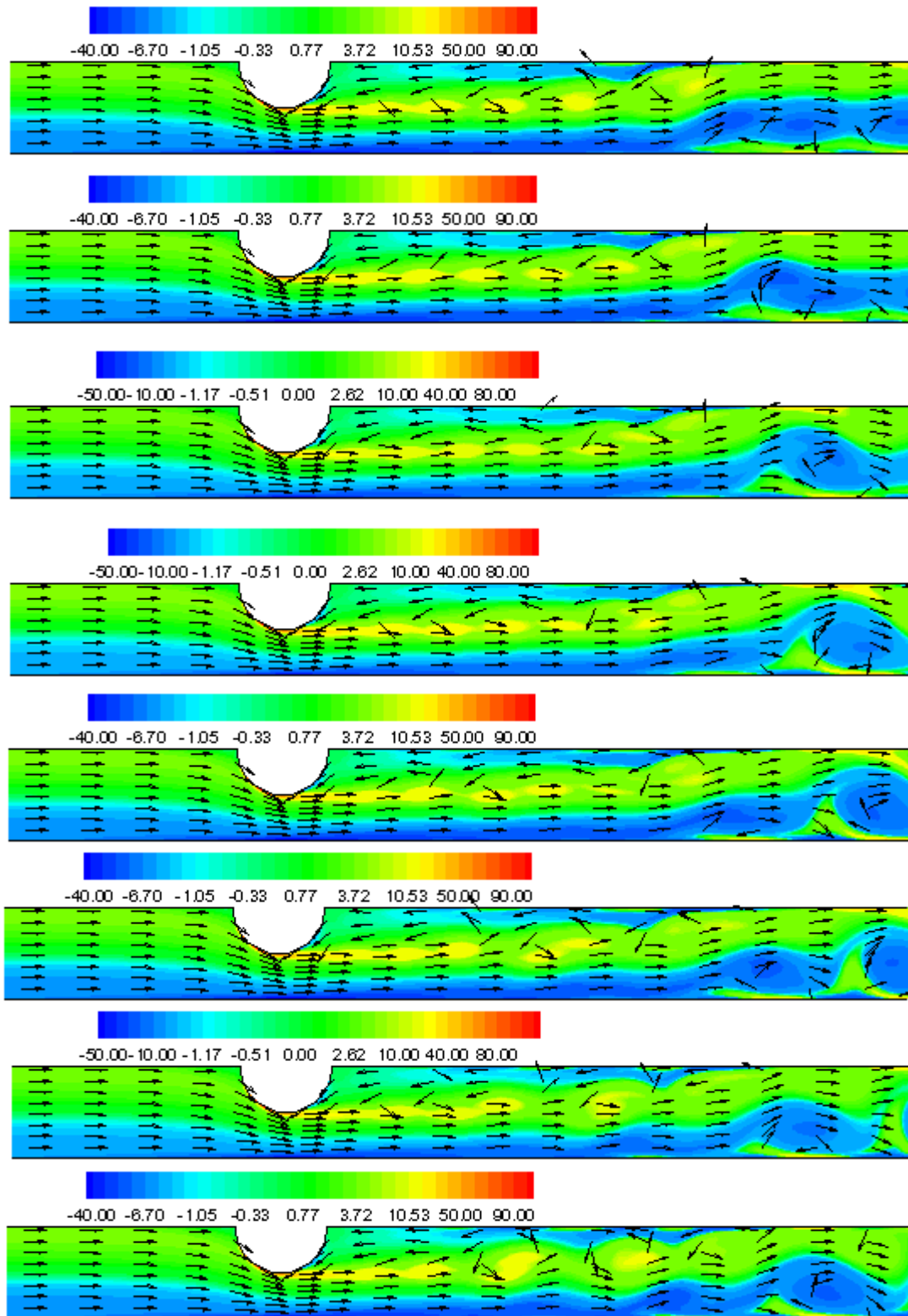
Figure 3.10 Vorticity and velocity vector plots with time for uniform inflow velocity (Newtonian flow) at a time interval of $\tau = 0.1$ for Re=750(x=22 to 32)

Figure 3.10 shows the development of vorticity and velocity vector plots with time for uniform inflow velocity in the channel.For all the flows, these plots are shown in a section of channel (x=22 to 32) for clarity purpose. As expected for flow in a channel the region prior to stenosis shows a uniform developed velocity profile and there is no change in the velocity pattern with time. However in the region after the stenosis there is a gradual change in velocity pattern. The vortex waves which are generated downstream gradually change their shape and size and also change their position as can be observed in the above plots. In case of non-Newtonian flow, for uniform inflow velocity, the streamlines attain a steady pattern with time as shown in Figure 3.5.

3.2 Sinusoidal inflow

We will now consider the effect of a sinusoidal velocity given in equation (3.1) on the flow dynamics as shown in Figure 3.11

$$V = 0.5[1 - cos(2\pi St\tau)] \tag{3.1}$$

Where St is the Strouhal number given by $St = {D}/{UT}$ where D is the unperturbed width of the channel, U is the free stream velocity and T is the time taken for a complete cycle of the flow. This sinusoidal inflow velocity profile is considered as a prototype of the physiological waveform in past experimental studies. Here we will consider a number of different cases. We take the velocity to be sinusoidal with a minimum value of zero and Reynolds number and Strouhal number of 750 and 0.024 respectively. We will then consider the effect of changing the Reynolds number and separately the Strouhal number. The Womersley number of the calculations varies from 3 to 7.5 which are within the range of physiological interest.
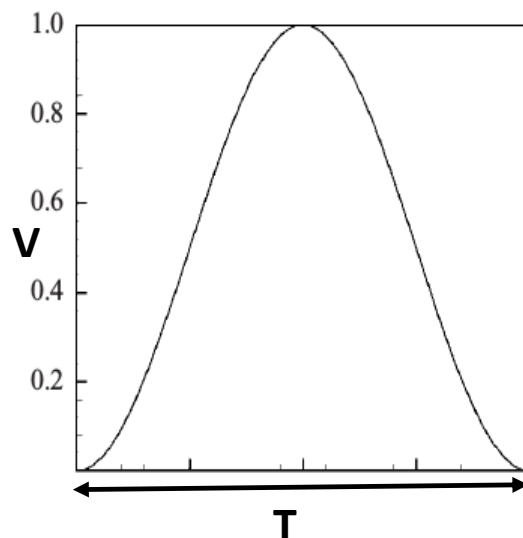

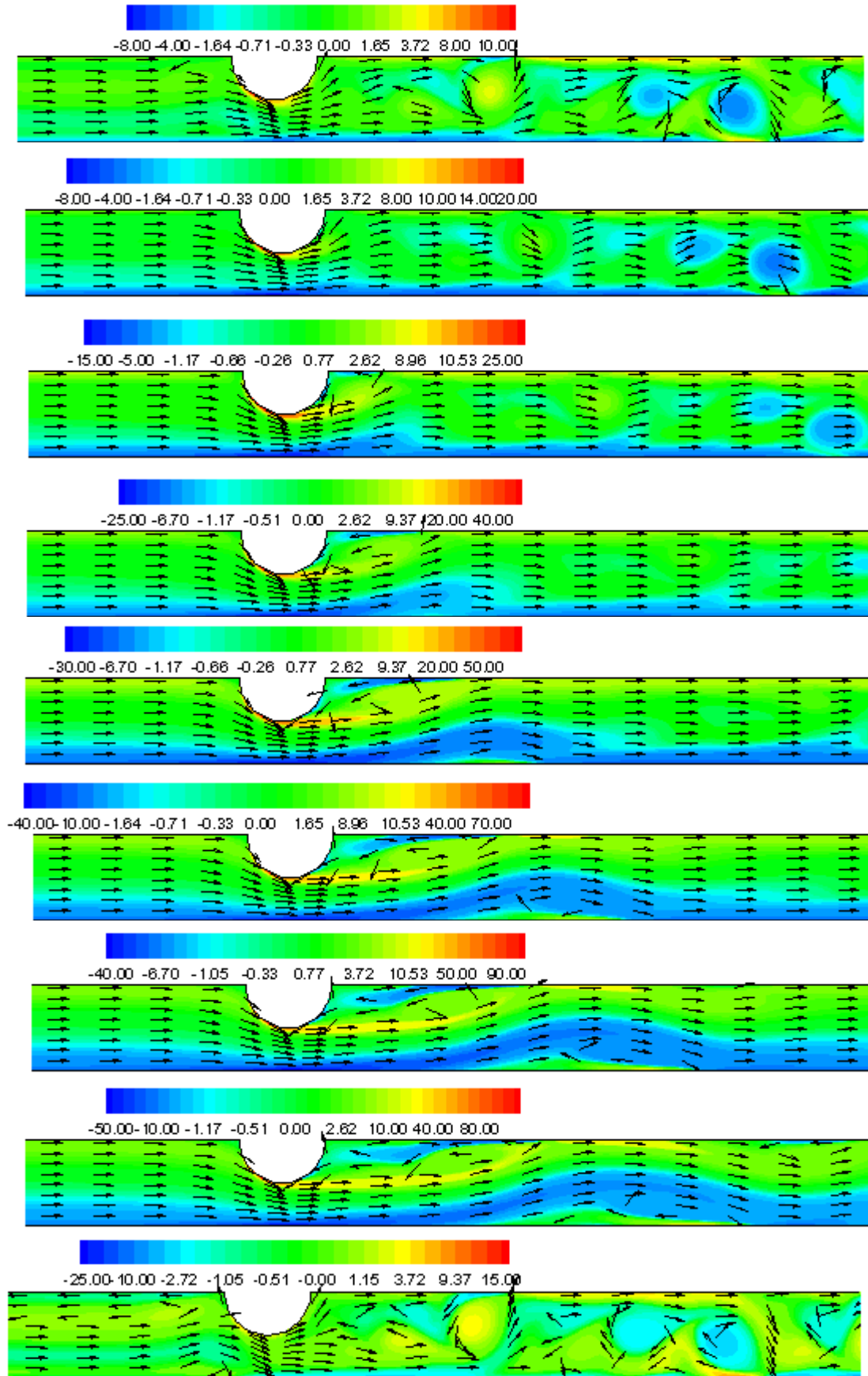Figure 3.11 Sinusoidal Inflow velocity profile [10]

Figure 3.12 Vorticity and velocity vector plots for sinusoidal flow(Newtonian) with Re=750 and St=0.024(x=22 to 32) at equal intervals in a cycle

The vorticity and velocity plots for the flow with Re 750 and St=0.024 are shown in Figure 3.12 for different time steps in a cycle at equal intervals. 10 time steps at equal intervals are taken in a cycle. For the first case in Figure 3.12, last snapshot shows the end of cycle. Small clockwise and anticlockwise vortex waves are formed in the initial stage of the cycle which decay as the cycle proceeds and re-attain the previous stage towards the completion of the cycle. During the cycle a vorticity wave is generated downstream of the constriction. The waves, present just after the stenosis increase in size by the middle of the cycle. By the end of the first cycle (t=1) the wave consists of a set of eddies occupying the channel downstream of the constriction and also just before the stenosis. As the flow is accelerated during the start of second cycle the eddies decay rapidly. Initially they remain in the same position and then vanish by the start of second cycle. As the second cycle proceeds the initial wave is swept downstream with the flow and decays, while a new wave is generated downstream of the constriction. Figure 3.13 shows the development of velocity profile along the length of the channel with time. The figure shows the velocity at three different locations along the length and at the centre along the width of the channel. It can be seen that velocity follows the inflow pattern before the stenosis and shows a fluctuation from the inflow velocity in the downstream region. This fluctuation could be because of the vortex waves generated in the downstream region.
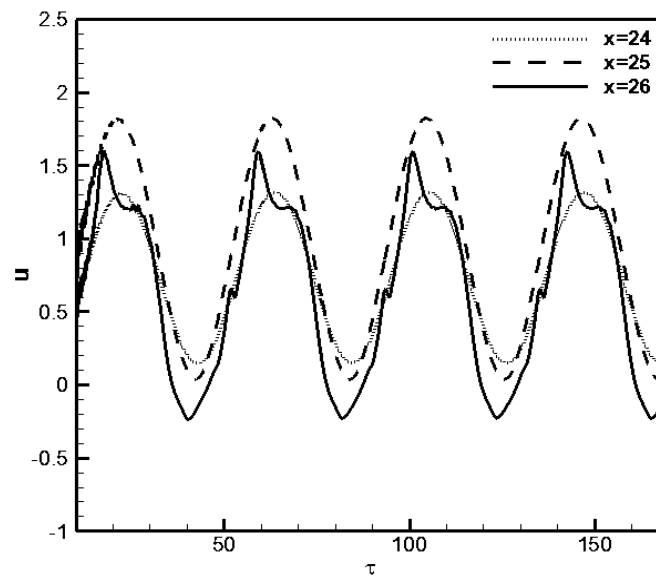
Figure 3.13 Centerline x-Velocity at three different x-locations along the length of the channel(Re=750, St=0.024)
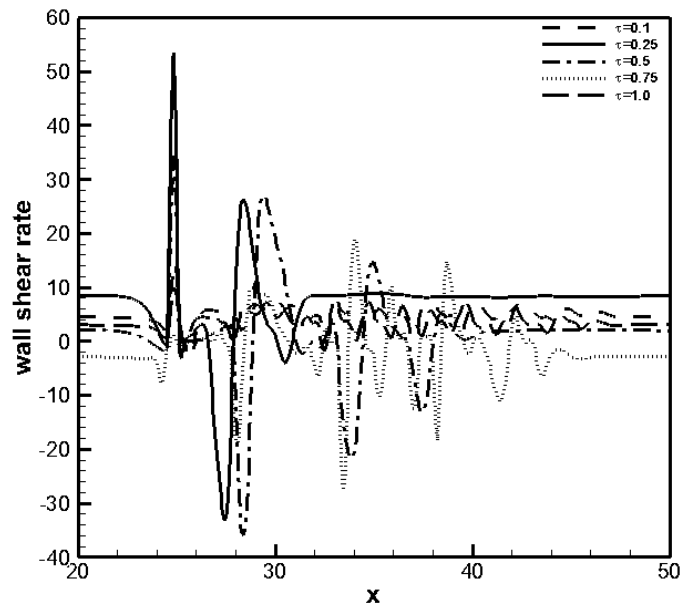
Figure 3.14 Upper Wall shear rate for Re=750 and St=0.024 at different time instants.
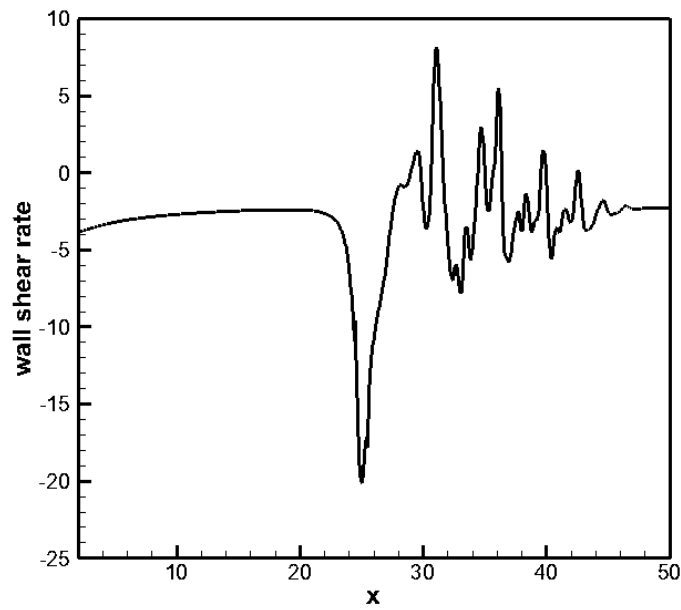
Figure 3.15 Time average upper wall shear rate for sinusoidal flow at Re=750, St=0.024

The non-dimensional shear rate on the upper wall is shown in Figure 3.14. As would be expected from the streamline patterns the wall shear distribution is complex. The extreme values are found where the channel width is least. Downstream of the constriction the values

48

are not as extreme but the peak values are still far greater in magnitude than the unsteady parallel flow. These peaks decrease in magnitude downstream with successive eddies, reflecting the gradual weakening of wave. Figure 3.15 shows the time average of the wall shear rate taken over a cycle. It shows that the peak values are reduced quite significantly on taking the mean. However the position of the peak value remains the same. Like the upper wall, similar scenario is observed on the lower wall too in Figure 3.16. However the peak values of wall shear rate are less compared to the upper wall.

The wall pressure distribution for this flow is shown in Figure 3.17. The fluctuations in the pressure is greatest near the constriction. Similar to uniform flow pressure drop is seen because of the stenosis. The pressure reaches a local minimum value (represented by the kink) at the peak stenosis and later recovers downstream. Also in the post stenotic region slight fluctuations in the pressure are seen. Figure 3.18 shows the mean of pressure distribution on the upper wall of the channel over a cycle. The sudden drop in the pressure could be observed at the peak stenotic region.


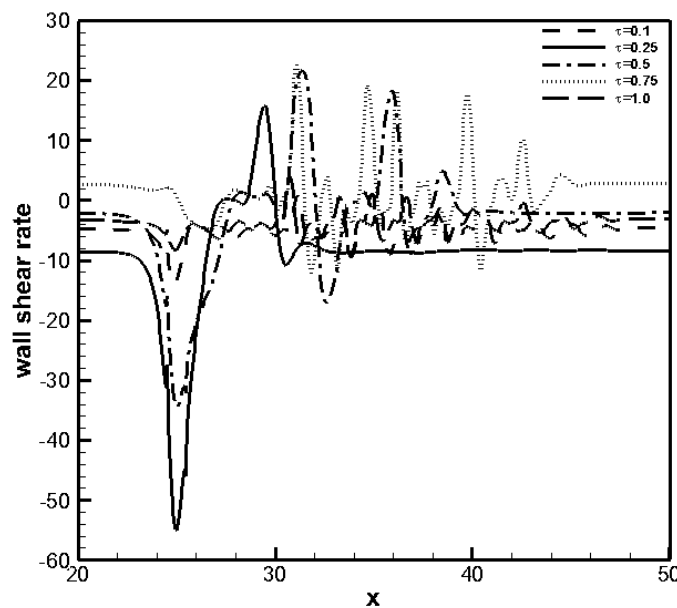Figure 3.16 Lower Wall shear rate for Re=750 and St=0.024 at different time instants.
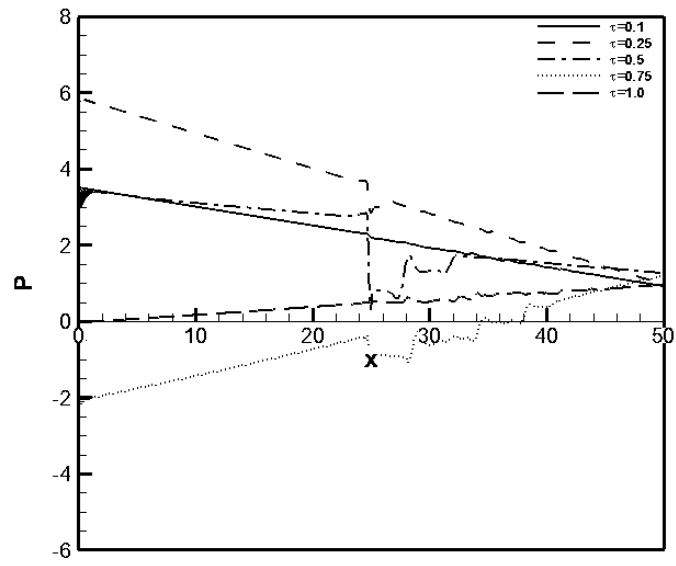
Figure 3.17 Wall pressure distribution for sinusoidal flow at Re=750 and St=0.024 at different time instants.
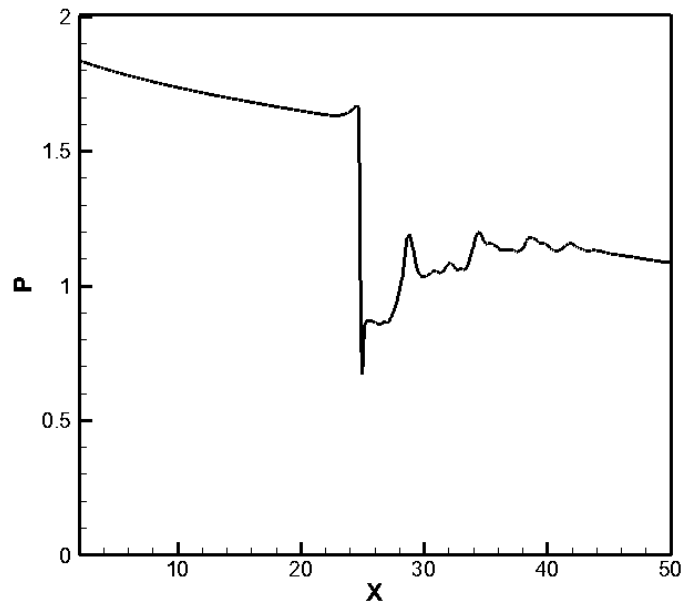
Figure 3.18 Time average wall pressure for sinusoidal flow at Re=750, St=0.024

3.2.1 Variation in Reynolds Number:

We have studied the effect of changing the Reynolds number of the flow by holding the geometry and Strouhal number constant, i.e. to change the strength of the wave but not to change the length of the wave. Figure 3.19 shows that the gradient in mean pressure decreases on decreasing the Re number. Also the sudden drop near the peak stenotic region is lower for lower Re. The vorticity and velocity vector plots for a flow with Re=500 and St=0.024 is shown in Figure 3.20. The waves exist like in case of Re=750, but spatially they decay in strength much faster with Re=500. Also at the same time instant less number of waves are present in comparison to the high Reynolds number flow. As would be expected the peak values of wall shear rate for Re=500 would be slightly less than those for Re 750 as shown in Figure 3.21 and Figure 3.22. Also the fluctuations in the wall shear rate in the post stenotic region is higher at higher Re. Again there is a significant reduction on the time average peak wall shear rate as shown in Figure 3.23. In Figure 3.24 pressure drop is seen along the length of the channel and a sudden drop in pressure is observed at the peak stenotic region.
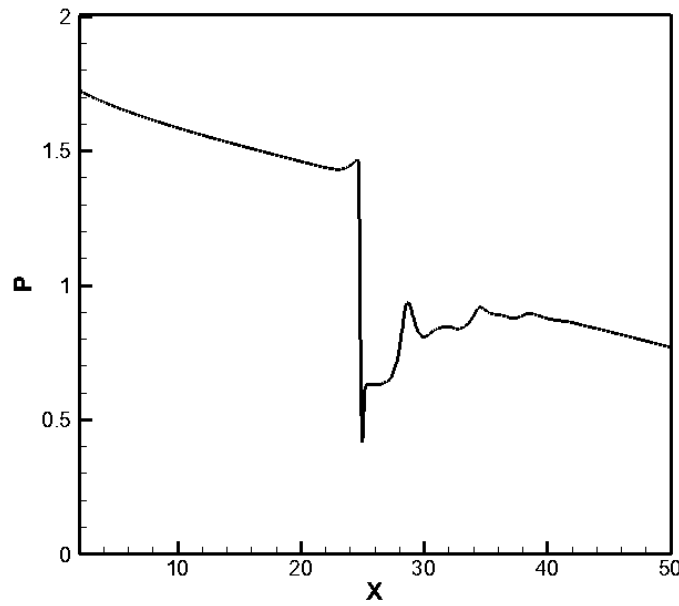
Figure 3.19 Time average wall pressure for sinusoidal flow at Re=500, St=0.024

Figure 3.20 Vorticity and velocity vector plots for sinusoidal flow(Newtonian) with Re=500

and St=0.024(x=22 to 32) at equal intervals in a cycle

Figure 3.21 Upper wall shear rate for sinusoidal flow with Re=500 and St=0.024

Figure 3.22 Lower wall shear rate for sinusoidal flow with Re=500 and St=0.024
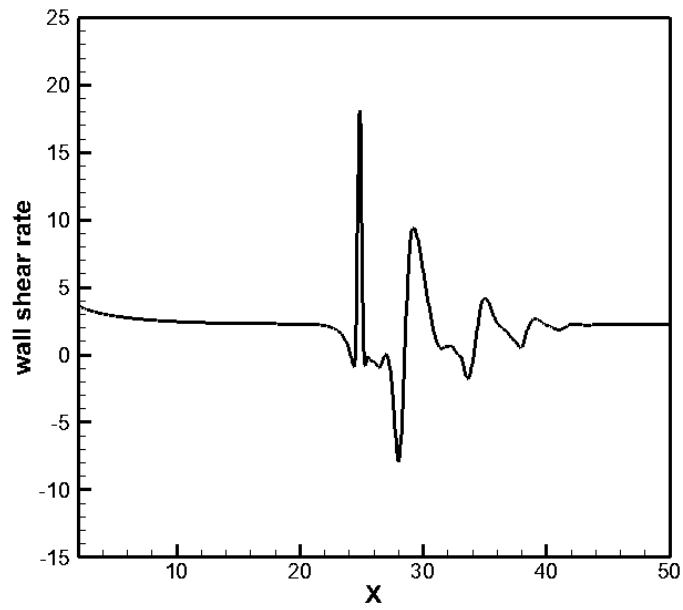
Figure 3.23 Time average upper wall shear rate for sinusoidal flow at Re=500, St=0.024
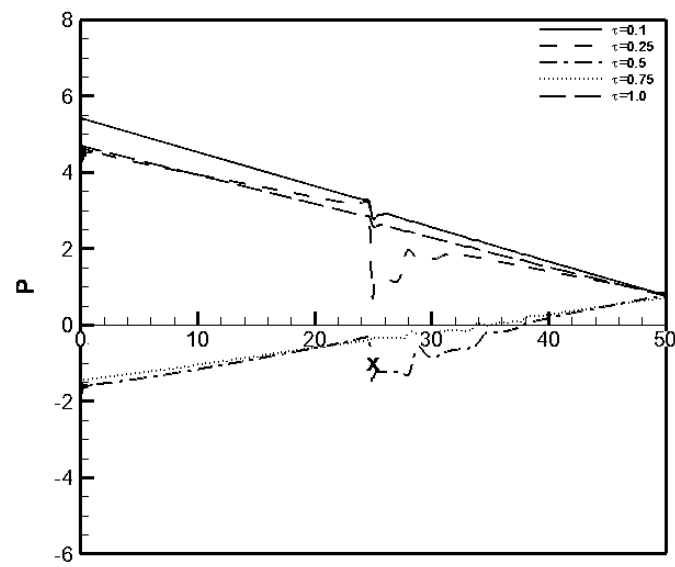
Figure 3.24 Wall pressure distribution for Re=500 and St=0.024 at different time instants.

3.2.2 Variation in Strouhal Number:

With an increase in Strouhal number, a shorter wave is expected and since the Reynolds number is fixed it would lead to a faster frequency of oscillation and hence a more vigorous wave is expected. These predictions can be seen in Figure 3.26 which shows the vorticity and velocity vector plots for Re=500 and St=0.048. The strength of the vortices for in case of higher St is higher for the same Re. Although the wavelength is shorter than that for lower Strouhal number, the peak values for shear stress is greater than those shown in Figure 3.21 for Re=500 and St=0.024 but the basic pattern is much the same. The centreline velocity pattern downstream of the stenosis also differs on changing the Strouhal number as can be seen in Figure 3.25. The peak values of wall shear rate shown in Figure 3.27 and Figure 3.28 are greater than those shown for Re=500, St=0.024, although the basic pattern is much the same.
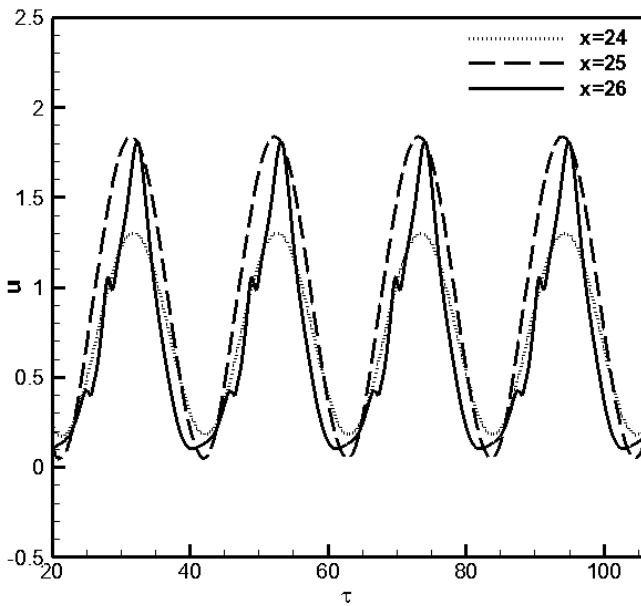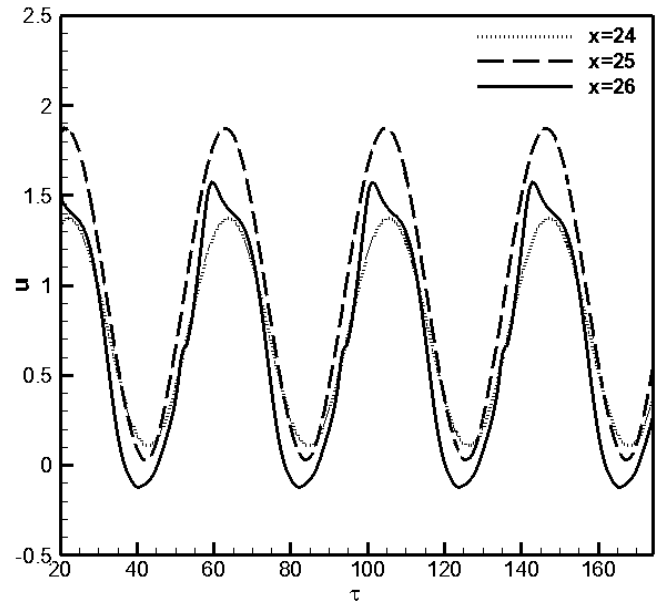
(a)   (b)

Figure 3.25 Centreline X-Velocity at three different locations along the length of the channel for Re=500 (a) St=0.048 (b) St=0.024
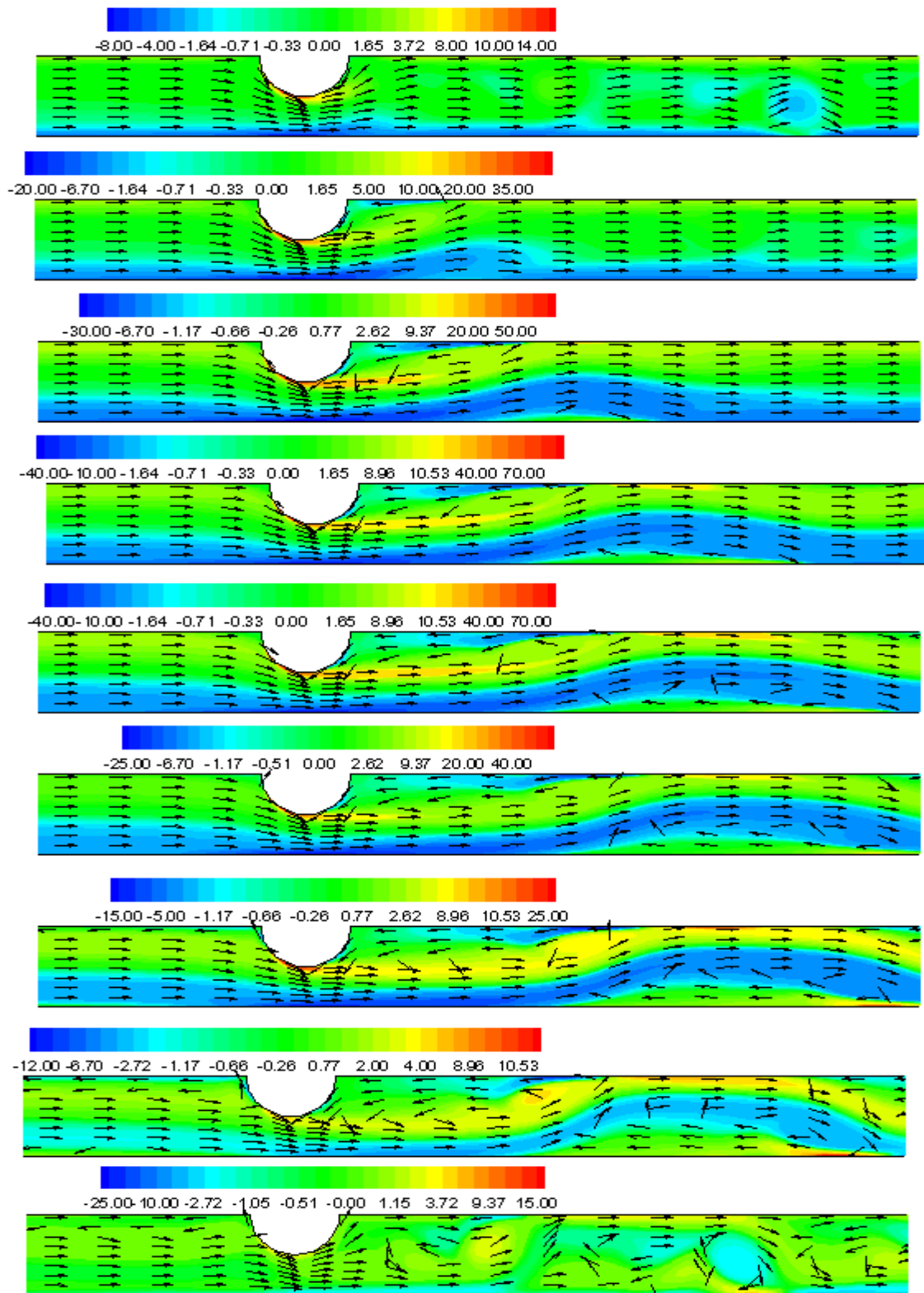
Figure 3.26 Vorticity and velocity vector plots for sinusoidal flow(Newtonian) with Re=500 and St=0.048(x=22 to 32) at equal intervals in a cycle

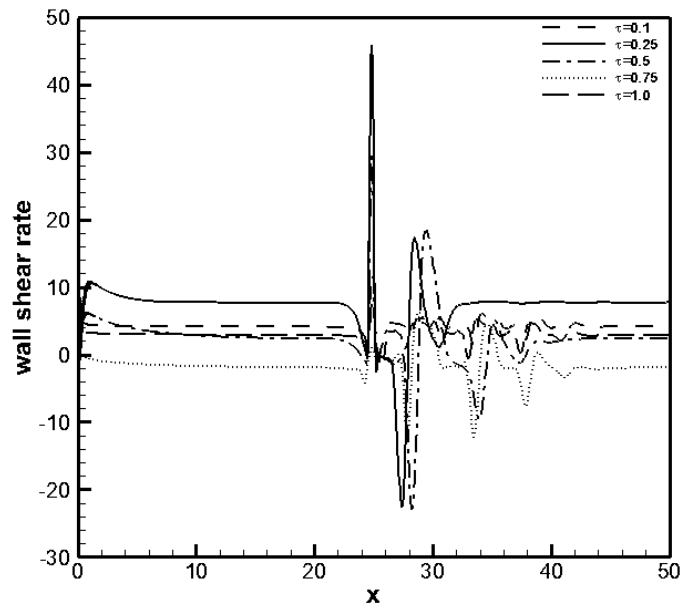Figure 3.27 Lower Wall shear rate for Re=500 and St=0.048 at different time instants
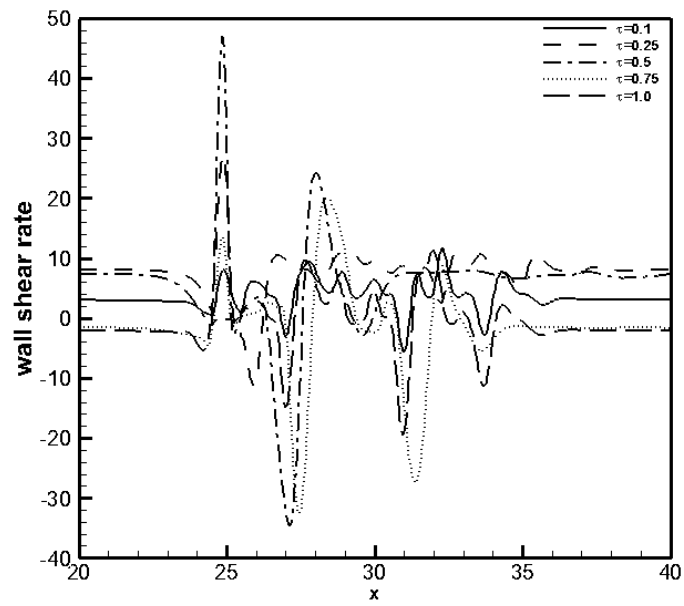
Figure 3.28 Upper Wall shear rate for Re=500 and St=0.048 at different time instants.

3.3 Non-sinusoidal inflow

The sinusoidal incoming flow which is used in theoretical and experimental studies of flow in non-uniform vessels [21] is not for the physiological case of flow in blood vessels where there is a double pulse, with the velocity during systole much greater than during diastole. Therefore to consider the effect of non-sinusoidal incoming flow, we use the velocity profile given in [16]

V=0.251+0.290($cos\phi + 0.97cos2\phi + 0.47cos3\phi + 0.14cos4\phi$)

Where $\phi = 2\pi\tau St - 1.4142$. This gives the velocity profile shown in Figure 3.29. Figure 3.30 shows the centreline X-velocity development with time along the channel at the three different locations. Similar to sinusoidal inflow, here too there is slight fluctuation in the velocity patterns after the stenosis but it follows the same pattern as of inflow velocity prior to that.

The flow is started from rest at t=0. The vorticity and velocity vector plots with time for Re=750 and Strouhal number= 0.024 are shown in Figure 3.31. However the number of vortex waves form in non-sinusoidal flow is more than in sinusoidal flow. Since the peak velocity of diastolic pulse is much less than the peak velocity of systolic pulse the vortex waves almost decay on the start of the cycle. But as half of the cycle is reached a number of vortex waves can be seen. These vortex decrease in size and decay by the end of the cycle.

The wall shear rate for this flow is shown in Figure 3.32 and Figure 3.33. The peak values are greater than those for the sinusoidal flow with the same Reynolds and Strouhal number (Figure 3.14) but the general pattern is as expected. During the second weaker part of the pulse the shear stress is relatively low throughout with the peak values at constriction. The wall pressure distribution is shown in Figure 3.34. This follows a similar pattern to the shear with relatively large changes during the main pulse and a weak response during the second part of the cycle. The strength of the vortex waves are higher in the initial phase of the cycle but less in the later phase in comparison to sinusoidal inflow velocity for the same Re and St.

The mean wall shear rate plot in Figure 3.35 shows close resemblance with the sinusoidal flow for same Re and St. However the time average pressure gradient is higher for non-sinusoidal flow as shown in Figure 3.36.
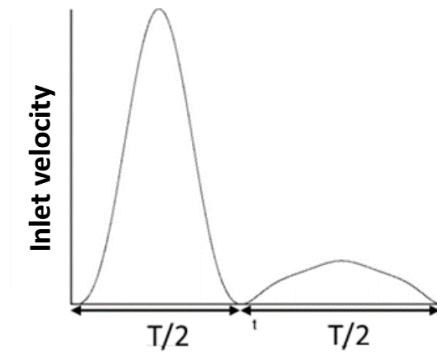
Figure 3.29 Non sinusoidal inflow velocity
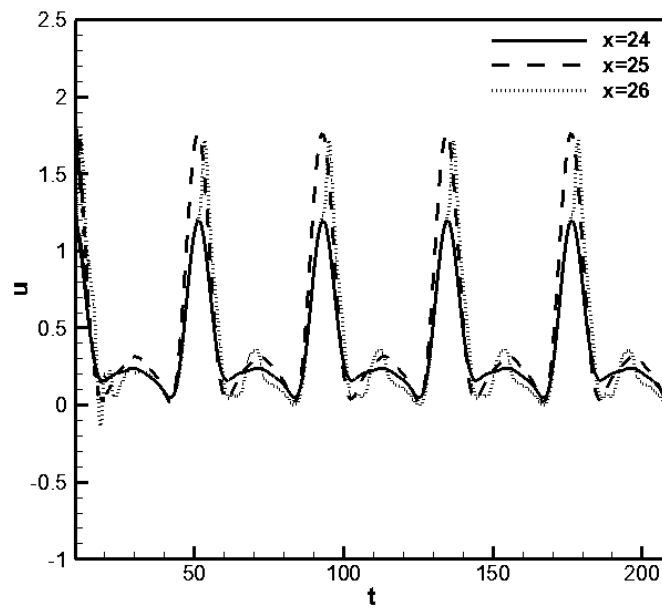
Figure 3.30 Centerline x-Velocity for non-sinusoidal inflow(Newtonian) at three different locations along the length of the channel(Re=750, St=0.024)
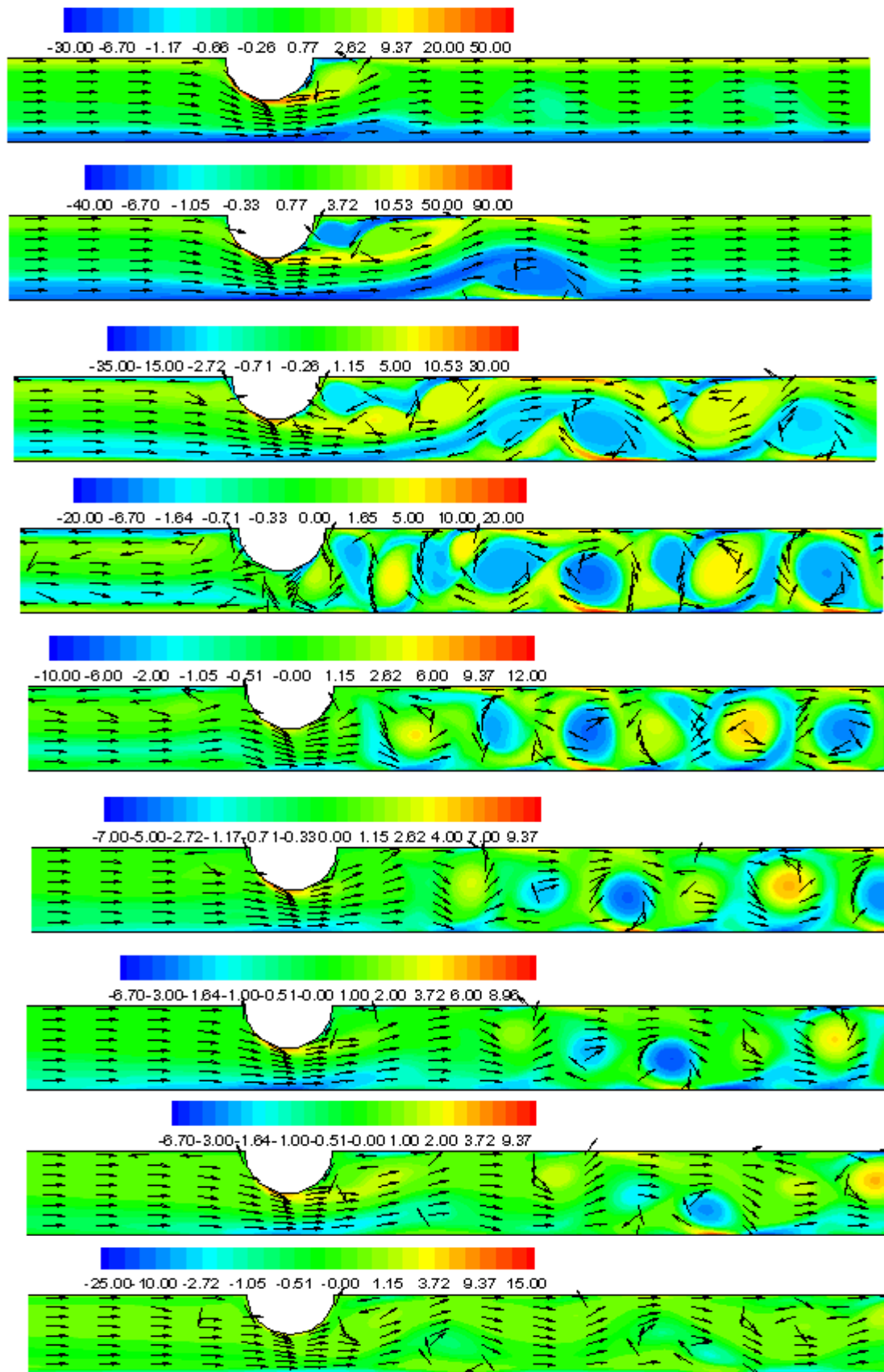
Figure 3.31 Vorticity and vector plots for non-sinusoidal flow with Re=750 and St=0.024(x=22 to 32) at equal intervals in a cycle
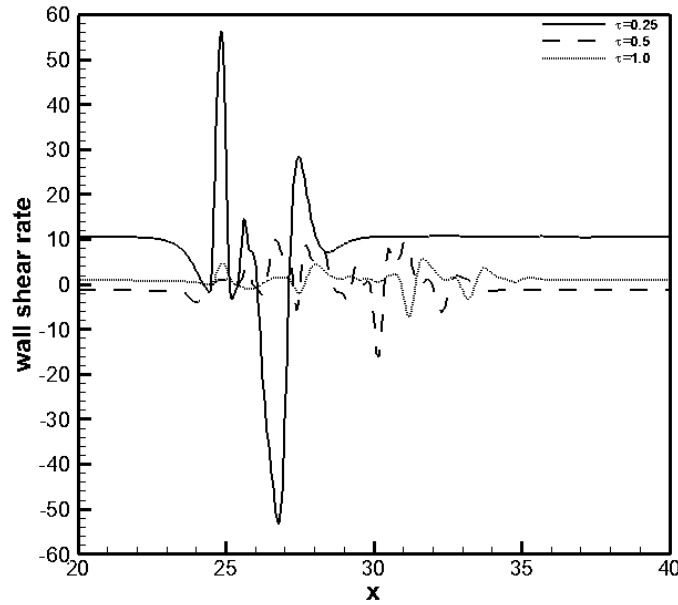
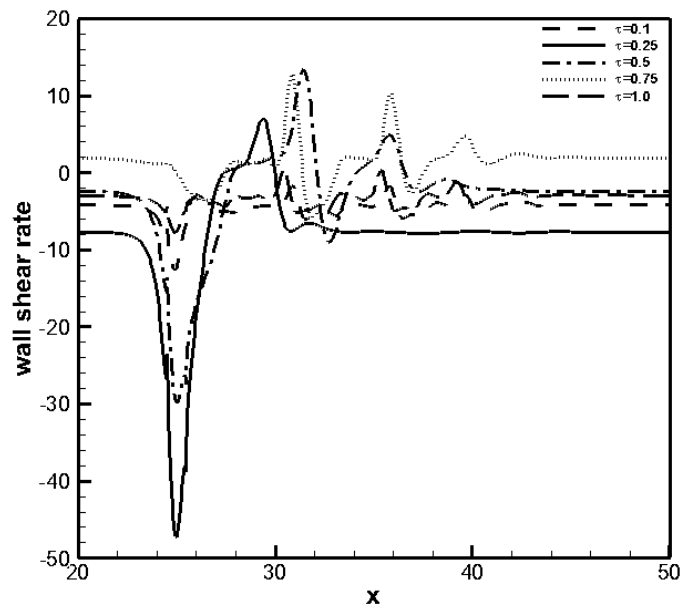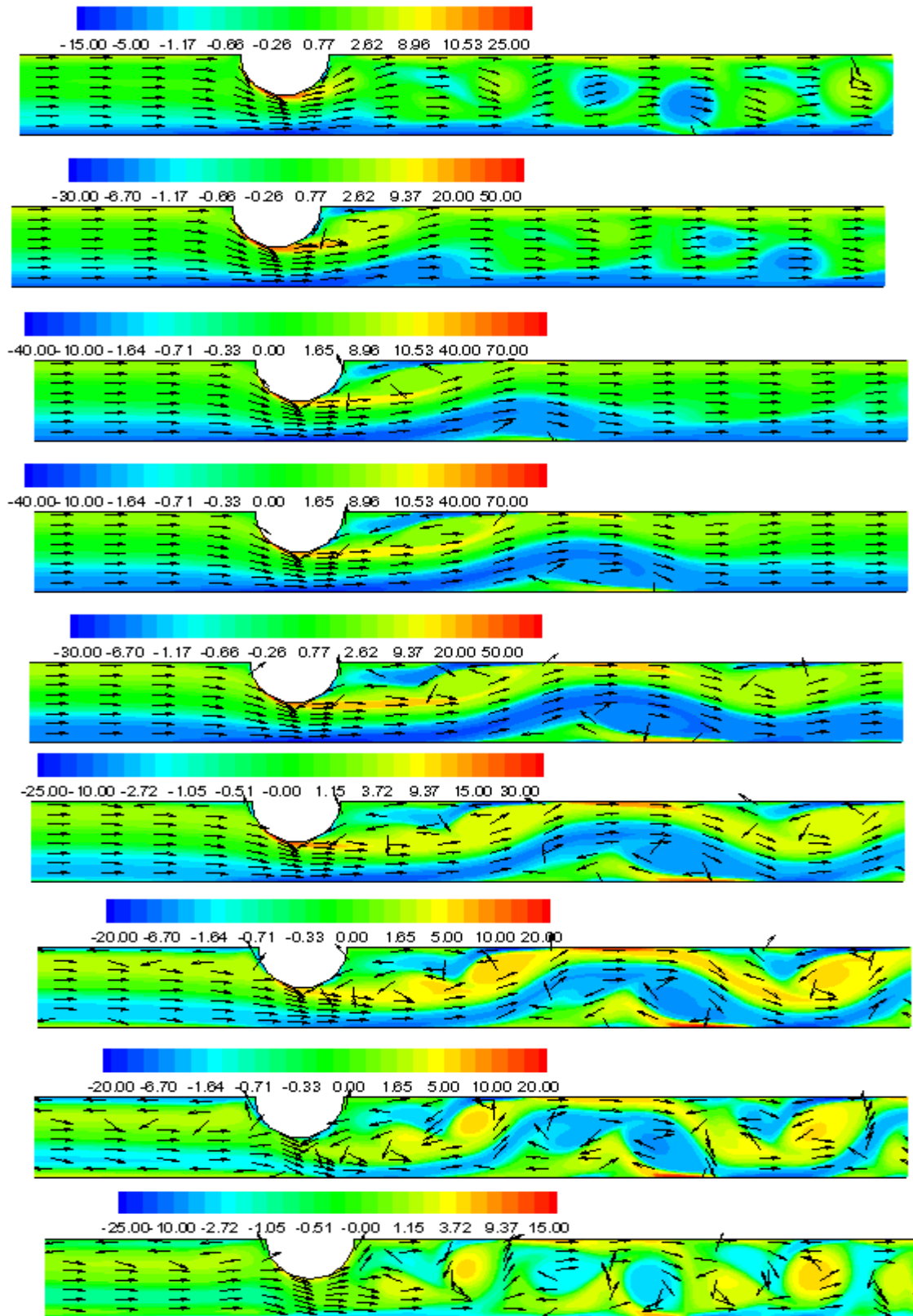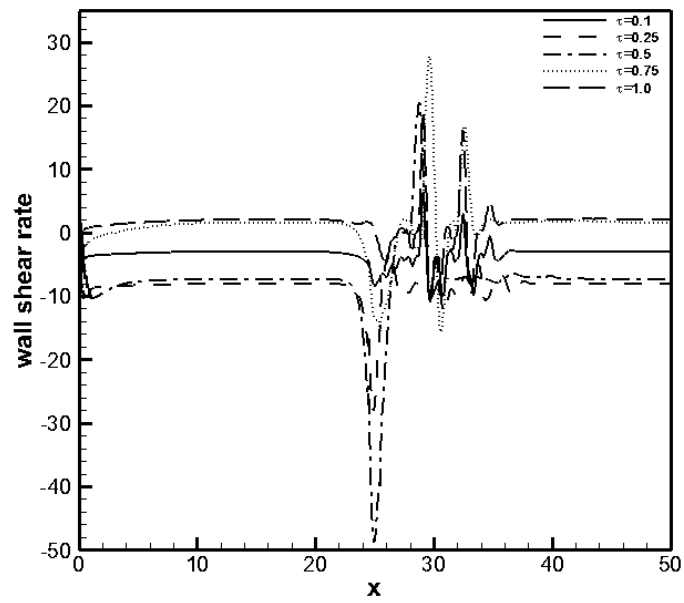Figure 3.32 Upper wall shear rate for non-sinusoidal flow with Re 750 and St=0.024 for different time instants.

We have characterized our problem in terms of the basic fluid mechanical parameters, the Reynolds and Strouhal numbers, whereas physiological flows are commonly characterized by the Womersley number. For a non-uniform vessel with nonparallel flow, two flows with the same Womersley number may have very different behaviour. For example, in our problem, if we increase the flow velocity but hold the other parameters constant, Re would increase, St would decrease, but α would not change. However, we would have a longer vortex wave with a larger wavelength and a corresponding change in the wall shear stress and pressure distributions, although the strength of the wave (in terms of the eddy strength and the magnitude of the peak values of wall shear stress) may not change much as the effect of increasing the Reynolds number would be compensated for by the effect of decreasing the Strouhal number.
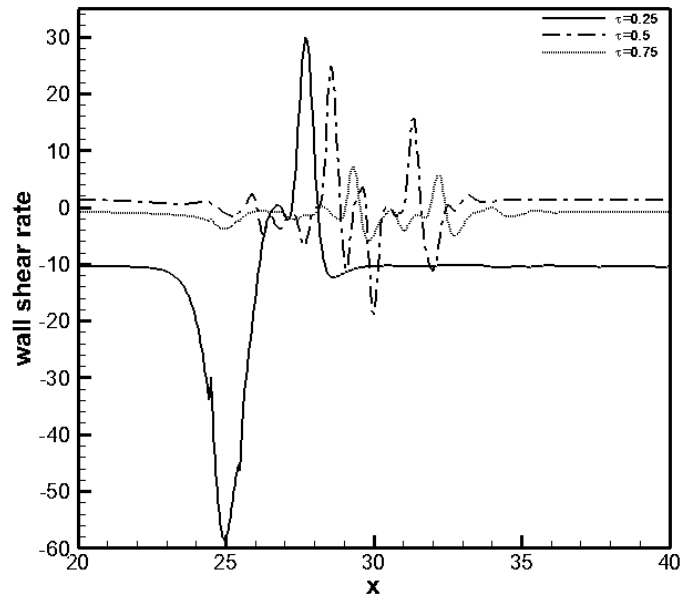
Figure 3.33 Lower wall shear rate for non-sinusoidal flow with Re 750 and St=0.024 for different time instants.
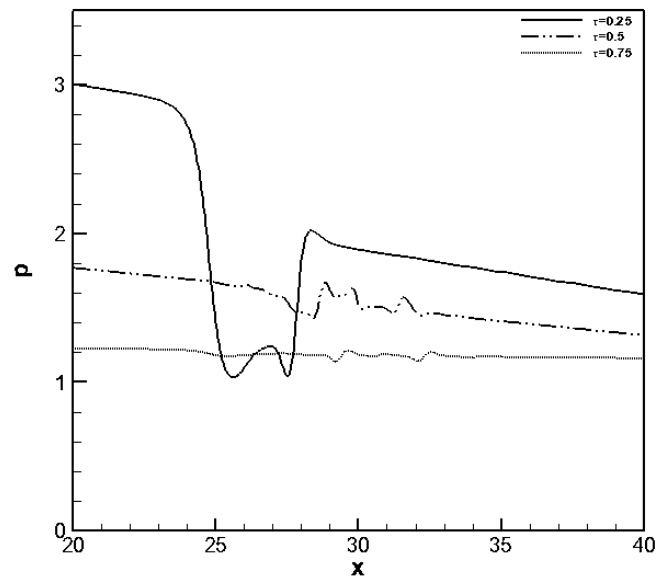
Figure 3.34 Upper wall pressure distribution for nonsinusoidal flow with Re =750 and St=0.024 for different time instants
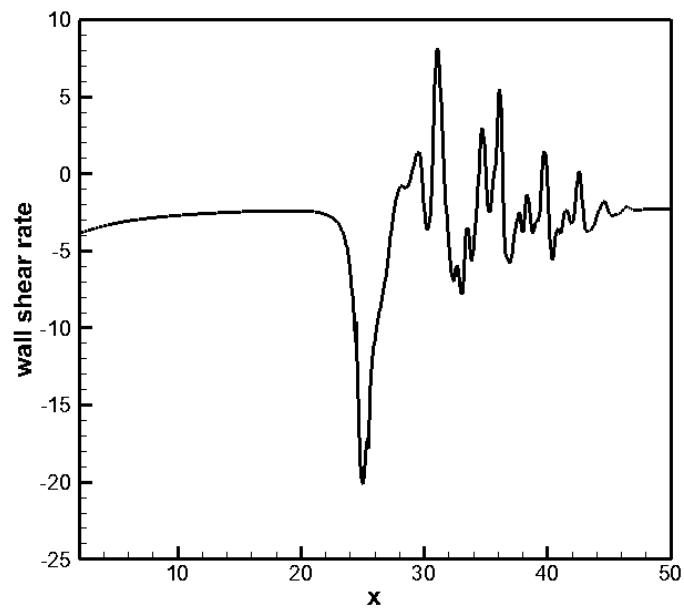
Figure 3.35 Time average upper wall shear rate for non-sinusoidal flow at Re=750, St=0.024
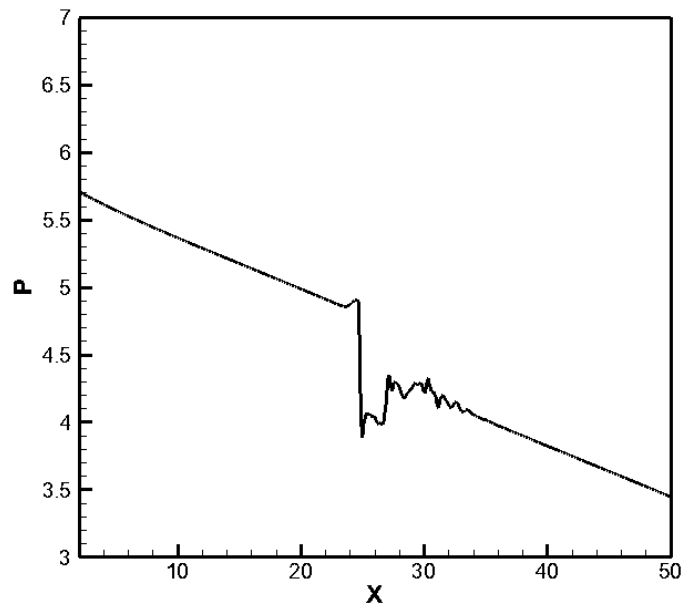
Figure 3.36 Time average wall pressure for non-sinusoidal flow at Re=750, St=0.024

3.4 Comparison with Non-Newtonian Flows

It is consider that blood is a non-Newtonian fluid because the elastic and deformable structure of red cell give is a shear dependent viscosity. Therefore to consider the non-Newtonian behaviour of blood a brief study of the Generalized Newtonian model of blood has been done. The unsteady flow of blood governed by oscillatory velocity profile is studied. The key hemodynamic variable affecting the growth of atherosclerotic plaques is the wall shear rate. We therefore have examined the difference brought about by shear-thinning behaviour on the peak wall shear rate in both uniform and pulsatile flows. The difference in the vorticity and velocity vectors plots and pressure variation is also studied.

3.4.1 Sinusoidal inflow

Figure 3.37 shows the vorticity and velocity vectors for the shear thinning fluid at different time instants. The flow pattern is the almost same in both the fluids. However, the vorticity formation is less in shear-thinning model than the Newtonian model of blood. A primary vortex is formed during the initial phase of the cycle which increases in size as half of the cycle is reached. As the end of the cycle is reached few more vortex waves are generated which decay as the next cycles begins. Less recirculation zones are present in non-Newtonian flow as compared to Newtonian flow. Very less vortex waves are seen which decay rapidly as the cycle ends. Figure 3.38 and Figure 3.45 shows the time history of the velocity development along the channel length for sinusoidal and non-sinusoidal inflow. Here it can be seen the velocity follows the same inflow pattern unlike the case with Newtonian flows as in Figure 3.13 and Figure 3.30 where the velocity pattern slightly fluctuates after the stenosis. The variation of peak wall shear stress at different time instants is shown in Figure 3.39 and Figure 3.40. The conclusion from the graphs is that for a pulsatile velocity and for a given Re, the shear thinning fluid will experience a higher peak shear rate than the Newtonian fluid. Also the fluctuations in the shear rate decay quite rapidly in comparison to the Newtonian flows. Also it can be seen that in non-Newtonian flows much lesser eddies are formed for the same Re in comparison to Newtonian flows. Similarly a pressure gradient is seen in Figure 3.41 as compared to Newtonian. A high pressure gradient is attained as compared to Newtonian flows. However the variations in pressure in post-stenotic region is less as compared to Newtonian flow.
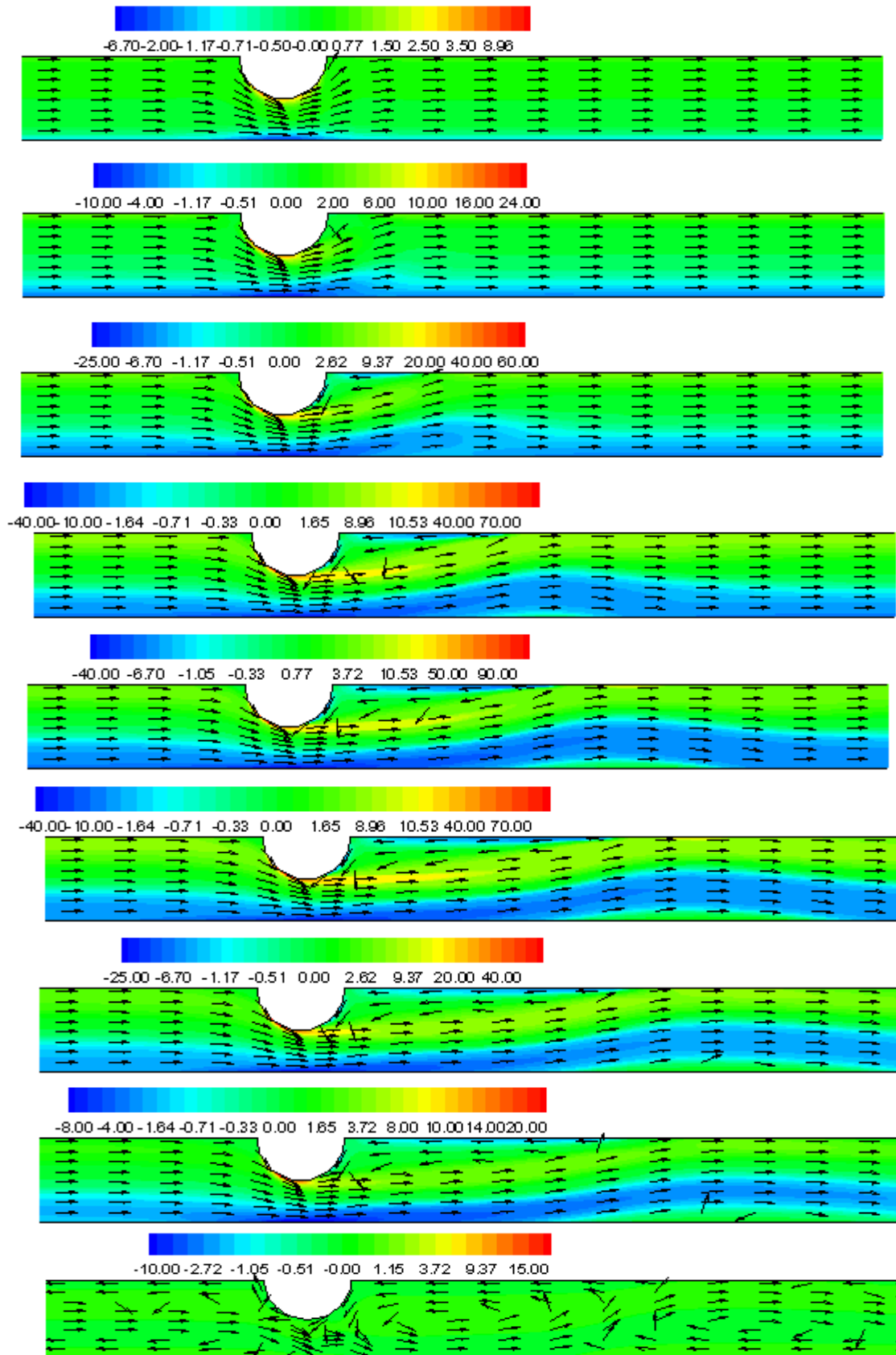
Figure 3.37 Vorticity and velocity vector plots for non-newtonian sinusoidal flow with Re=750 and St=0.024(x=22 to 32) at equal intervals in a cycle
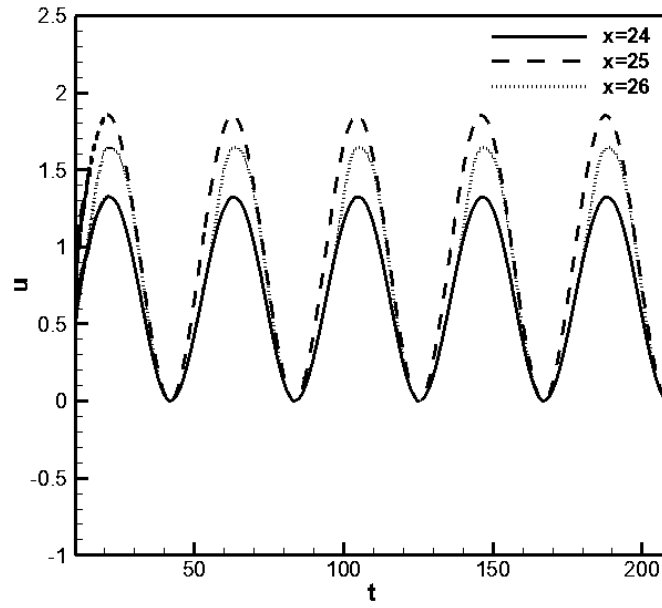
Figure 3.38 Centerline x-Velocity at three different locations along the length of the channel(Re=750, St=0.024)
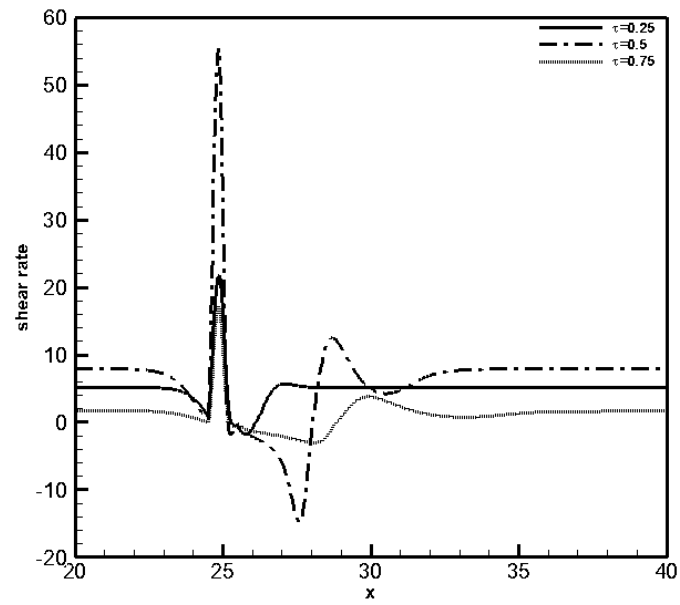
Figure 3.39 Upper wall shear rate for non-Newtonian sinusoidal flow with Re 750 and St=0.024 for different time instants.
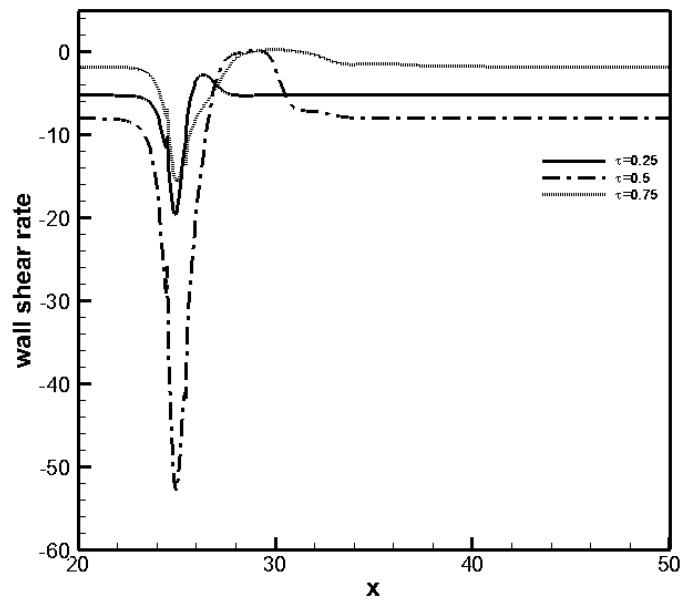
Figure 3.40 Lower wall shear rate for non Newtonian sinusoidal flow with Re 750 and St=0.024 for different time instants.
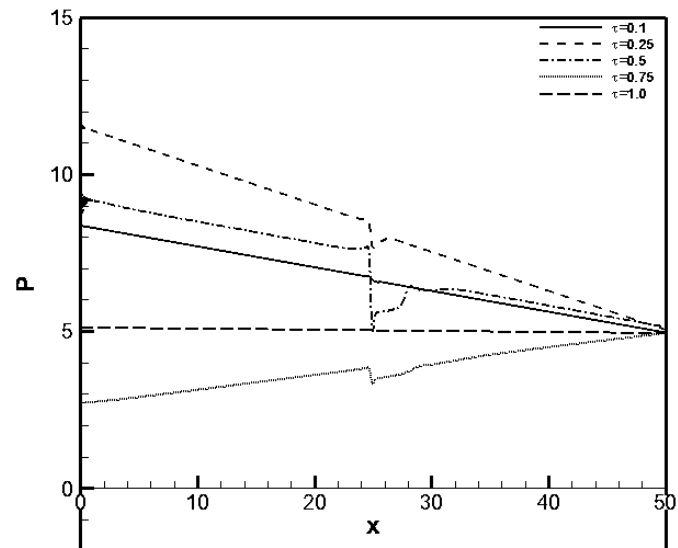

Figure 3.41 Wall pressure distribution for non Newtonian sinusoidal flow with Re 750 and St=0.024 for different time instants.

Figure 3.42 shows the time average wall shear rate for non-Newtonian flows and it can be seen that the peak value is higher for non-Newtonian fluid. The mean pressure gradient pattern in Figure 3.43 is similar to that obtained for Newtonian flows.
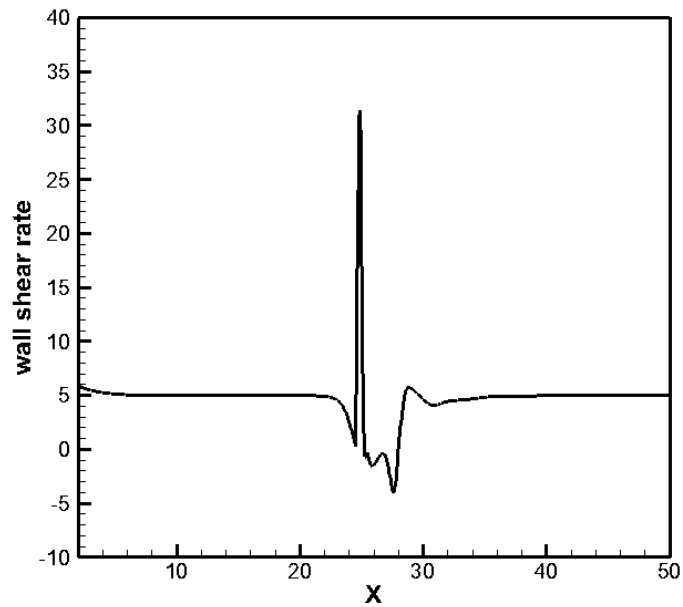
Figure 3.42 Time average upper wall shear rate for non-Newtonian sinusoidal flow at Re=750, St=0.024
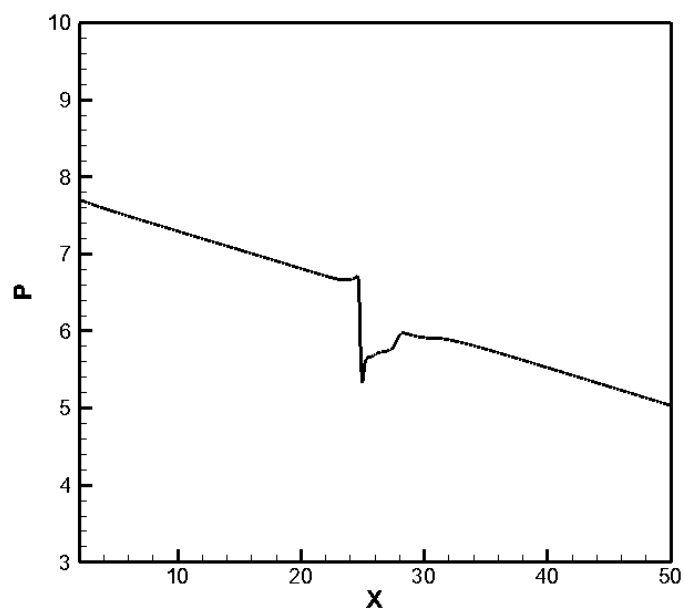
Figure 3.43 Time average wall pressure distribution for non-Newtonian sinusoidal flow at Re=750, St=0.024

3.4.2 Non-Sinusoidal flow
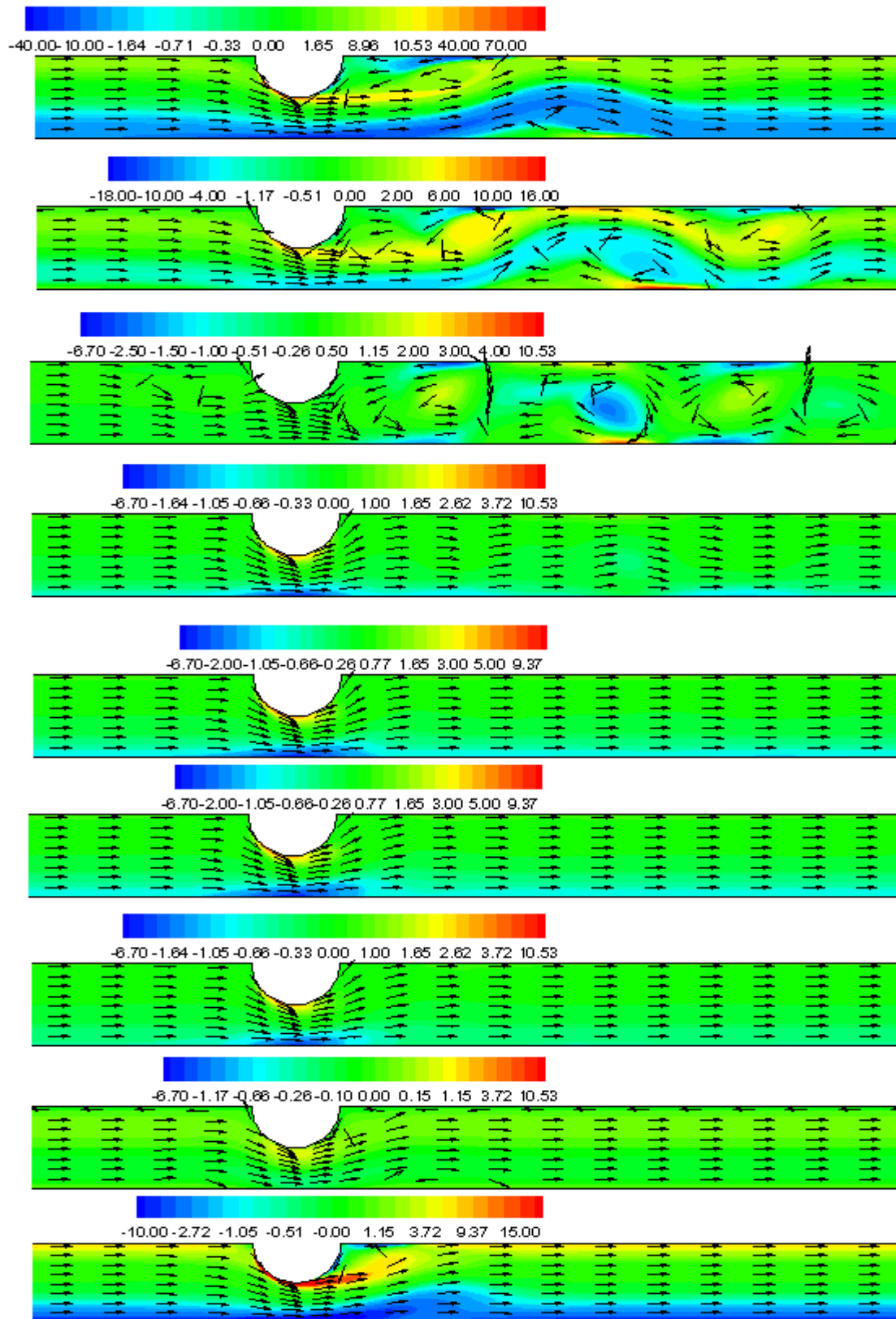
Figure 3.44 Vorticity and velocity vector plots for non-sinusoidal flow(non-Newtonian) with Re=750 and St=0.024(x=22 to 32) at equal intervals in a cycle
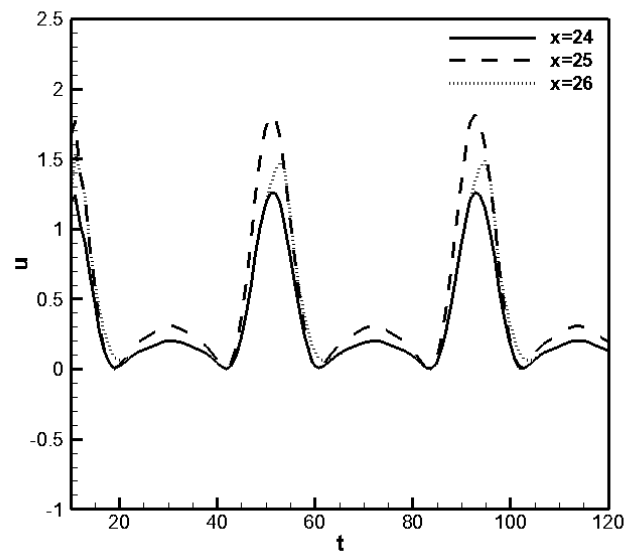
Figure 3.45 Centerline x-Velocity at three different locations along the length of the channel(Re=750, St=0.024)
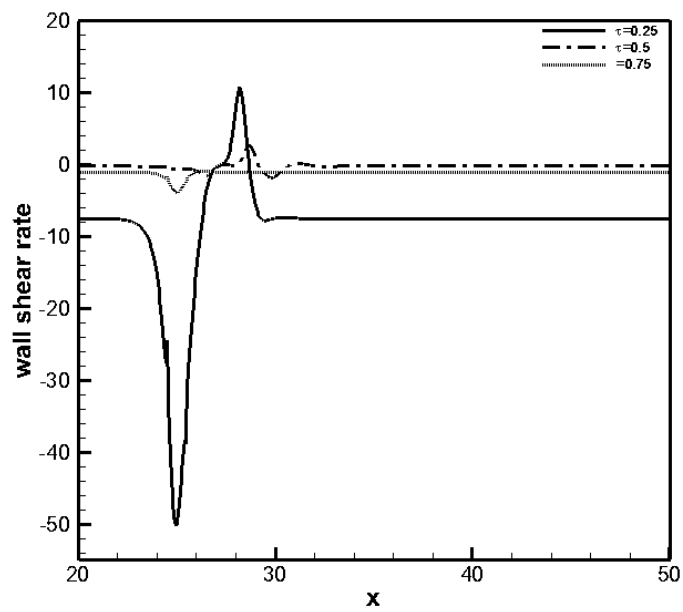
Figure 3.46 Lower wall shear rate for non Newtonian non-sinusoidal flow with Re 750 and St=0.024 for different time instants.

Figure 3.44 shows the vorticity and velocity vectors for non-sinusoidal inflow velocity in Non-Newtonian flow. The velocity profiles are similar to the Newtonian case with the same inflow velocity but the flow is not as complex. Here again eddies are formed by the end of the first phase of the cycle in comparison to Newtonian flows which decay quite rapidly by the end of the cycle.The peak values of vorticity are higher than Newtonian flows. Figure 3.46 and Figure 3.47 show the lower and upper wall shear rates for the non- sinusoidal flow at different time instants. Similar to sinusoidal flows the peak values of shear rate are less at different time instants in comparison to Newtonian flows. The shear rate attain a steady value quickly downstream of the stenosis unlike Newtonian flows where large fluctuations are seen. The fluctuations in the wall pressure downstream of stenosis is also very less as seen in Figure 3.48.
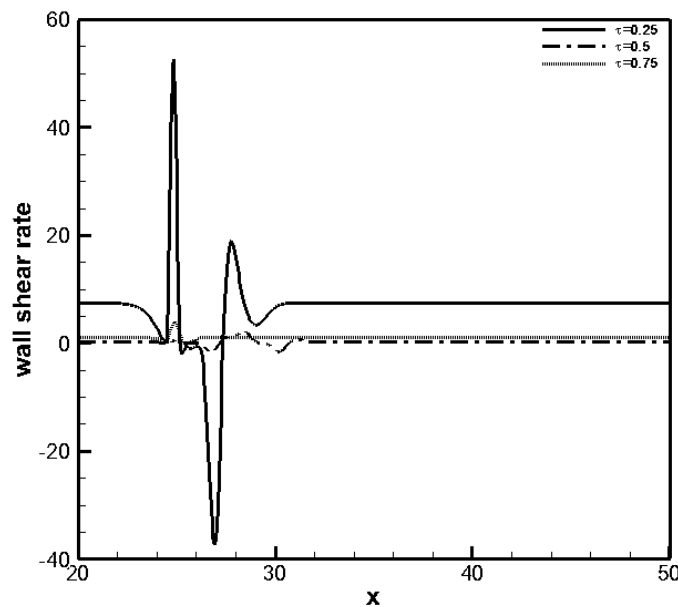
Figure 3.47 Upper wall shear rate for non-Newtonian non-sinusoidal flow with Re 750 and St=0.024 for different time instants.
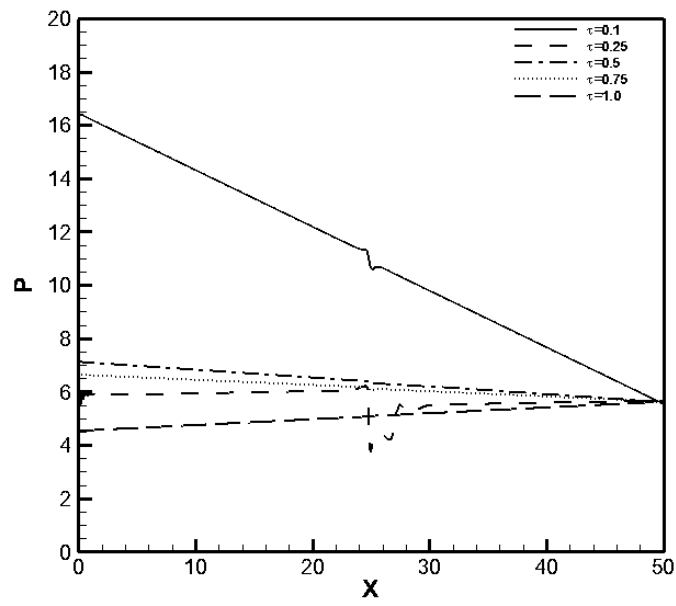
Figure 3.48 Wall pressure distribution for non Newtonian non-sinusoidal flow with Re 750 and St=0.024 for different time instants.
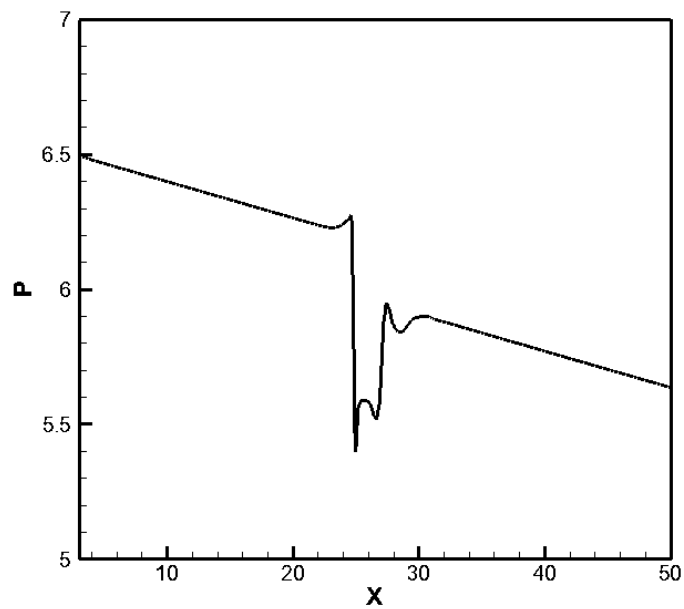
Figure 3.49 Time average wall pressure distribution for non Newtonian non-sinusoidal flow at Re 750 and St=0.024

Chapter 4 POD Analysis

Proper orthogonal decomposition (POD) is a powerful statistical tool for the extraction of significant patterns or structures in large data set. In the context of fluid mechanics, the data comprises of flow field information obtained from a number of experiments (physical or numerical) or the information of an unsteady flow field at different time instants from a single experiment. Most of the earlier efforts involving the application of POD to fluid flow problems have been directed at investigating the dynamics of the different classes of turbulent flows. Very few studies have focussed on the application of POD for the investigation of laminar unsteady flows. To the author's knowledge, the POD has not been utilized to investigate blood flow in constricted channels. The POD has established itself as a powerful reduction tool with the capability of representing a data ensemble with the smallest set of modes for a given accuracy.

In the light of the purpose described above, the POD analysis has been carried out on the computational data at different combinations of Re and St for Newtonian and non-Newtonian flow. This chapter is organised in two sections. The mathematical elements of the POD and the method of snapshots is presented in § 4.1. § 4.2 presents the POD analysis.

4.1 Mathematical elements of POD

Proper orthogonal Decomposition or Karhunen-Loeve expansion is a statistical technique that has been known for quite some time but has gained popularity in the subject of fluid mechanics over the last decade. The technique provides an optimal spatial basis for capturing the spatial structure of the most energetic fluctuations in the flow field in an average sense. Let $U^m = U(x, \tau_m)$, m=1,.....M be M realizations or snapshots of the fluctuating flow field obtained through experimentation or numerical simulations. In the present case, the snapshots U^m comprises of both the fluctuating velocity components and the fluctuating vorticity field with the three values $(U_1, U_2, U_3) \equiv (u', v', \omega')$. This is done in order to take care of the inherent coupling of the velocity and vorticity field for the problem under consideration. The K-L basis functions are thus vector functions Ψ with three components at each point (Ψ_1, Ψ_2, Ψ_3) associated with the two velocity components and the vorticity field. The vector space in which the decomposition is sought has an inner product defines as:

$$(f, g) = \int_D (f_1 g_1 + f_2 g_2 + f_3 g_3) dA \qquad (4.1)$$

As pointed out by Lumley and Poje [24], the introduction of a scaling factor 's' is necessary to balance the velocity and vorticity fluctuation energies so that the K-L basis captures the structure of the most energetic structures of both the vorticity and the velocity fields in a composite manner. They have shown that the proper value of s that maximizes the average of the square of the projection of the data onto the basis function ψ is given as:

$$s = \frac{\int_D \langle (u'u' + v'v') \rangle dA}{\int_D \langle \omega' \omega' \rangle \, dA}$$

(4.2)

The '$\langle \rangle$'denotes the ensemble average and in the present scenario is taken to be the time average as a result of time stationarity of the flow field. The K-L basis function ψ is given by the Fredholm Integral of the first kind given as:

$$\int_\Omega R_{ij}(x, x') \Psi_j(x') \, dA = \lambda \psi_i(x), \quad (i,j) \epsilon \{1,3\}$$

(4.3)

The Kernel of the integral in equation (4.3) is the two point Correlation tensor defined as:

$$R_{ij}(x, x') = \langle U_i(x, \tau) U_j(x', \tau) \rangle$$

Equation (4.3) is an eigenvalue problem with λ as the eigenvalue and $\psi \equiv (\psi_1, \psi_2, \psi_3)$ as the Eigen function or mode. It is known that the eigenvalue problem expressed via equation (4.3) has countably infinite non-negative eigenvalues and corresponding eigenfunctions. The eigenfunctions $\{\Psi\}_1^\infty$ or modes are orthogonal and form a complete basis of an infinite-dimensional linear space spanned by them. These basis functions can be normalized to yield:

$$\left(\psi^{(p)}, \psi^{(r)} \right) = \delta_{pr}$$

The superscripts in parentheses represent the POD quantum numbers. The K-L basis is utilized for carrying out the decomposition of the fluctuating flowfield as:

$$U(x, \tau) = \sum_1^\infty a^{(p)}(\tau) \, \psi^{(p)}(x)$$

(4.4)

Once the eigenfunctions are known, the temporal coefficients in equation (4.4) can be readily obtained as:

$$a^p(\tau) = \left(U, \psi^{(p)}\right)$$

It can be shown that the temporal coefficients are uncorrelated and satisfy the relation:

$$\langle a^{(p)} a^{(r)} \rangle = \delta_{pr} \lambda^{(p)}$$

The total energy captured by the expansion in the average sense is given as:

$$E = \langle (U, U) \rangle = \sum_p \sum_r \langle a^{(p)} a^{(r)} \rangle \left(\psi^{(p)}, \psi^{(r)} \right) = \sum \lambda^{(p)}$$

(4.6)

If the eigenvalues $\{\lambda\}_1^\infty$ are ordered such that $\lambda^{(1)} > \lambda^{(2)} > \lambda^{(3)}$ ...., the sequence on the right of equation (4.4) converges more rapidly than with any other basis and only a few modes are needed to obtain a good enough reconstruction of the original data ensemble U^i.

The discrete solution of the eigenvalue problem in equation (4.3) involves handling a fairly large algebraic eigenvalue problem in terms of the values of the eigenfunctions at the discrete mesh points. For the mesh points employed in the present study, the order of the algebraic problem is equal to three times the total number of mesh points in the domain. To overcome this difficulty, Sirovich [25], proposed the method of snapshots. In this method the eigenfunction ψ is taken as a linear combination of the snapshots given as:

$$\psi = \sum_1^M \alpha_m U^m$$

(4.7)

Furthur expressing the two point Correlation tensor as:

$$R_{ij}(x, x') = \frac{1}{M} \sum_1^M U_i^m(x) U_j^m(x')$$

(4.8)

Utilizing equation (4.7) and (4.8), the eigenvalue problem in equation (4.3) is transformed into an equivalent, M eigenvalue problem given as,

$$A\alpha = \lambda\alpha$$

(4.9)

where $\qquad A_{mn} = \frac{1}{M}(U^m, U^n)$

Since relatively few snapshots are needed to capture the temporal structure of non-turbulent flows, the method of snapshots is preferred in most cases. This method yield at most M modes.

4.2 POD Analysis

The method of snapshots has been applied to obtain the POD eigen spectra and the eigenfunctions or modes for the different cases of Re and St for the Newtonian and non-Newtonian flows. The POD modes are also employed to reconstruct the instantaneous flow field.

4.2.1 Eigen spectra and eigenfunctions

For the flow problem 512 snapshots equally spaced in time over one period have been taken for the determination of the modes or eigenfunctions. Since the decomposition is applied to the fluctuating flow field, the mean for each set of snapshots is computed and subtracted from the instantaneous snapshots to obtain the snapshots for the fluctuating flow field. For each of the cases, the number of snaps appropriate for the determination of the eigenfunctions is obtained through a series of trials with increasing number of snaps. The number of snaps adequate for the decomposition is determined by carrying out a snapshot independence study, in which the leading eigenvalues do not change significantly with increase in the number of snapshots employed. A typical outcome of the snapshot independence study is shown in Table 4.1 for the case of Re=750, St=0.024. It can be observed that the leading ten eigenvalues do not change significantly for 128 snaps or more. The fraction of energy captured for the first N modes is given as,

$$\frac{E_N}{E} = \frac{\sum_1^N \lambda^{(p)}}{\sum_1^M \lambda^{(P)}}$$

(4.10)

It is observed from the data in Table 4.1 that, the first fifteen eigenvalues taken together represent more than 99% average energy of the entire data ensemble and the remaining eigenvalues or modes are not significant. Similar snapshot independence studies have been carried out for other cases to determine the appropriate number of snaps for carrying out the decomposition. For the given flow problem for the various combinations of Re and St and for Re in case of uniform inflow velocity pattern a data ensemble comprising of 128 snaps or more is found to yield converged leading eigenvalues. However the number of modes capturing 99% energy in the data ensemble is greater for flows with Re 750 than for Re 500. Also the value is more for Newtonian model than the non-Newtonian model.

Table 4.1: Convergence of eigenvalues with increase in number of snaps

Mode (p)	Snaps=32	Snaps=64	Snaps=128	Snaps=256	Snaps=512
1	12.317	12.320	12.321	12.321	12.321
2	2.585	2.585	2.586	2.586	2.586
3	0.767	0.766	0.767	0.767	0.767
4	0.343	0.343	0.343	0.343	0.343
5	0.265	0.264	0.265	0.265	0.265
6	0.168	0.167	0.167	0.167	0.167
7	0.106	0.107	0.107	0.107	0.107
8	0.087	0.085	0.084	0.084	0.084
9	0.079	0.075	0.075	0.075	0.075
10	0.068	0.068	0.067	0.067	0.067

For uniform inflow velocity pattern and Newtonian flow 132 modes capture more than 99% energy for Re=750 whereas only 3 modes capture the same energy for Re=500. For uniform inflow velocity pattern and non-Newtonian flow 1 mode capture more than 99% energy for Re=750 and for Re=500.

For sinusoidal Newtonian flow, 8 modes capture more than 99% energy for Re=500 and 15 modes are required for Re=750 irrespective of their Strouhal number. For the non-Newtonian case 4 modes capture 99% of the energy for Re=750 and St=0.024, 3 modes for Re=500 and St=0.048 and 2 modes for Re=500 and St=0.024.

Figure 4.1(a)-Figure 4.1(d) shows the eigenvalue spectra for the different cases of uniform inflow velocity.

Figure 4.2(a) - Figure 4.2(d) shows the eigenvalue spectra for the different cases of Newtonian flows. The fast convergence of POD modes can be readily observed as a small number of modes are needed to capture almost 99% energy of the snapshots in the average sense. It is interesting to observe the spatial structure of the eigenfunctions or modes associated with the few leading eigenvalues for these cases.
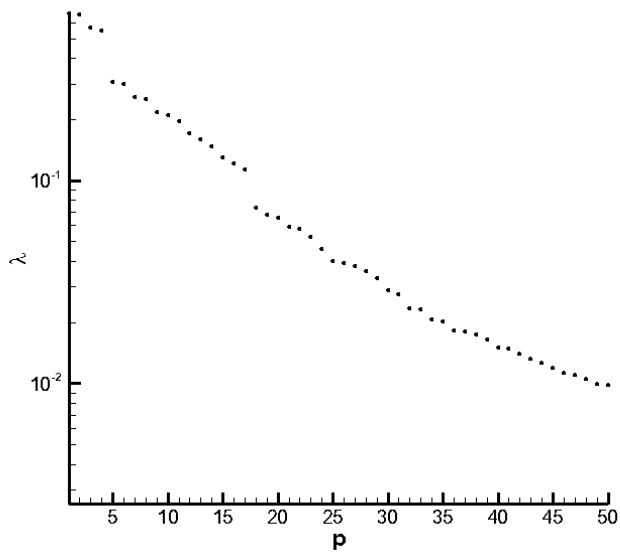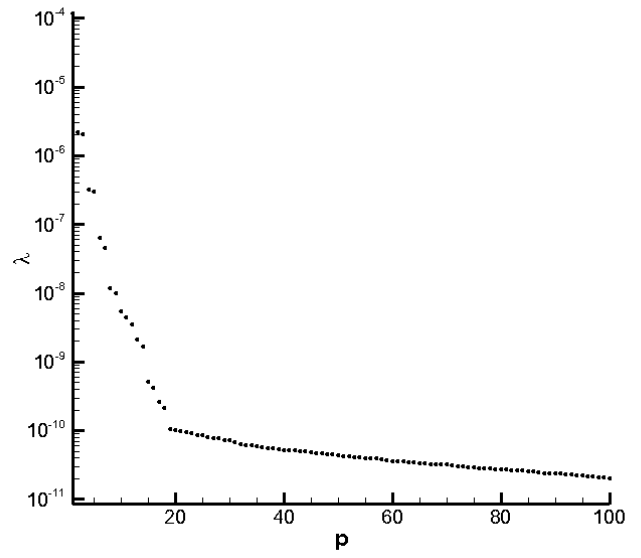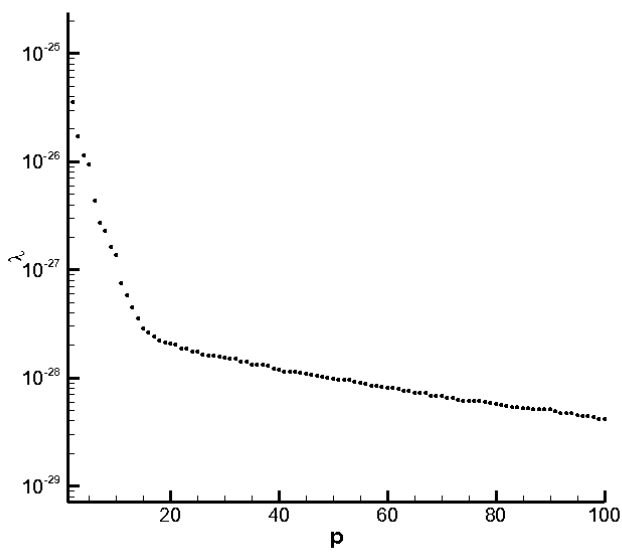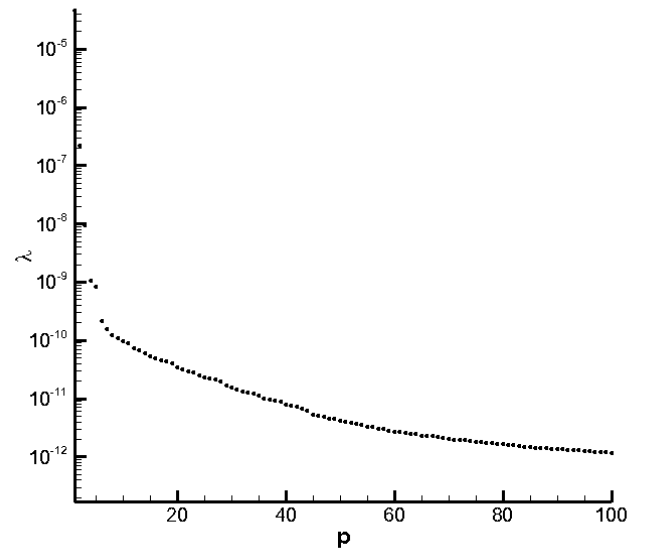
Figure 4.1 Eigen value spectra for uniform inflow velocity (a) Newtonian flow Re=750 b) Newtonian flow Re=500 c) Non-Newtonian flow Re=750 d) Non-Newtonian flow Re=500
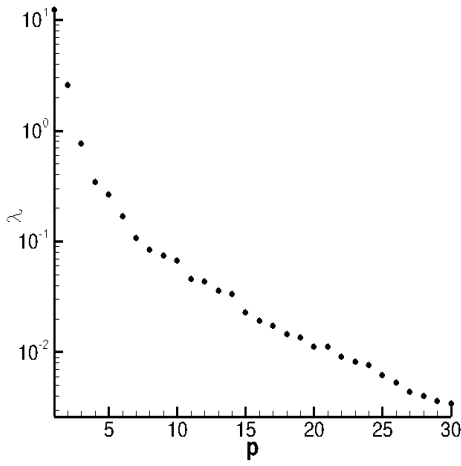
(a)
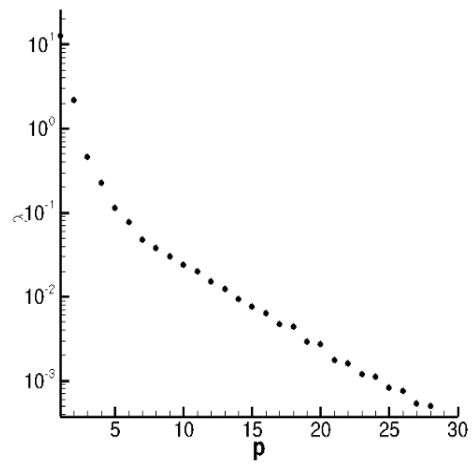
(b)
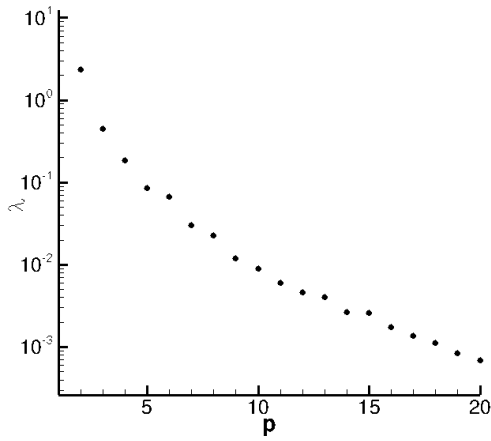
(c)
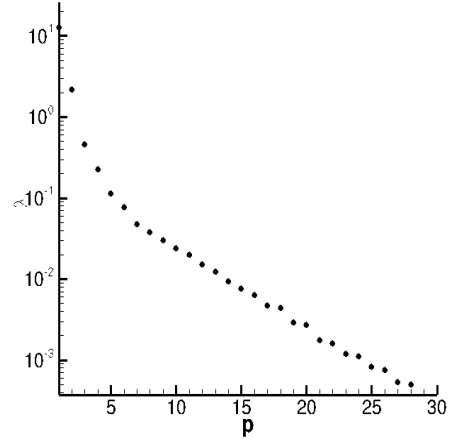
(d)

Figure 4.2 Eigen value spectra for Newtonian flow. a) Re=750, St=0.024 b) Re=750, St=0.048 c) Re=500, St=0.024 d) Re=500, St=0.048

The eigenvalues for velocities $\psi_1^{(p)}$ and $\psi_2^{(p)}$ for a particular mode have been combined to yield the spatial structure of the fluctuating velocity field captured by the mode. This is possible as the individual components of the vector eigenfunction for a given mode are multiplied by the same scalar temporal coefficient. Thus the directional sense of the structure of the fluctuating

velocity field captured by the mode is effectively visualized through a streamline plot of vector function $\psi_v^{(p)} = \left(\psi_1^{(p)}, \psi_2^{(p)}\right)$. Figure 4.3(a)-Figure 4.3(d) shows the eigenspectra for the various cases of non-Newtonian flows.
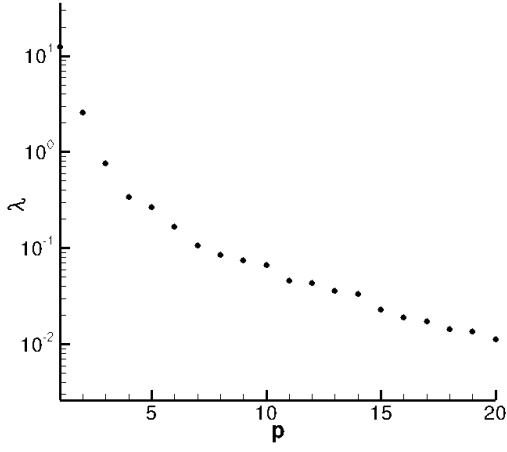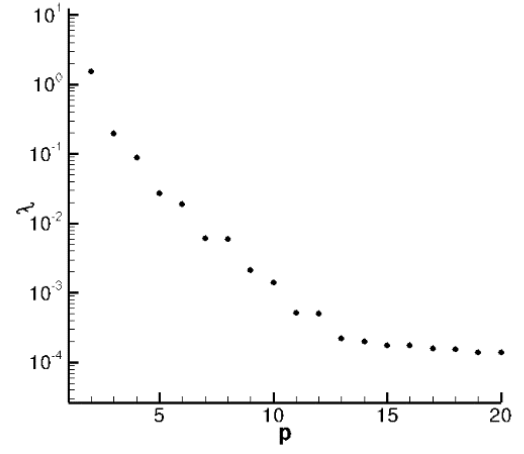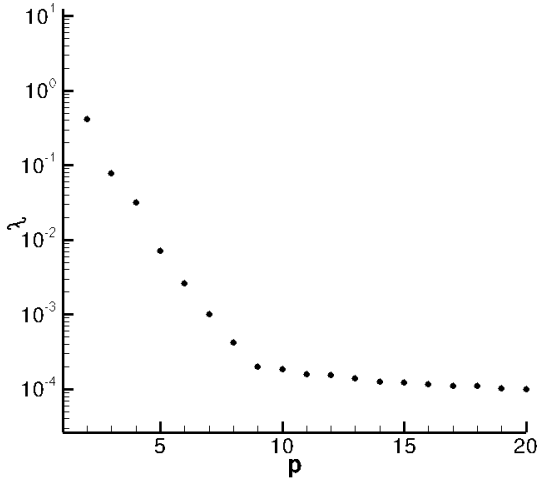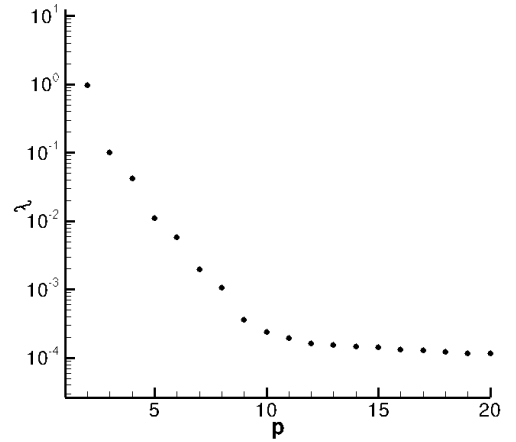
Figure 4.3 Eigen value spectra for Non-Newtonian flow. a) Re=750, St=0.024 b) Re=750, St=0.048 c) Re=500, St=0.024 d) Re=500, St=0.048

4.2.2 Flow field reconstruction

The POD modes or the eigenfunctions can be used to reconstruct the original data ensemble or flow field snaps by using equations (4.4) and (4.5). The reconstruction of the flow field from equation (4.4) requires the truncation of the infinite summation sequence. Thus the reconstructed flow field $V^N(x, \tau)$ obtained from the first N modes can be expressed as,

$$V^N(x, \tau) = \sum_1^N a^{(p)}(\tau)\psi^{(p)}(x)$$

(4.11)

The number of modes N obtained in the infinite expansion of equation (4.4) determines the accuracy of the reconstruction. As given in equation (4.10), a simple criteria based on the fraction of the total average energy has been commonly employed in most of the earlier works. In this regard the criteria proposed by Deane and Sirovich [33] has been widely used. According to this criteria, the number of modes which capture more than 90% of the average energy in the ensemble U^i along with the condition that none of the neglected modes has more than 1% of energy of the most energetic mode, should be retained for accurate reconstruction. However, this criteria has some drawbacks as proposed by Nadeem and Sanghi [34]. To overcome the drawback, a different method was proposed by them for specifying the limit for the truncation of infinite expansion given in equation (4.4), which is used for the flow field reconstruction in the present scenario. The truncation criteria are specifically designed to reflect directly on the accuracy of the reconstruction of the data using the POD modes.

Let V^N be the reconstructed flow field as given by equation (4.12). The temporal coefficients required for the evaluation of the expansion in equation (4.12) are obtained using equation (4.5). The error norms,E_j^N, j=1, 2 or 3, representing the accuracy of the spatial structure obtained via reconstruction using the POD modes are defined as:

$$E_j^N = \left(\frac{\int_\Omega (U_j - V_j^N)^2 \, dA}{\int_\Omega U_j^2 \, dA} \right)^{1/2} , \text{j=1,2 or 3}$$

(4.12)

The three error norms (E_1^N, E_2^N, E_3^N) provide information on the space averaged rms error in the reconstruction of the fluctuating velocity components and vorticity field of a given snapshot separately using the first N modes. This is a quantitative measure that reflects directly on the accuracy of the reconstruction. These error norms are evaluated for the data ensemble

comprising of M snapshots for a fixed number of POD modes (N). The maximum values of these error norms ($E_{1\,max}^{N}, E_{2\,max}^{N}, E_{3\,max}^{N}$) over the entire data ensemble for a given number of modes are taken as a quantitative measure of accuracy with which the data ensemble can be represented with the given number of modes. By computing these maximum values for increasing values of N, information regarding the increase in accuracy of reconstruction for an increase in number of modes can be assessed. By specifying on these error norms, the number of modes that will provide a reconstruction within a specified level of accuracy over the entire time interval of the data ensemble can be determined.

In the context of the above discussed criteria, Table 4.2 , Table 4.3 and Table 4.4 show the results of exercise carried out to obtain the number of POD modes or dimensions needed for accurate representation of the data for uniform inflow velocity ,pulsatile inflow for Newtonian and Non-Newtonian flow repectively considering different Re and St. The values of the error norms for the velocity components and the vorticity fields are the maximum values for the entire data ensemble for each Re and St. As expected the error decreases rapidly with increase in the number of modes. The comparison between the maximum values of the three error norms, the fraction of average energy captured by a given number of POD modes (N), is also shown in Table 4.2, Table 4.3, and Table 4.4. The fact that the velocity and vorticity fields converge at different rates is also shown in Table 4.2,Table 4.3 and Table 4.4. Consider the reconstruction of the flow field at Re=500 and St=0.048 using 10 modes in Table 4.3. The values of the error norms are 13.34%, 43.91% and 19.70%. From the point of view of energy criterion, 10 modes capture 99.39% energy. Thus while there are significant deviations in terms of error norms, the energy criteria gives a false sense of accuracy as already mentioned by Nadeem and Sanghi [34]. Further, a single lumped criteria is not sensitive to the difference in the convergence rates of the velocity and vorticity fields. For lower Re less number of modes are required to reconstruct the flow field. Similarly for non-Newtonian flows lesser number of modes are required.

From Table 4.2 for uniform inflow at Re=750, it can be seen that 40 modes capture only 92.48% of the total energy and the error norms too indicate that reconstructions of the fluctuating flow field using 40 modes yields significant maximum rms deviations of 28.68%, 26.40% and 38.45% in the velocity components and vorticity field respectively.

Table 4.2: Convergence statistics of POD based reconstructions of the computational data for uniform inflow Newtonian and non-Newtonian flow

Type of flow	Re	N	$E_{1\,max}^{N}$	$E_{2\,max}^{N}$	$E_{3\,max}^{N}$	$\sum_{1}^{N} \lambda^{(p)}/\sum \lambda$
Newtonian flow	750	20	0.53908	0.43669	0.57830	0.825160
		40	0.28680	0.26403	0.38456	0.924848
	500	1	0.99974	1.00008	0.99970	0. 958939
		2	0.93846	0.99236	0.96831	0. 976734
		4	0.40549	0.61119	0.42373	0. 996322
		6	0.20923	0.35801	0.22402	0. 999255
		8	0.11425	0.26073	0.12197	0. 999730
		10	0.09292	0.06597	0.08138	0. 999855
		12	0.04897	0.04869	0.04745	0. 999919
Non-Newtonian flow	750	2	0.00799	0.55254	0.00171	1.0
		4	0.00799	0.53274	0.00178	1.0
		5	0.00893	0.65770	0.00199	1.0
		6	0.00426	0.63464	0.00124	1.0
	500	3	0.06379	0.19096	0.06927	0. 999922
		6	0. 02201	0.07492	0.02463	0. 999967

For Newtonian flow at Re=750, St=0.024, 20 modes capture 99.45% of the total energy while the error norms indicate that reconstructions of the fluctuating flow field using 20 modes yields significant maximum rms deviations of 13.43%, 44.17% and 20.82% in the velocity components and vorticity field respectively as shown in Table 4.3. Thus as mentioned by Nadeem and Sanghi [34], the energy criterion can be misleading as far as accuracy of the reconstruction of the data ensemble is concerned. A similar observation is made for all other cases. The convergence of the POD expansion is much slower for the Newtonian flows than for non-Newtonian flows. 40 modes are needed for accurate reconstruction (to bring the error norms within 5% or less) in case of Newtonian flows whereas 10 modes are sufficient for non-Newtonian flows for Re=750 and St=0.024. Also the rate of convergence decreases with increase in Re and St, though the influence of Re is more. For all the cases, the maximum rms deviations are brought close to 5% or less by the number of modes that capture greater than 99.98% of the average energy of the snaps in the average sense. Thus to achieve an accurate reconstruction of the flow under consideration a 99.98% energy criteria appears suitable here. However, since the energy criteria may vary from problem to problem and is hard to predict beforehand, the criteria based on error norms allows one to achieve any desired level of accuracy in POD reconstructions.

Table 4.3: Convergence statistics of POD based reconstructions of the computational data for sinusoidal inflow Newtonian flow

Re	St	N	$E_{1\ max}^{N}$	$E_{2\ max}^{N}$	$E_{3\ max}^{N}$	$\sum_{1}^{N} \lambda^{(p)} / \sum \lambda$
500	0.024	1	1.00868	1.00893	1.00304	0.798956
		5	0.18113	0.62237	0.25216	0.989466
		10	0.09836	0.45265	0.15725	0.998187
		15	0.05461	0.22980	0.08335	0.999416
		20	0.02270	0.09450	0.04072	0.999772
		25	0.00908	0.04975	0.02199	0.999879
750	0.024	1	1.00906	1.06291	1.00341	0.719133
		5	0.31598	0.94658	0.47204	0.950330
		10	0.28696	0.70407	0.37682	0.979514
		15	0.22064	0.55346	0.29771	0.990109
		20	0.13434	0.44172	0.20820	0. 994512
		25	0.06864	0.26414	0.13566	0.996972
		30	0.05355	0.20266	0.10619	0.998181
		35	0.03631	0.14487	0.07570	0.998874
		40	0.02325	0.10082	0.05641	0.999267
		50	0.01578	0.06131	0.03910	0.999655
500	0.048	1	1.03808	1.04038	1.01129	0.795180
		5	0.26253	0.70751	0.33402	0.980472
		10	0.13343	0.43914	0.19708	0.993943
		15	0.04505	0.22963	0.10190	0.997953
		20	0.02456	0.12371	0.06548	0.999255
		25	0.01460	0.07046	0.04136	0.999660
		30	0.00705	0.03452	0.02227	0.999811
750	0.048	1	1.03992	1.04728	1.01096	0.747702
		5	0.39343	0.76657	0.46109	0.956966
		10	0.23055	0.49336	0.32927	0.982096
		15	0.09081	0.26578	0.16994	0.993206
		20	0.04194	0.16028	0.11376	0. 997147
		30	0.02098	0.06760	0.06048	0.999301
		40	0.00788	0.03247	0.02848	0.999789

Table 4.4: Convergence statistics of POD based reconstructions of the computational data for sinusoidal inflow Non-Newtonian flow

Re	St	N	$E_{1\,max}^{N}$	$E_{2\,max}^{N}$	$E_{3\,max}^{N}$	$\sum_{1}^{N}\lambda^{(p)}\big/\sum\lambda$
500	0.024	1	1.03156	1.01530	1.00463	0.962654
		5	0.05259	0.15325	0.07829	0.999162
		6	0.04254	0.08773	0.05813	0.999342
		7	0.02835	0.07138	0.03740	0.999412
		8	0.01224	0.04080	0.02237	0.999440
750	0.024	1	1.01831	1.03532	1.00419	0.926129
		5	0.06106	0.25882	0.11481	0.998626
		6	0.05336	0.15372	0.08344	0.999328
		7	0.04133	0.10479	0.06394	0.999574
		8	0.02244	0.06302	0.04101	0.999688
		9	0.01215	0.04472	0.02792	0.999740
		10	0.01134	0.03267	0.02115	0.999766
500	0.048	1	1.03925	1.02065	1.00694	0.923325
		5	0.04262	0.16447	0.07433	0.998727
		6	0.03418	0.09222	0.05529	0.999118
		7	0.02845	0.05643	0.04708	0.999251
		8	0.01816	0.03794	0.02975	0.999323
750	0.048	1	1.04739	1.03228	1.00990	0.872203
		5	0.06909	0.22528	0.10925	0.996974
		6	0.04902	0.14434	0.07760	0.998264
		7	0.04419	0.11489	0.07411	0.998683
		8	0.03054	0.09702	0.05162	0.999084
		9	0.02622	0.06759	0.04589	0.999230
		10	0.01545	0.04201	0.02951	0.999325

Taking in view this criteria the structure are reconstructed using the POD modes as shown in Figure 4.4 to Figure 4.10 and the number of modes taken together which give more resemblance to the DNS snap is observed. The figures are shown from x=24 to x=34 for clarity. Figure 4.4 shows the flow field reconstructed for the uniform inflow velocity at Re=750 at $\tau = 1.30$. It can be seen that 5 modes taken together capture the flow field efficiently and it resembles the DNS snap. From a qualitative viewpoint, it is shown that the spatial structure of the instantaneous flow field as obtained by DNS calculations can be faithfully captured using a few modes. 8 modes appear to capture the instantaneous flow structure at τ=1.30 very well at Re=500 and St=0.024 as shown in Figure 4.5. But the error norms indicate that a significant amount of deviation ($> 10\%$) in the modal reconstruction is expected over the entire time range of the time interval of the data ensemble. A set of 20 modes bring down the energy level to

nearly 5%. Again a set of 10 modes capture the instantaneous flow structure for Re=750 and St=0.024 in Figure 4.6 .But the error norms are high for 10 modes. 50 modes are required to reduce the error norms below 7%.

(a) DNS snap

(b) 1 mode

(c) 2 modes

(d) 3 modes

(e) 4 modes

(f) 5 modes

Figure 4.4 Comparison of the flow field reconstructed using POD modes for uniform inflow (Newtonian flow) with the numerical simulations at τ=1.30 for Re=750

(a) DNS snap

(b) 1 mode

(c) 2 modes

(d) 3 modes

(e) 4 modes

(f) 5 modes

(g) 8 modes
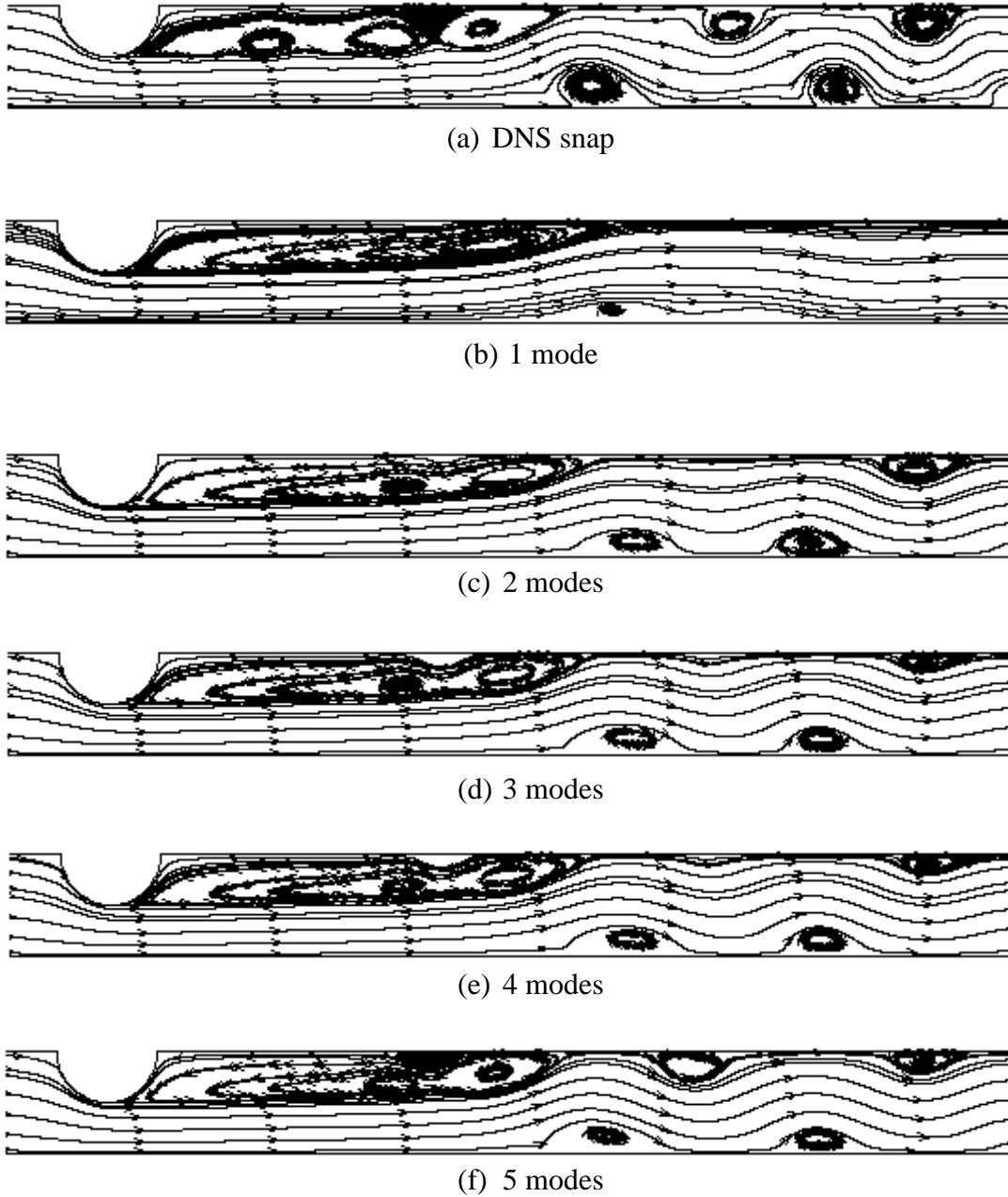
Figure 4.5 Comparison of the flow field reconstructed using POD modes (Newtonian flow) with the numerical simulations at $\tau=1.30$ for Re=500, St=0.024.

(a) DNS snap

(b) 1 mode

(c) 2 modes

(d) 3 modes

(e) 4 modes

(f) 5 modes

(g) 10 modes

Figure 4.6 Comparison of the flow field reconstructed using POD modes (Newtonian flow) with the numerical simulations at $\tau = 1.30$ for Re=750, St=0.024.

(a) DNS snap

(b) 1 mode

(c) 2 modes
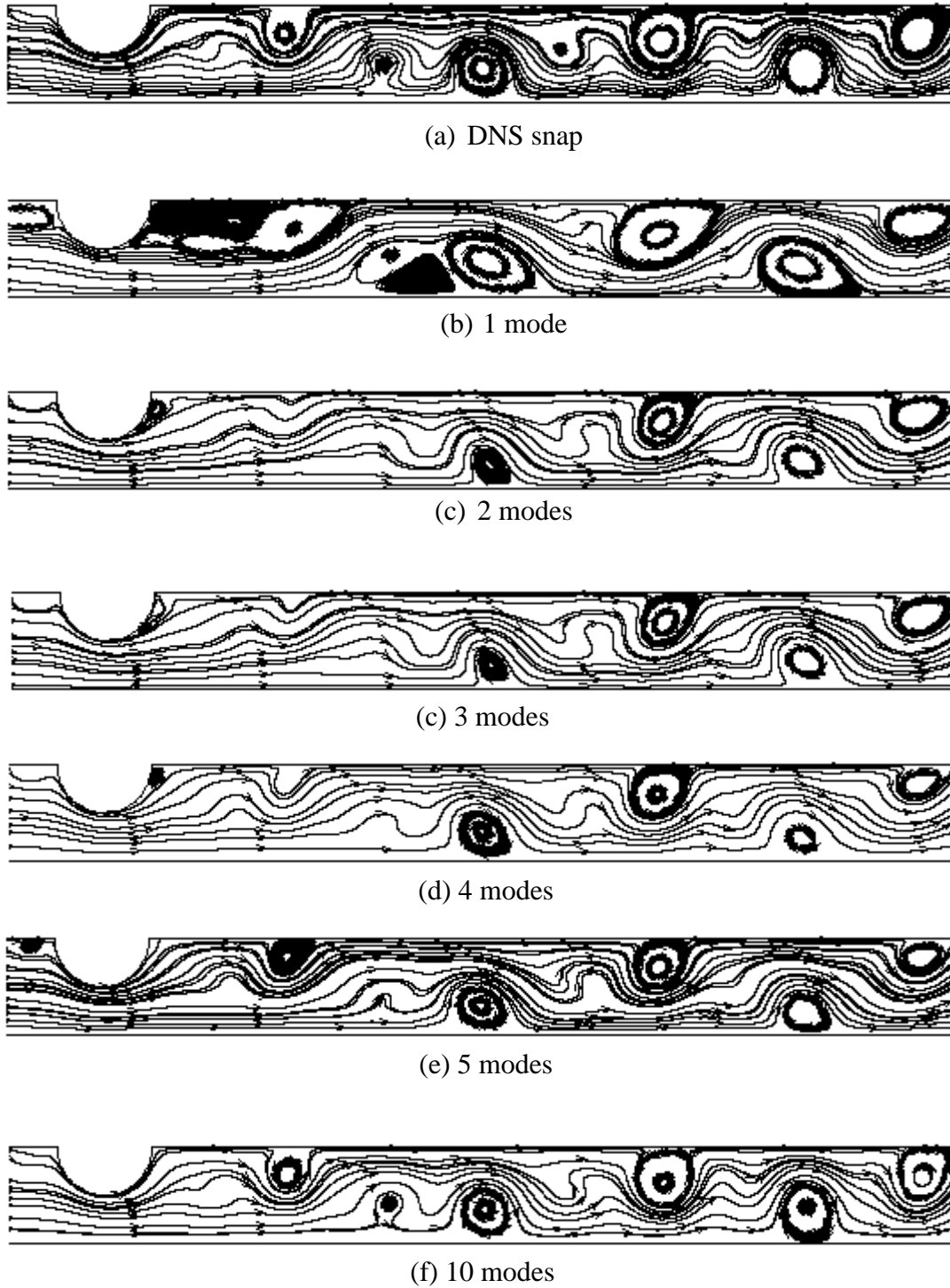

(c) 3 modes

(d) 4 modes

(e) 5 modes

(f) 10 modes

Figure 4.7 Comparison of the flow field reconstructed using POD modes (Newtonian flow) with the numerical simulations at $\tau = 1.30$ for Re=500, St=0.048.

In Figure 4.7, 10 modes are required to capture the DNS snap for Re=500 and St=0.048 whereas 5 modes capture the DNS snap for Re=750 and St=0.048 for in Figure 4.8. The reconstruction of the flow field using POD modes for the non-Newtonian flow at Re=500, St=0.048 is shown

in Figure 4.9. Here only 5 modes are reuired to capture the DNS snap. Again 5 modes are required to capture the DNS snap for Re=750, St=0.048 for non-Newtonian flow as shown in Figure 4.10. In these figures the large-scale structure of the unsteady flow field is captured quite well by a small number of modes. Since large scale structures contain most of the fluctuation energy, it is logical that the first few POD modes capture them quite well.
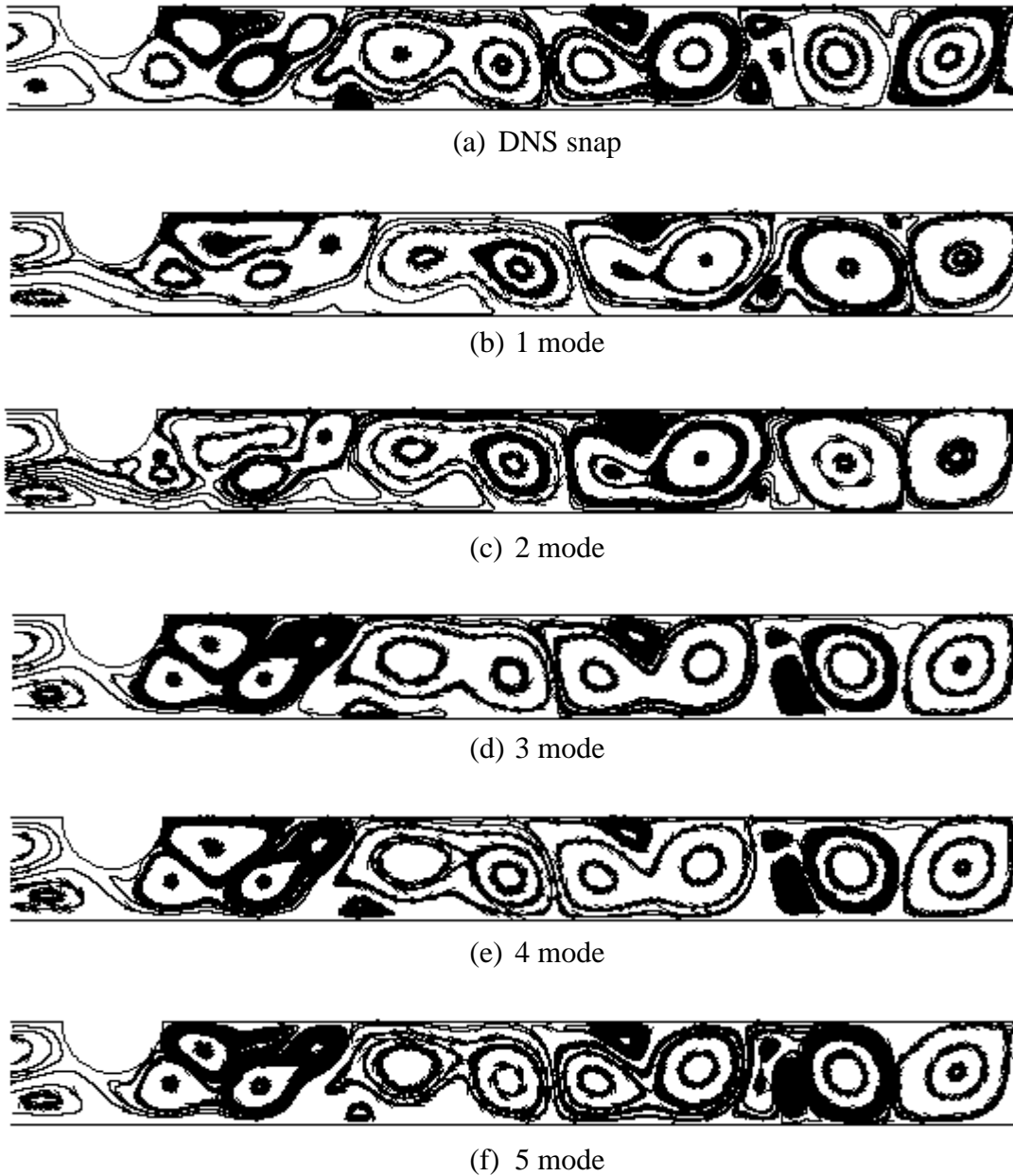

(a) DNS snap

(b) 1 mode

(c) 2 mode

(d) 3 mode

(e) 4 mode

(f) 5 mode

Figure 4.8 Comparison of the flow field reconstructed using POD modes (Newtonian flow) with the numerical simulations at $\tau = 1.30$ for Re=750, St=0.048.

(a) DNS snap

(b) 1 mode

(d) 2 mode

(e) 3 mode

(f) 4 mode

(g) 5 mode

Figure 4.9 Comparison of the flow field reconstructed using POD modes (Non-Newtonian flow) with the numerical simulations at $\tau=1.30$ for Re=500, St=0.048.

(a) DNS snap

(b) 1 mode

(c) 2 mode

(d) 3 mode
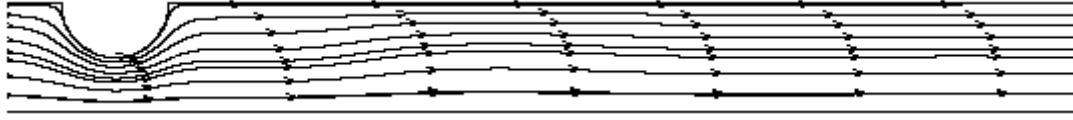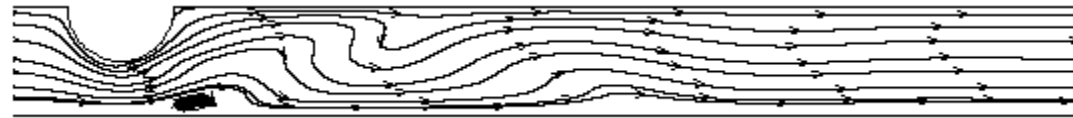

(e) 4 mode

(f) 5 mode
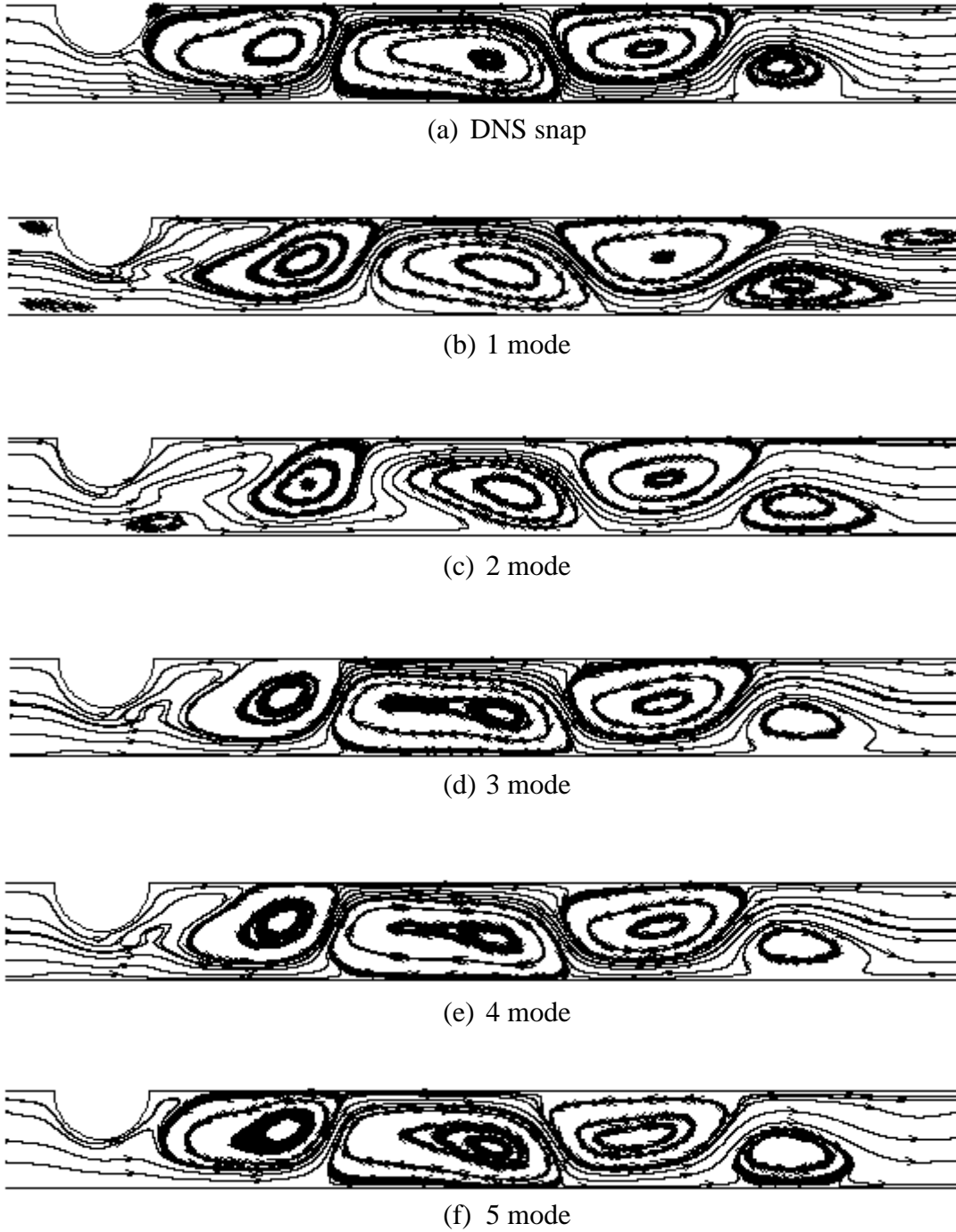
Figure 4.10 Comparison of the flow field reconstructed using POD modes (Non-Newtonian flow) with the numerical simulations at τ=1.30 for Re=750, St=0.048.

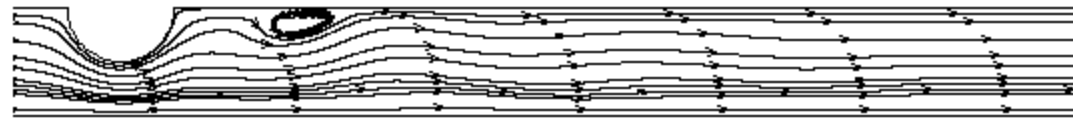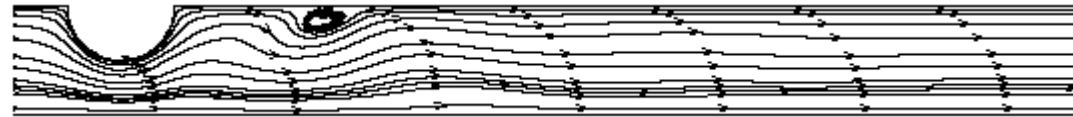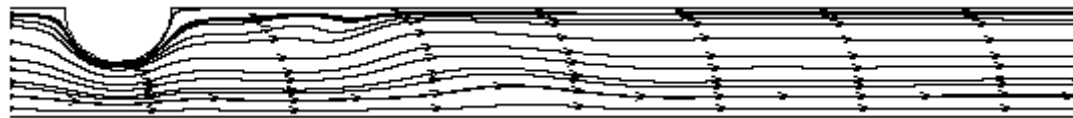Figure 4.11 to Figure 4.17 show the structure of the five eigenfunctions associated with the five largest or leading eigenvalues. Any property of the data ensemble expressed as a linear homogenous form is passed on to the POD modes or the eigenfunctions.

Figure 4.11 The structure of the velocity components of uniform (Newtonian) flow of the first five eigenfunctions at Re=750

Figure 4.11 show the structure of the first five eigenfunctions associated with the five largest or leading eigenvalues for Re=750. It can be seen that the first mode captures the larger vortices while the second mode captures the larger as well smaller vortices.

Figure 4.12 The structure of the velocity components of sinusoidal (Newtonian) flow of the first five eigenfunctions at Re=500, St=0.024

Figure 4.12 to Figure 4.17 show the contribution of individual modes in the reconstruction for sinusoidal flows. The struc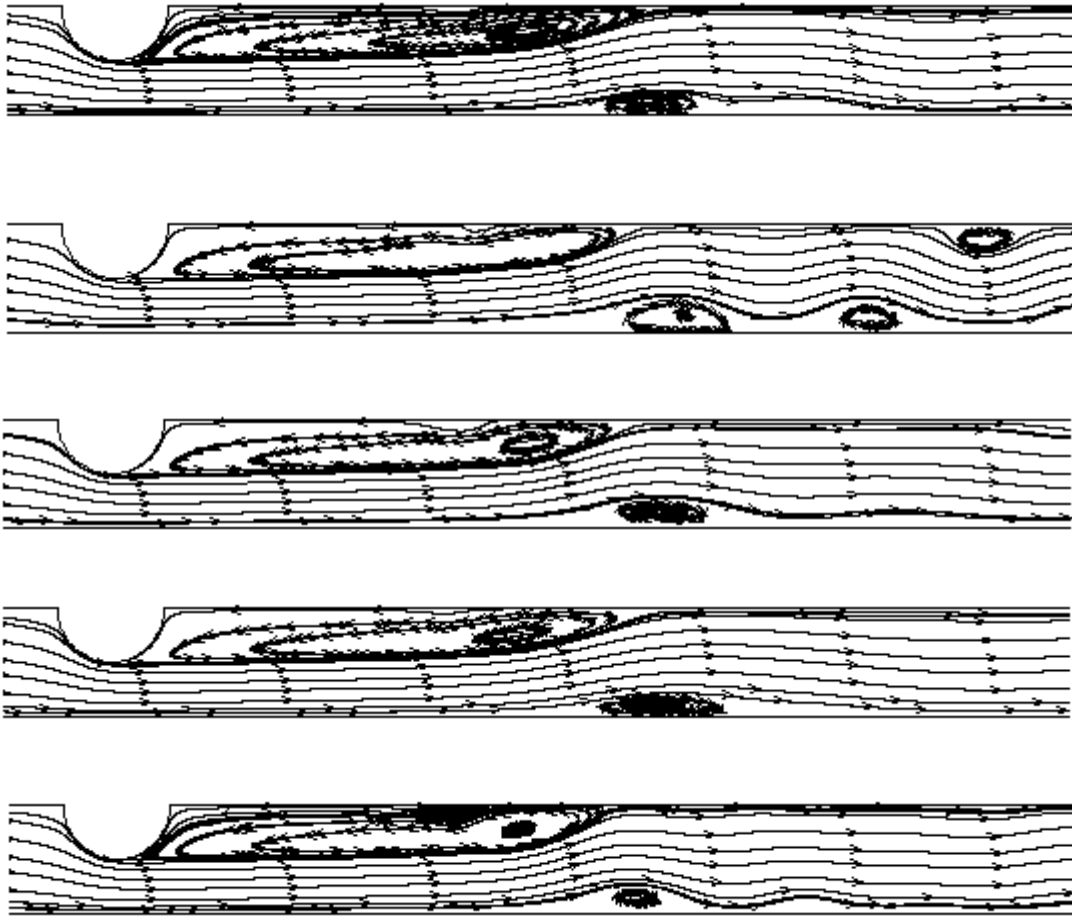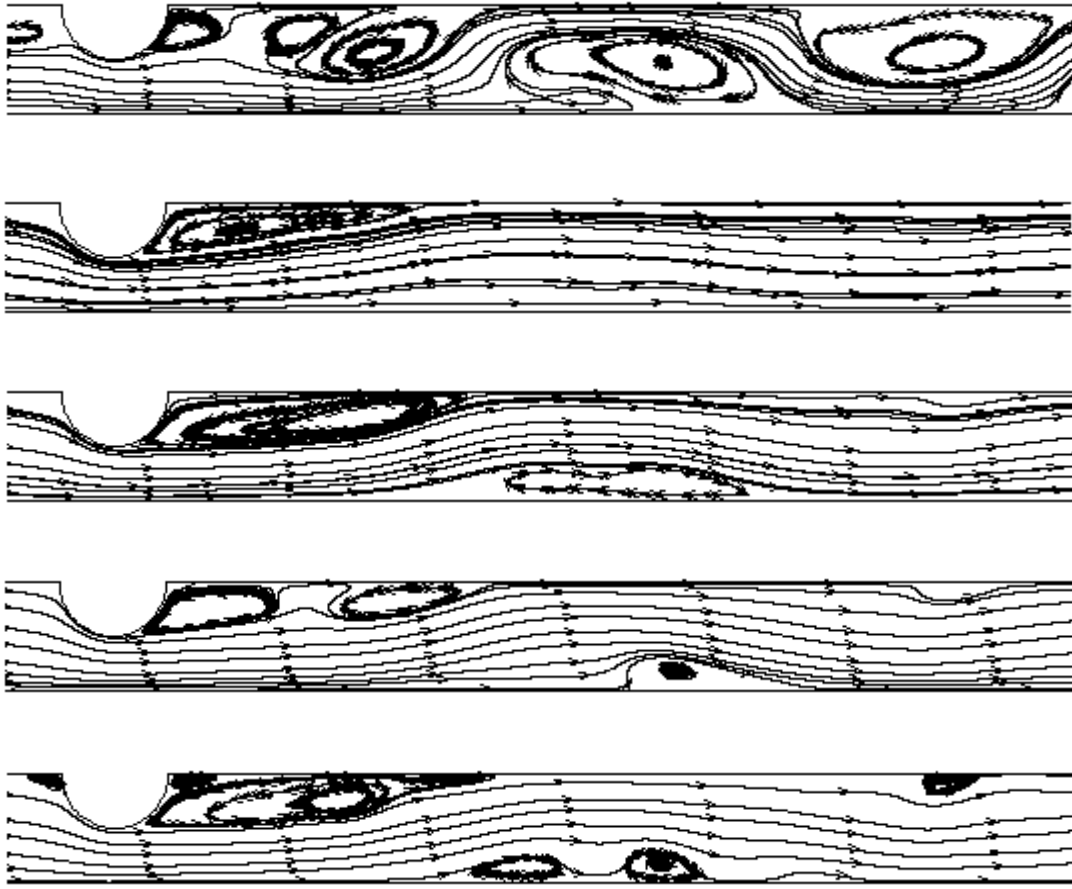ture of the five eigenfunctions associated with the five largest or leading eigenvalues for few cases of Newtonian flows are shown in Figure 4.12 to Figure 4.17. From Figure 4.12 it is seen that the structures comprise of anticlockwise circulation before the stenosis and also a change in the direction of velocity vectors can be seen just before the stenosis for first mode. Also on increasing the Re, keeping St fixed the number of recirculation zone increases for the same mode structure. Here also the first mode captures the most dominant structures. Figure 4.13 shows that most of the structures are captured by the first mode for Re=750, St=0.024. The larger structures are captured by the first mode while the smaller ones are captured by the third mode onwards. The individual contribution of structures for few other cases are shown in Figure 4.14 to Figure 4.17. It could be seen that first mode captures most of the dominant structures. It could be observed that while lesser modes are

required to reconstruct the flow file in non-Newtonian flows, more number of POD modes are required for Newtonian flows.

.

Figure 4.13 The structure of the velocity components of sinusoidal Newtonian flow of the first five eigenfunctions at Re=750, St=0.024

Figure 4.14 The structure of the velocity components of sinusoidal (Newtonian) flow of the
first five eigenfunctions at Re=500, St=0.048

Figure 4.15 The structure of the velocity components of sinusoidal (Newtonian) flow of the first five eigenfunctions at Re=750, St=0.048
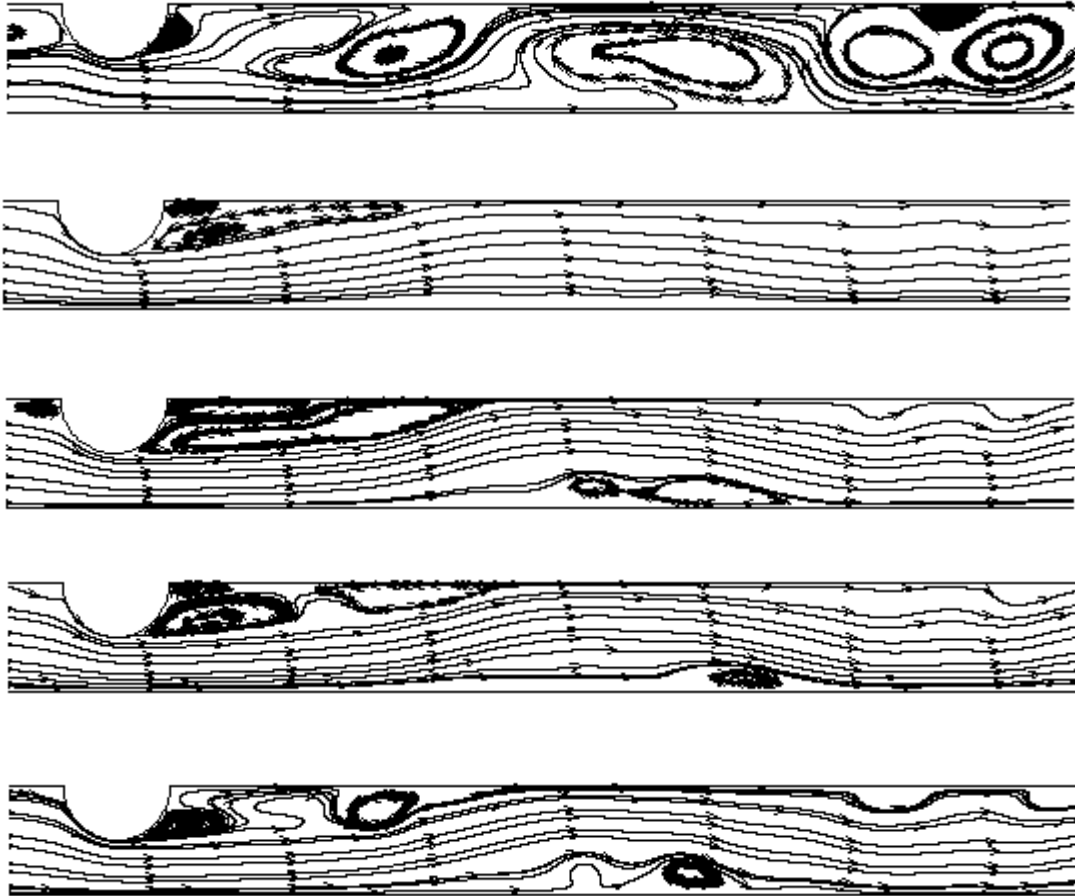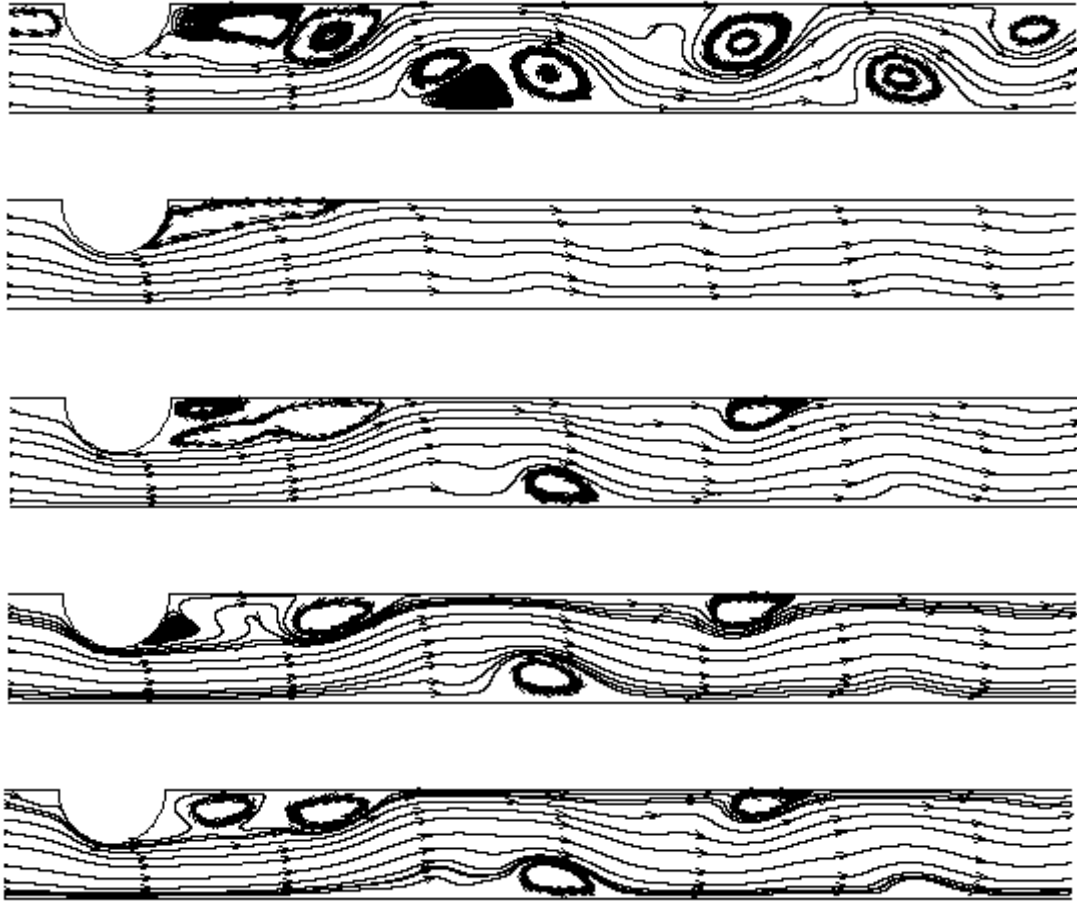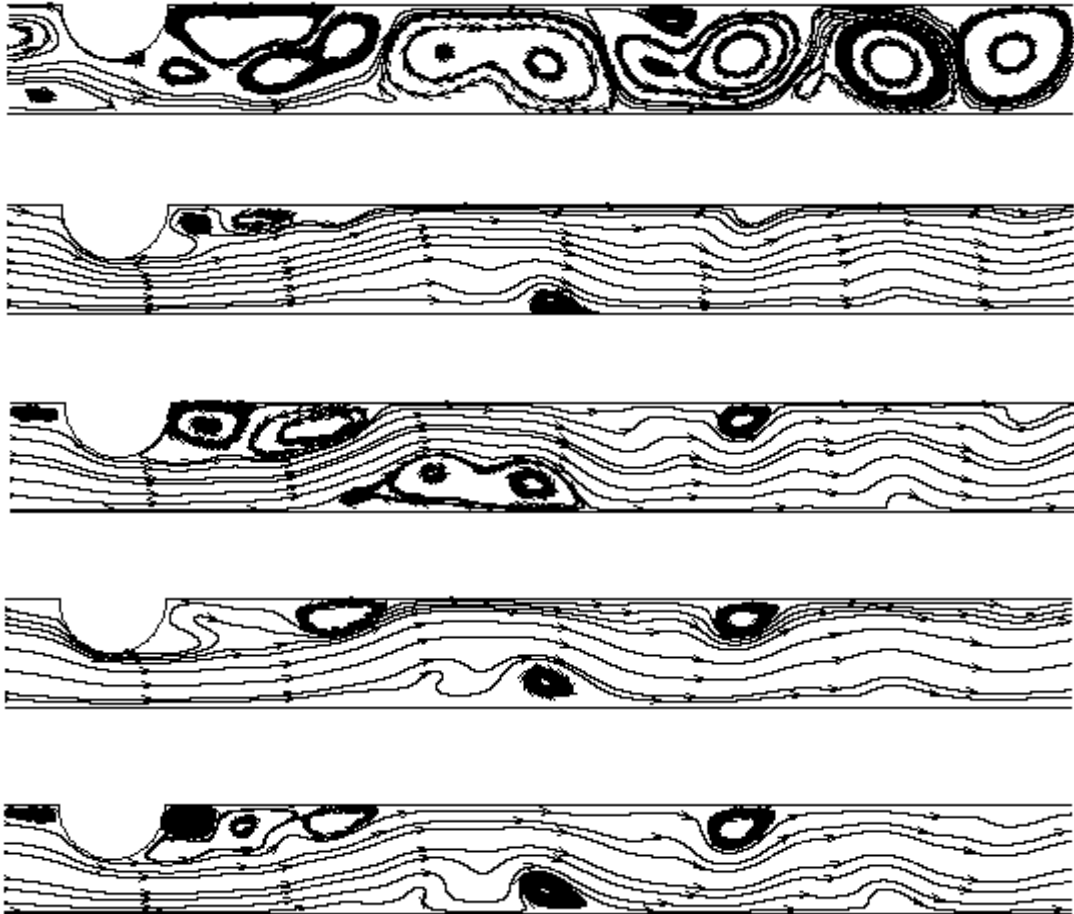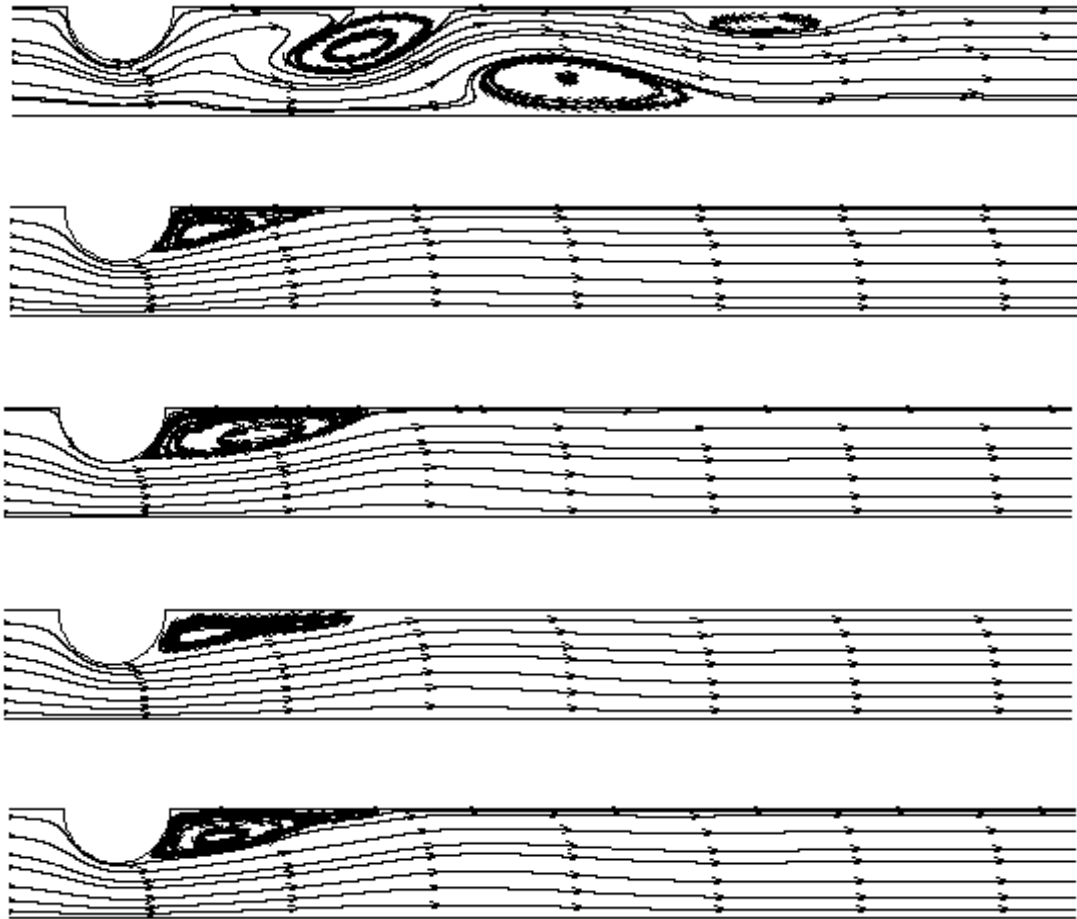
Figure 4.16 The structure of the velocity components of sinusoidal (non-Newtonian) flow of
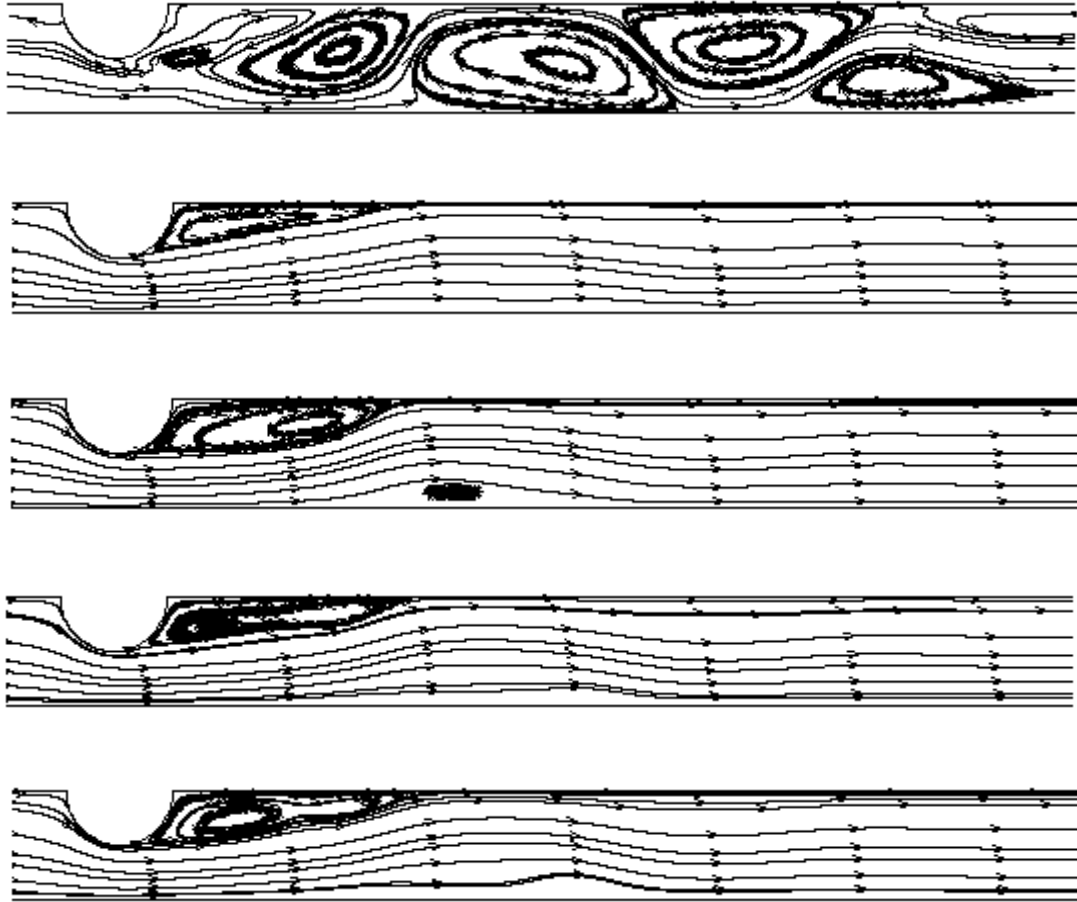the first five eigenfunctions at Re=500, St=0.048

Figure 4.17 The structure of the velocity components of sinusoidal (non-Newtonian) flow of the first five eigenfunctions at Re=750, St=0.048

Chapter 5 Conclusion and Scope for Future Work

The objective of the present study was to do numerical simulation of human arteries which should be efficient and accurate in predicting fluid dynamics generated due to the presence of a stenosis. The study done helps in predicting the changes in various flow properties which occur in stenosed arteries due to different inflow velocity patterns. Also a comparison between assuming blood to be Newtonian and non-Newtonian fluid is studied.

5.1 Conclusion

We have obtained the computational results for uniform and pulsatile flows of Newtonian and shear-thinning fluid modelled using the generalized Newtonian model in a two-dimensional channel. It has been observed that the flow properties are affected by the type of inflow velocity pattern. Some of the key features which could be observed from the simulation results are:

- The simulations reveal the presence of a recirculation zone immediately downstream of the stenosis. The size of the recirculation region increases with increase in Re. Also the pattern of the vortices form depend on the type of flow Newtonian or non-Newtonian. Steady flow condition is attained at lower Reynolds number with the formation of stationary vortex behind the stenosis. On increasing the Re vortex shedding occurs.

- In uniform flow, the shear-thinning fluid predicts higher peak wall shear rate, compared to the Newtonian fluid, though the difference is not much. Also the difference increases slightly on increasing Re.

- For pulsatile flows we have characterized our problem in terms of the basic fluid mechanical parameters, the Reynolds and Strouhal numbers, whereas physiological flows are commonly characterized by the Womersley number. In these flows too, an increase in peak wall shear rate is observed. But the fluctuation in the shear rate are much higher for Newtonian fluids.

- For pulsatile flows anticlockwise vortices are generated behind the stenosis where the flow separation occurs on the upper wall and clockwise stenosis are formed near the lower wall.

- For a non-uniform vessel with nonparallel flow, two flows with the same Womersley number may have very different behavior. For example, in our problem, if we increase the Re and decrease St, Womersley number would not change. However, we would have a longer vortex wave with a larger wavelength and a corresponding change in the wall shear

stress and pressure distributions, although the strength of the wave (in terms of the eddy strength and the magnitude of the peak values of wall shear stress) may not change much as the effect of increasing the Reynolds number would be compensated for by the effect of decreasing the Strouhal number.

- The vortex formed in Newtonian flow is greater than non-Newtonian flow. Since vorticity is high in low viscosity models, it suggest that the viscosity of non-Newtonian model is higher than Newtonian model which goes along with the previous studies that viscosity of blood produced by non-Newtonian models for shear rates (less than $100s^{-1}$) is higher than that of Newtonian models.

- Also since less vortex structures are formed in non-Newtonian model, less POD modes are required to capture the flow field in comparison to Newtonian flow.

5.2 Scope for future Work

The present study is based on the assumption of laminar flow in the human artery at Re = 750 and 500 and St= 0.024 and 0.048. This assumption can be questioned because the flows in stenosed arteries are experimentally noted to be on the edge of turbulence [23]. However we have therefore neglected the onset of turbulence, and assumed laminar flow based on the discussion in [15] which states that conditions like variable viscosity and cell concentration can prevent turbulence from developing. We have assumed smooth channel walls which prevent the onset of turbulence even in the presence of stenosis. A proper method to test this assumption will involve formulating the equations for channel flow in 3D, and solving numerically to see if the solution exhibits turbulence, this is however, beyond the scope of our study. Further, the hemodynamic factors such as wall shear rate for 2D study will be different from those obtained in a more advanced 3D study, but we do not expect the qualitative nature of our conclusions to change even if our study is preliminary compared to a 3D study which also neglects turbulence.

References

1   http://www.who.int/mediacentre/factsheets/fs317/en/

2   Smedby, Ö. (1997). Do plaques grow upstream or downstream? An angiographic study in the femoral artery. Arteriosclerosis, thrombosis, and vascular biology, 17(5), 912-918.

3   Young, D. F. (1979). Fluid mechanics of arterial stenoses. Journal of Biomechanical Engineering, 101(3), 157-175.

4   Womersley, J. R. (1955). Method for the calculation of velocity, rate of flow and viscous drag in arteries when the pressure gradient is known. The Journal of physiology, 127(3), 553.

5   Liepsch, D. (2002). An introduction to biofluid mechanics—basic models and applications. Journal of biomechanics, 35(4), 415-435.

6   Smith, F. T. (1979). The separating flow through a severely constricted symmetric tube. Journal of Fluid Mechanics, 90(04), 725-754.

7   Nandakumar, N., Kirti Chandra Sahu, and M. Anand. "Pulsatile flow of a shear-thinning model for blood through a two-dimensional stenosed channel."*European Journal of Mechanics-B/Fluids* 49 (2015): 29-35.

8   Pontrelli, Giuseppe. "Pulsatile blood flow in a pipe." *Computers & fluids* 27.3 (1998): 367-380.

9   Chakraborty, Debadi, and J. Ravi Prakash. "Viscoelastic fluid flow in a 2D channel bounded above by a deformable finite-thickness elastic wall."*Journal of Non-Newtonian Fluid Mechanics* 218 (2015): 83-98.

10   Mittal, R., S. P. Simmons, and F. Najjar. "Numerical study of pulsatile flow in a constricted channel." *Journal of Fluid Mechanics* 485 (2003): 337-378.

11   Chakraborty, Debadi, et al. "Viscoelastic flow in a two-dimensional collapsible channel." *Journal of Non-Newtonian Fluid Mechanics* 165.19 (2010): 1204-1218.

12   Sochi, Taha. "Non-Newtonian Rheology in Blood Circulation." *arXiv preprint arXiv:1306.2067* (2013).

13   Yeleswarapu, Krishna Kumar. *Evaluation of continuum models for characterizing the constitutive behavior of blood*. 1996.

14   Mann, D. E., & Tarbell, J. M. (1989). Flow of non-Newtonian blood analog fluids in rigid curved and straight artery models. Biorheology, 27(5), 711-733.

15   Nichols, W. W., & O'Rourke, M. F. (1990). McDonald's Blood Flow in Arteries (Edward Arnold, London, UK).

16   Tutty, O. R. (1992). Pulsatile flow in a constricted channel. Journal of biomechanical engineering, 114(1), 50-54.

17   Mandal, P. K. (2005). An unsteady analysis of non-Newtonian blood flow through tapered arteries with a stenosis. International Journal of Non-Linear Mechanics, 40(1), 151-164.

18   Anand, M., & Rajagopal, K. R. (2004). A shear-thinning viscoelastic fluid model for describing the flow of blood. Int. J. Cardiovasc. Med. Sci, 4(2), 59-68.

19   Mustapha, N., Mandal, P. K., Johnston, P. R., & Amin, N. (2010). A numerical simulation of unsteady blood flow through multi-irregular arterial stenoses. Applied Mathematical Modelling, 34(6), 1559-1573.

20   Rabby, M. G., Shupti, S. P., & Molla, M. M. (2014). Pulsatile non-Newtonian laminar blood flows through arterial double stenoses. Journal of Fluids, 2014.

21   Tutty, O. R., & Pedley, T. J. (1993). Oscillatory flow in a stepped channel. Journal of Fluid Mechanics, 247, 179-204.

22   Schlichting, H. (1979). Boundary Layer Theory. McGraw-Hill: New York.

23   Ku, D. N. (1997). Blood flow in arteries. Annual Review of Fluid Mechanics, 29(1), 399-434.

24   Lumley, J. L., & Poje, A. (1997). Low-dimensional models for flows with density fluctuations. Physics of Fluids (1994-present), 9(7), 2023-2031.

25   Sirovich, L. 1987 Turbulence and the dynamics of coherent structures. Part I. Coherent structures. Q. Appl. Maths 45(3), 561–571.

26   Hasan, N. & Sanghi, S. 2004 The dynamics of two-dimensional buoyancy driven convection in a horizontal rotating cylinder. Trans. ASME: J. Heat Transfer 126(6), 963–984

27   Cheng, L., & Armfield, S. (1995). A simplified marker and cell method for unsteady flows on non-staggered grids. International journal for numerical methods in fluids, 21(1), 15-34.

28   Peric, M., & Ferziger, J. H. (1996). Computational methods for fluid dynamics.

29   Rhie, C. M., & Chow, W. L. (1983). Numerical study of the turbulent flow past an airfoil with trailing edge separation. AIAA journal, 21(11), 1525-1532.

30   Hirsch, H. (1990). Numerical computation of internal and external flows. Computational methods for inviscid and viscous flows, 2, 536-556.

31   Amsden, A. A., & Harlow, F. H. (1970). A simplified MAC technique for incompressible fluid flow calculations. Journal of Computational Physics, 6(2), 322-325.

32   Kim, S. W., & Benson, T. J. (1992). Comparison of the SMAC, PISO and iterative time-advancing schemes for unsteady flows. Computers & fluids, 21(3), 435-454.

33   Deane, A. E., & Sirovich, L. (1991). A computational study of Rayleigh–Bénard convection. Part 1. Rayleigh-number scaling. Journal of fluid mechanics, 222, 231-250.

34   Hasan, N., & Sanghi, S. (2007). Proper orthogonal decomposition and low-dimensional modelling of thermally driven two-dimensional flow in a horizontal rotating cylinder. Journal of Fluid Mechanics, 573, 265-295.

35   White, Frank M. *Viscous fluid flow*. Vol. 3. New York: McGraw-Hill, 2006.